ALEX READ

034

COLO-HEP-122

ELEMENTARY PARTICLE PHYSICS

DEPARTMENT OF PHYSICS
UNIVERSITY OF COLORADO BOULDER COLORADO

Measurements of Tau Lepton Production and Decay at $\sqrt{s} = 29$ GeV.

by Alexander Lincoln Read

Measurements of Tau Lepton Production

and Decay at $\sqrt{s} = 29$ GeV.

by

Alexander Lincoln Read

B.S., University of Illinois, 1981

A thesis submitted to the

Faculty of the Graduate School of the

University of Colorado in partial fulfillment

of the requirements for the degree of

Doctor of Philosophy

Department of Physics

1986

Read, Alexander Lincoln (Ph.D., Physics)

Measurements of Tau Lepton Production and Decay at $\sqrt{s} = 29$ GeV.

Thesis directed by Assistant Professor James G. Smith

Properties of the tau lepton were measured in data taken with the MAC detector at the PEP e^+e^- storage ring at the Stanford Linear Accelerator Center. Approximately 27 000 tau-pair events were produced at a center of mass energy of 29 GeV and about half of these were selected from the data in order to study various properties of the tau. Precise measurements of the leptonic branching ratios of the tau yielded $B(\tau \rightarrow \nu_\tau e \bar{\nu}_e) = 0.174 \pm 0.008 \pm 0.005$ and $B(\tau \rightarrow \nu_\tau \mu \bar{\nu}_\mu) = 0.177 \pm 0.008 \pm 0.005$. A precise measurement of the pion branching ratio yielded $B(\tau \rightarrow \nu_\tau \pi) = 0.106 \pm 0.004 \pm 0.008$. A search for tau decays into five charged hadrons was performed and an upper limit on the branching ratio for this decay mode was set at 0.0027 at the 95% confidence level. The Michel parameter was measured with the leptonic energy spectra and was found to be $0.79 \pm 0.11 \pm 0.09$, consistent with the $V - A$ hypothesis for the $\tau\,\nu_\tau - W$ vertex. Measurements of the coupling constants of the tau to the weak neutral current were made by observation of the forward-backward energy asymmetry of the tau decay products and their average energy. These measurements yielded $g_a^e\, g_v^\tau = (0.26 \pm 0.31) \times (1 \pm 0.012)$ and $g_v^e\, g_a^\tau = (-0.05 \pm 0.21 \pm 0.34)$ respectively, consistent with the Glashow-Weinberg-Salam model of electroweak interactions.

"Whenever you get near Longs Peak it turns into an Epic"

Stephen Sessions Talley

ACKNOWLEDGMENTS

I would like to thank the many people who have made the completion of this thesis possible.

I thank my advisor, Jim Smith, for his many contributions to my education as a high energy physicist, the direction he provided in my research, his apparently infinite patience, and the constant encouragement he gave me. He also deserves recognition for developing the tau-pair event selection software which was heavily relied upon in my analysis. I apologize for all the times I complained about how unintelligible I found the code and wish the reader good luck in making any sense of my description of it.

I also thank the many MAC collaborators who were responsible for designing, building, and maintaining our fine detector. The excellent support provided by the online and offline software czars was also appreciated. The many discussions I had with my collaborators were always interesting and often very helpful. I will especially miss the company of the other long term denizens of the "Maze": John Venuti, Manuel Delfino, Glenn Goderre, and Nading Qi. I would also like to thank Takashi Maruyma for his heroic efforts to bring up, maintain, and understand the detector Monte Carlo.

While it is a surprise to some, even graduate students have some sort of a life away from the lab. I thank my parents, Janet and Lincoln, for many years of moral support and the freedom to find my own way. I'm especially grateful for plane fares that allowed me to visit you from time to time and made it possible for Hilde and me to spend so much time together. I also thank my many other friends for their love and encouragement. I especially thank Steve Talley and Mike Ward for their phone calls which always seemed to come just when my spirits were lowest and Bob and Claire Knapp for making me part of their family.

I dedicate this thesis to my best friend and wife, Hilde. I'm sorry it caused us such pain but very thankful that you always told me to keep going and understood that eventually the ordeal would end.

This work was supported in part by the U. S. Department of Energy under contract numbers DE-AC02-81ER40025 (CU), DE-AC03-76SF00515 (SLAC), and DE-AC02-76ER00881 (UW); by the National Science Foundation under grant numbers NSF-PHY82-15133 (UH), NSF-PHY82-15413 and NSF-PHY82-15414 (NU), and NSF-PHY83-08135 (UU); and by the Istituto Nazionale di Fisica Nucleare.

CONTENTS

TABLES

Table

FIGURES

Figure

CHAPTER 1

INTRODUCTION

The heavy lepton tau (τ) was first observed by the SLAC-LBL collaboration in e^+e^- annihilations at the SPEAR storage ring at the Stanford Linear Accelerator Center in 1975.[1] The evidence for the production of tau-pair events was the observation of events containing one electron, one muon, and no other particles. The possibility that the observed events might have been due to a property of charm that wasn't understood was ruled out by the observation of events of this type below the threshold for charm production.[2]

By observation of the total cross section for tau-pair production as a function of center of mass energy near production threshold, the mass of the tau was precisely measured ($m_\tau = 1784 \pm 3$ MeV$/c^2$) and the spin was determined to be 1/2.[3,4] Measurements of the electron energy spectrum were consistent with the hypothesis of a three body decay where two of the particles where neutrinos, one of them the tau neutrino ν_τ.[5] The electron energy spectrum was also consistent with a mass for ν_τ much less than the tau mass. When more data were accumulated it was demonstrated, once again with the electron energy spectrum, that the form of the coupling of $\tau\nu_\tau$ to the weak charged current was consistent with $V - A$ theory.[6] Events containing a muon recoiling against three pions were observed and it was suggested that this was the observation of tau decaying into the A_1 resonance.[7] Later, with more data and experience, measurements of the branching ratios into hadrons were made.[8,9]

The next generation of e^+e^- storage rings, PEP at SLAC and

PETRA at Deutsches Elektronen-Synchrotron (DESY) in Germany, ran at much larger energies and the separation of tau-pair events from other low multiplicity processes was facilitated. Many of the branching ratios have been remeasured with greater precision at PEP and PETRA. The only substaintial change has been a reduction by a factor of two of the branching ratio to three charged hadrons.[3,10] No evidence has been found to indicate that e-μ-τ universality does not hold, i.e., that the only apparent differences between the electron, muon, and tau are that they have different masses, their own separately conserved lepton numbers, and unique associated neutrinos. The first non-zero measurements of the tau lifetime were made at PEP[11] and demonstrated that the strengths of the couplings of $\tau\nu_\tau$ and $\mu\nu_\mu$ to the weak charged current were similar.

The Glashow-Weinberg-Salam (GWS) model of electroweak interactions[12] has been spectacularly successful in describing all electro-weak interactions. One more test of this model is to verify that the interaction of the weak neutral current with the tau is correctly described. Lepton universality can be tested by comparing this reaction with the interactions of electrons and muons with the weak neutral current. The center of mass energies at the PEP and PETRA rings were large enough to look for the effects of the weak neutral boson Z^0 on the cross section for producing tau-pair events.

This thesis describes three sets of experiments which measured various properties of the tau. The first consists of precise measurements of the tau leptonic branching ratios and the branching ratio $B(\tau \to \nu_\tau \pi)$. The second experiment is an attempt to measure the branching ratio for tau decay to five charged hadrons. The third experiment is a comparison of measurements of the process $e^+e^- \to \tau^+\tau^-$ with the GWS model of electroweak interactions.

1.1 Electroweak Interactions

The Glashow-Weinberg-Salam model of electroweak interactions is the simplest model which (1) reproduces all that is known about low energy weak charged interactions and electromagnetic interactions (2) is renormalizible (does not violate probability conservation due to divergences in the energy dependence of a cross section) and (3) is gauge invariant. The Lagrangian of the GWS model (known as the standard model) incorporates two sets of interactions: (1) an isospin triplet of weak currents which couple to three vector bosons $\vec{W}^{\mu}$ with strength g and (2) a weak hypercharge current which couples to a vector boson B^{μ} with strength $g'/2$. Requiring the electromagnetic interaction to appear in the model forces a relation between the coupling constants e, g, and g' and the mixing angle that determines what mixture of gauge fields B^{μ} and W_3^{μ} appear in the physical photon and massive neutral boson: $e = g\sin\theta_W = g'\cos\theta_W$. The mixing angle θ_W is known as the Weinberg angle. In order to give masses to the charged vector bosons, denoted by $W^{\pm} = \frac{1}{\sqrt{2}}(W_1 \pm iW_2)$, while leaving the photon massless and preserving the gauge invariance of the Lagrangian, a spontaneous symmetry breaking isospin doublet containing four scalar fields (Higgs bosons) was introduced into the electroweak Lagrangian. For the particular choice of Higgs field which was made the relative strength of the weak neutral and charged current interactions is given by

$$\rho = \frac{M_W^2}{M_Z^2\cos^2\theta_W} = 1. \tag{1.1}$$

The above results can be used to derive the vertex factor for the coupling of the weak neutral current to a fermion line in the standard model:

$$\frac{-ig}{\cos\theta_W}\gamma^{\mu}[\frac{1}{2}(1-\gamma^5)T_f^3 - \sin^2\theta_W Q_f], \tag{1.2}$$

where T_f^3 and Q_f are the third component of weak isospin and charge for fermion f. This vertex factor is commonly written in terms of the axial vector and vector coupling constants:

$$\frac{-ig}{\cos\theta_W}\gamma^\mu\frac{1}{2}(g_v^f - g_a^f\gamma^5). \tag{1.3}$$

If τ^- and ν_τ are members of a weak isospin doublet then $Q_\tau = -1$ and $T_\tau^3 = -\frac{1}{2}$ which leads to the standard model predictions of the coupling constants of the tau to the axial vector and vector components of the weak neutral current:

$$g_a^f = T_f^3 = -\frac{1}{2} \tag{1.4}$$

$$g_v^f = T_f^3 - 2\sin^2\theta_W Q_f = -\frac{1}{2} + 2\sin^2\theta_W. \tag{1.5}$$

A comparison of the results of calculations of the muon lifetime in the Standard Model with the $V - A$ point interaction model produces a relationship between the Fermi coupling constant G_F and the weak isospin coupling constant g:

$$\frac{G_F}{\sqrt{2}} = \frac{g^2}{8M_W^2}. \tag{1.6}$$

The measured muon lifetime implies $G_F = (1.16634 \pm 0.00002) \times 10^{-5}\,\mathrm{GeV}^{-2}$. The more familiar G_F will be used in place of g throughout the rest of this discussion.

1.2 Cross Section

The spin dependent cross section for the process $e^+e^- \to \tau^+\tau^-$ with unpolarized beams, calculated from the Feynman diagrams in Figure 1 and including only terms of order G_F or lower, is[13]

$$\frac{d\sigma(\vec{s}_-, \vec{s}_+)}{d\Omega} = \frac{\alpha^2\beta}{4s}[(1 - rg_v^e g_v^\tau)t_1 + rg_a^e g_a^\tau t_2 + rg_a^e g_v^\tau t_3 - rg_v^e g_a^\tau t_4] \tag{1.7}$$

where

$$
\begin{aligned}
r &= \frac{G_F}{\pi\sqrt{2}\alpha}\frac{sM_z^2}{M_z^2 - s}, \\
t_1 &= 1 + \cos^2\theta + \frac{1}{\gamma^2}\sin^2\theta + s_z^+ s_z^- (1 + \cos^2\theta - \frac{1}{\gamma^2}\sin^2\theta) \\
&\quad + s_x^- s_x^+ \frac{1}{\gamma^2}\sin^2\theta - s_y^- s_y^+ \beta^2 \sin^2\theta - (s_x^- s_z^+ + s_z^- s_x^+)\frac{1}{\gamma}\sin 2\theta, \\
t_2 &= -2\beta\cos\theta(1 + s_z^- s_z^+) + (s_x^- s_z^+ + s_z^- s_x^+)\frac{\beta}{\gamma}\sin\theta, \\
t_3 &= 2(s_z^- + s_z^+)\cos\theta - 2(s_x^- + s_x^+)\frac{1}{\gamma}\sin\theta, \text{ and} \\
t_4 &= -(s_z^- + s_z^+)\beta(1 + \cos^2\theta) + (s_x^- + s_x^+)\frac{\beta}{2\gamma}\sin 2\theta.
\end{aligned}
\tag{1.8}
$$

The polar angle between the outgoing τ^- and the incoming e^- is θ, s is the center of mass energy squared, M_Z is the mass of the weak neutral boson, β is the velocity of the taus in the laboratory in units of the velocity of light, γ is $1/\sqrt{1-\beta^2}$, and α is the electromagnetic coupling constant, $e^2/4\,\pi$. The tau spins $\vec{s}_\pm$ are calculated in their respective centers of mass using a coordinate system for which the z-axis points along the direction of flight of the τ^-, the x-axis is formed from the cross product of the e^- direction with the z-axis, and the y-axis completes a right handed coordinate system. The constant r is an approximation made under the assumption that the center of mass energy is many times the width of the Z^0 lower than M_Z.

1.3 Production Angular Distribution

Observation of the tau-pair angular distribution with respect to the beam axis implies a summation over spins in equation (1.7) which in practice means that spin-dependent terms are eliminated. The resultant differential cross section assumes the form

$$
\frac{d\sigma}{d\cos\theta} = \frac{\pi\alpha^2\beta}{2s}[(1 - rg_v^e g_v^\tau)(1 + \cos^2\theta + \frac{1}{\gamma^2}\sin^2\theta) - 2\beta r g_a^e g_a^\tau \cos\theta]. \tag{1.9}
$$

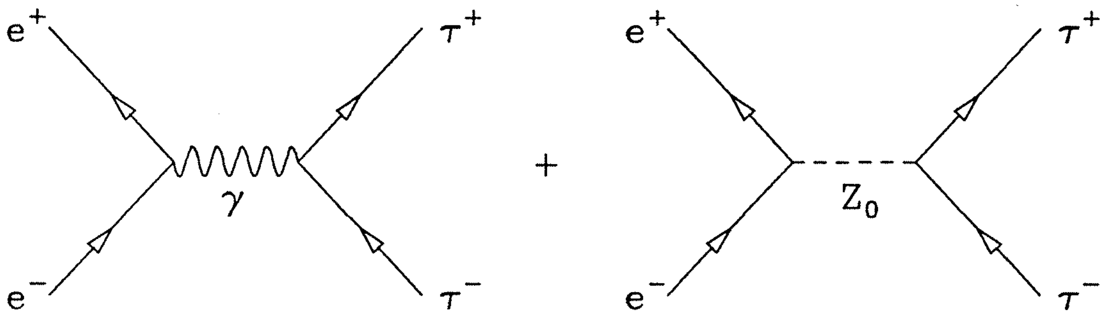

FIGURE 1. Feynman diagrams for lowest order cross section for the process $e^+e^- \rightarrow \tau^+\tau^-$.

The term proportional to $\cos\theta$ produces a forward-backward asymmetry in the angular distribution and a measurement of this asymmetry is sensitive to the coupling constant product $g_a^e g_a^\tau$. The asymmetry is defined by

$$A_{\tau\tau} = \frac{\sigma(\cos\theta > 0) - \sigma(\cos\theta < 0)}{\sigma(\cos\theta > 0) + \sigma(\cos\theta < 0)} \tag{1.10}$$

and after performing the integrations is found to be

$$A_{\tau\tau} = -\frac{3}{4}\beta r g_a^e g_a^\tau. \tag{1.11}$$

The world average value of the Weinberg angle ($\sin^2\theta_W = 0.22$[14]) and the world average value of the mass of the weak neutral boson ($M_Z = 93$ GeV/c^2[15]) yield $r = 0.3370$. The value of the asymmetry expected from the standard model, at a center of mass energy of 29 GeV, is therefore -6.3%. The ratio of the total cross section for this process to the total cross section due to the electromagnetic interaction only is

$$R_{\tau\tau} = 1 - r g_v^e g_v^\tau. \tag{1.12}$$

A measurement of $R_{\tau\tau}$ is therefore sensitive to $g_v^e g_v^\tau$. The expected value of $1 - R_{\tau\tau}$ is 0.5×10^{-3}. Table 1 summarizes the measurements of $A_{\tau\tau}$ and $R_{\tau\tau}$. There is good agreement with the standard model.

TABLE 1. Measurements of $R_{\tau\tau}$, the ratio of the total cross section for $e^+e^- \to \tau^+\tau^-$ to the predicted QED total cross section and $A_{\tau\tau}/A_{\tau\tau}(Pred.)$, the ratio of the measured charge asymmetry to that predicted by the Standard Model. The statistical and systematic errors for each experiment have been added in quadrature for the calculation of the average.

Experiment	$R_{\tau\tau}$	$A_{\tau\tau}/A_{\tau\tau}(Pred.)$
MAC[16]	$0.98 \pm 0.01 \pm 0.034$	$0.97 \pm 0.21 \pm 0.09$
Mark II[17]	$0.996 \pm 0.016 \pm 0.028$	0.74 ± 0.35
JADE[18]	$0.963 \pm 0.017 \pm 0.035$	$0.73 \pm 0.21 \pm 0.09$
HRS[19]	$1.10 \pm 0.03 \pm 0.04$	$1.03 \pm 0.39 \pm 0.08$
PLUTO[20]	$0.89 \pm 0.05 \pm 0.08$	$0.62 \pm 0.72 \pm 0.26$
TASSO[21]	$1.03 \pm 0.05^{+0.06}_{-0.11}$	$0.53 \pm 0.58 \pm 0.14$
Average	0.992 ± 0.018	0.83 ± 0.13

1.4 Tau Polarization

The longitudinal polarization of the τ^- is defined by

$$P_\tau = \frac{d\sigma(s_z^- = +1) - d\sigma(s_z^- = -1)}{d\sigma(s_z^- = +1) + d\sigma(s_z^- = -1)} \tag{1.13}$$

and can be calculated from equation (1.7):

$$P_\tau = r \frac{g_v^e\, g_a^\tau\, \beta(1+\cos^2\theta) + g_a^e\, g_v^\tau\, 2\,\cos\theta}{(1+\cos^2\theta + \frac{1}{\gamma^2}\sin^2\theta)(1 - r g_v^e g_v^\tau) - r g_a^e g_a^\tau 2\beta\cos\theta}. \tag{1.14}$$

The polarization of the τ^- is identical to that of the τ^+ and depends on the center of mass energy, polar angle and the two products of coupling constants $g_a^e g_v^\tau$ and $g_v^e g_a^\tau$. At $\sqrt{s} = 29$ GeV r and g_v are expected to be sufficiently small that P_τ can be approximated by

$$P_\tau = r(g_v^e\, g_a^\tau + \frac{2\cos\theta}{1+\cos^2\theta} g_a^e\, g_v^\tau). \tag{1.15}$$

Evidently a measurement of the polarization averaged over solid angle is sensitive only to $g_v^e g_a^\tau$ whereas a measurement of the polarization asymmetry, defined by

$$A_P = \frac{1}{2}(P_F - P_B), \tag{1.16}$$

where P_F and P_B are the average polarizations for $\cos\theta > 0$ and $\cos\theta < 0$ respectively, is sensitive only to $g_a^e\, g_v^\tau$. It is straightforward to show that

$$\langle P \rangle = r\, g_v^e\, g_a^\tau, \text{ and} \tag{1.17}$$

$$A_P = r\, g_a^e\, g_v^\tau \frac{3\,x^2}{3\,x + x^3}, \tag{1.18}$$

where x is the maximum allowable $|\cos\theta|$ of tau-pairs in an analysis sample. The average polarization, at $\sqrt{s} = 29$ GeV, is expected to be 1.01% and the polarization asymmetry to be 0.76% (0.72%) for full acceptance (for $|\cos\theta| < 0.9$).

The polarization can be measured by observation of the angular distribution of decay products with respect to the polarization axis. Fortunately the tau lifetime is short enough that decays are contained inside typical colliding beam detectors (for a beam energy of 14.5 GeV the average tau decay length is 680 microns) and thus it is possible to observe the tau decay products.† Due to the $V - A$ nature of charged weak interactions (the neutrino helicity is -1), parity is maximally violated and the decay angular distribution is antisymmetric. This means, for example, that in the decay $\tau^- \to \nu_\tau \pi^-$ the neutrino direction is not allowed to lie along the τ^- spin axis in order to conserve angular momentum. When tau decays are Lorentz boosted into the laboratory frame an angular distribution in the center of mass is transformed into a momentum and angle distribution. Since it is impossible to reconstruct the original tau direction in leptonic decays and experimentally difficult for semi-leptonic decays, it is practical simply to observe the energy spectrum.

1.5 Tau Decays

The following section lists the various expected tau decay modes and results of calculations of differential and total decay rates in the standard model where τ and ν_τ couple with a $V - A$ interaction of strength G_F to the weak charged current. The results come from Tsai[23] and Gilman and Rhie.[24] Unknown couplings of the decay products to the weak charged current were extracted from experiment or reasonable theoretical hypotheses whenever possible. The calculations were done in the tau center of mass and expressed in terms of p and E, the momentum and energy of the charged tau decay product, θ, the angle between the charged decay product and the polarization axis, and P, the degree of polarization. The expressions for τ^+ decay can be related to τ^- decay via CP conservation by simply changing

† There was a proposal in the 1974 PEP Summer Study to measure the polarization of muons in the reaction $e^+e^- \to \mu^+\mu^-$ by stopping the muons with a 10 000 ton uranium ball and measuring the decays $\mu \to \nu_\mu e \bar{\nu}_e$ with a 3600 ton aluminium polarimeter.[22]

the signs of the angular dependent terms in the differential decay rates. The tau neutrino was assumed to be massless.

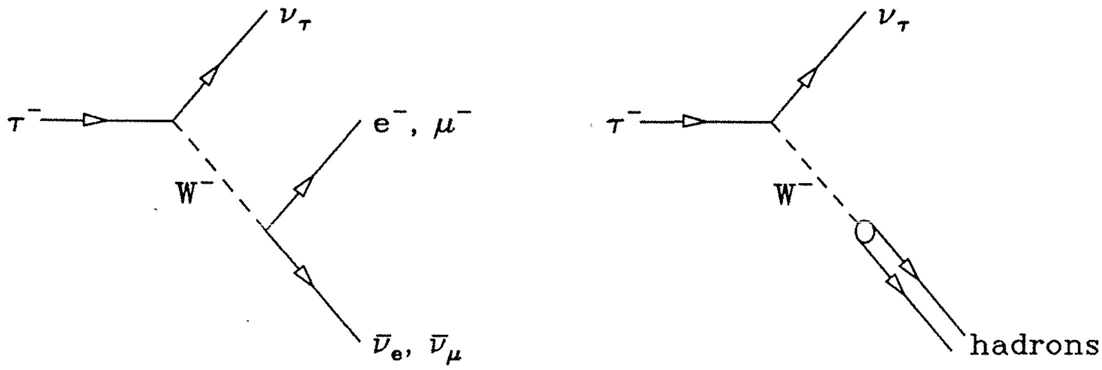

FIGURE 2. Feynman diagrams for leptonic and semi-leptonic tau decays.

1.5.1 $\tau^- \rightarrow \nu_\tau e^- \bar{\nu}_e$

This decay can be calculated directly from the leptonic Feynman diagram in Figure 2. The resultant differential decay rate, neglecting the mass of the electron, is

$$\frac{d^2\Gamma_e}{dp\,d\cos\theta} = \frac{G_F^2 m_\tau^5}{192\pi^3}\frac{8}{m_\tau^4}p^2[3m_\tau - 4p - P\cos\theta(4p - m_\tau)]. \tag{1.19}$$

The total decay rate can be found by integrating over momentum and $\cos\theta$:

$$\Gamma_e = \frac{G_F^2 m_\tau^5}{192\pi^3}. \tag{1.20}$$

It is straightforward to show that the tau lifetime is

$$\tau_\tau = \frac{B(\tau \rightarrow \nu_\tau e \bar{\nu}_e)}{\Gamma_e}. \tag{1.21}$$

1.5.2 $\tau^- \rightarrow \nu_\tau \mu^- \bar{\nu}_\mu$

The calculation of this decay rate is similar to the previous one but the mass of the muon m_μ is no longer negligible compared with the mass of the tau. The result is

$$\begin{aligned}\frac{d^2\Gamma_\mu}{dp\,d\cos\theta} =& \frac{G_F^2 m_\tau^5}{192\pi^3}\frac{8}{m_\tau^4}p^2[3m_\tau - 4E - 2\frac{m_\mu^2}{E} + 3\frac{m_\mu^2}{m_\tau} \\ &- P\cos\theta\frac{p}{E}(4E - m_\tau - 3\frac{m_\mu^2}{m_\tau})]\end{aligned} \quad . \tag{1.22}$$

Defining $y = (m_\mu/m_\tau)^2$ the total decay rate is

$$\Gamma_\mu = \Gamma_e \cdot (1 - 8y + 8y^3 - y^4 - 12y^2 \ln y) = 0.973 \cdot \Gamma_e.$$

1.5.3 $\tau \rightarrow \nu_\tau \pi^-$

This decay is simply related to the decay $\pi \rightarrow \mu\bar{\nu}_\mu$ and the coupling constant at the $W\,\pi$ vertex, $f_\pi \cos\theta_c$, (θ_c is the Cabibbo angle) has been precisely measured in pion decay experiments. The differential decay rate is

$$\frac{d\Gamma_\pi}{d\cos\theta} = \frac{G_F^2\, f_\pi^2 \cos^2\theta_c}{32\,\pi} m_\tau^3\,(1 - \frac{m_\pi^2}{m_\tau^2})^2\,(1 + P\cos\theta) \tag{1.23}$$

and the total decay rate relative to the electronic decay rate is

$$\Gamma_\pi/\Gamma_e = 0.607. \tag{1.24}$$

1.5.4 $\tau \rightarrow \nu_\tau K^-$

This Cabibbo suppressed decay is very similar to $\tau \rightarrow \nu_\tau \pi$ and the coupling constant at the $W\,K$ vertex, $f_K \sin\theta_c$, has been precisely measured elsewhere. The differential decay rate is

$$\frac{d\Gamma_K}{d\cos\theta} = \frac{G_F^2\, f_K^2 \sin^2\theta_c}{32\,\pi} m_\tau^3 \,(1 - \frac{m_K^2}{m_\tau^2})^2\,(1 + P\cos\theta) \tag{1.25}$$

and the total decay rate relative to the electronic decay rate is

$$\Gamma_K/\Gamma_e = 0.0395. \tag{1.26}$$

1.5.5 $\tau^- \rightarrow \nu_\tau \rho^-$

This resonance decay is expected to dominate the $\pi\pi$ decays of the tau. The total decay rate can be calculated from the measured $e^+e^- \rightarrow \pi^+\pi^-$ cross section by invoking the conserved-vector-current hypothesis (CVC) which relates the strength of $W - \rho$ coupling to that of $\gamma - \rho$ coupling. The total decay rate obtained in this manner is

$$\Gamma_\rho = 1.23 \cdot \Gamma_e. \tag{1.27}$$

The differential decay rate is

$$\begin{aligned} \frac{d^2\Gamma_\rho}{dm\, d\cos\theta} = & \frac{G_F^2\, f_\rho^2 \cos^2\theta_c\, m_\tau^3}{32\,\pi^2 \quad\; m}(1-y)^2(1+2\,y) \\ & \times \left(1 + P\,\cos\theta\,\frac{1-2\,y}{1+2\,y}\right) \times |A_{BW}|^2 \end{aligned}, \tag{1.28}$$

where $y = m^2/m_\tau^2$ and $|A_{BW}|^2$ is the relativistic Breit-Wigner amplitude squared:

$$|A_{BW}|^2 = \frac{m_\rho\,\Gamma(q)}{m_\rho^2\,\Gamma^2(q) + (m_\rho^2 - m^2)^2}, \tag{1.29}$$

and where $\Gamma(q)$ is the decay rate of the rho which depends on the pion momentum in the rho center of mass (q) and is of the form $\Gamma(q) = \Gamma_0 \times (q/q_0)^3$.

Apart from the large width of the rho, the reason that the differential decay rate here is more complicated than those for decays to pseudoscalar hadrons is that the ρ is a vector particle. The strength with which the W couples to the various helicity states of a vector particle depends on the vector's mass. That one of the three helicity states is forbidden by angular momentum conservation introduces an additional complication.

1.5.6 $\tau^- \rightarrow \nu_\tau(5, 6\pi)^-$

$e^+e^- \rightarrow (6\pi)$ data are sparse but if a reasonable upper limit is taken for this cross section and CVC is invoked a limit on the (6π) decay rate can be set:

$$\Gamma_{6\pi} \leq 0.024 \cdot \Gamma_e. \tag{1.30}$$

The (5π) decay couples only to the axial-vector current and there is no independent experimental determination of the strength of this coupling. There is one estimate of the branching ratio $B(\tau \rightarrow \nu_\tau(5\pi)) = 1\%$ based on the partially conserved axial-vector current hypothesis but it is plagued with theoretical uncertainties.

For the purpose of calculating the angular dependent differential decay rate it was assumed that both of these decays occur through a spin 1 intermediate state so that equation (1.28) cold be used with $m^2_{(5\pi,6\pi)} = m^2_\rho$. This is not an important point since these decays are rare. The Breit-Wigner factor in (1.28) was replaced by a continuum mass distribution with $m > 1100$ MeV/c^2.

1.5.7 Other Tau Decays

The differential decay rates for the following decay modes can be obtained by substituting the appropriate mass for m_ρ, decay rate for $\Gamma(q)$, and form factor for $f_\rho^2 \cos^2\theta_C$ in equation (1.28):

$$\begin{aligned}
\tau^- &\rightarrow \nu_\tau K^\star \\
\tau^- &\rightarrow \nu_\tau A_1^- \\
\tau^- &\rightarrow \nu_\tau (Q_1, Q_2)^- \\
\tau^- &\rightarrow \nu_\tau \rho'^- .
\end{aligned}$$

The total decay rates for two of these decay modes have been estimated:

$$\begin{aligned}
\Gamma_{K^\star} &= 0.064 \cdot \Gamma_e \\
\Gamma_{\rho'} &= 0.55 \cdot \Gamma_e .
\end{aligned} \tag{1.31}$$

The first result above comes directly from Gilman and Rhie.[24] The second result was calculated from $\Gamma_{4\pi} = 0.330\Gamma_e$[24] and the measured branching ratio $B(\rho' \rightarrow 4\pi) = 0.60 \pm 0.07$.[14] This calculation is valid since the ρ' dominates the e^+e^- data used to calculate $\Gamma_{4\pi}/\Gamma_e$ and is expected to dominate the decay $\tau \rightarrow 4\pi$.

1.6 Summary of Measured Tau Properties

1.6.1 Branching Ratios to Inclusive Charge Multiplicity States

Several measurements of exclusive tau branching ratios reported here require knowledge of the inclusive branching ratios to one, three, and five charged particles. The results of the six experiments which have made significant contributions to the measurement of B_3, the branching ratio to three charged particles, are listed in Table 2. By convention, charged pions

TABLE 2. Measurements of B_3, the inclusive branching ratio of tau to three charged particles. The statistical and systematic errors of each experiment have been added in quadrature for the calculation of the average.

Experiment	$B_3(\%)$
HRS[25]	$13.0 \pm 0.2 \pm 0.3$
MAC[26]	$13.3 \pm 0.3 \pm 0.6$
JADE[18]	$13.6 \pm 0.5 \pm 0.8$
DELCO[10]	$12.1 \pm 0.5 \pm 1.2$
TPC[28]	$14.8 \pm 0.9 \pm 1.5$
TASSO[21]	$15.3 \pm 1.1^{+1.3}_{-1.6}$
Average	13.2 ± 0.3

from K^0_S decays are counted as charged particles while e^+e^- pairs from photon conversions and Dalitz decays of π^0's are not.

It has been known for some time that the 5-prong branching ratio is small. The earliest measurements by Brandelik *et al.*,[29] $B_5 < 0.06$ (95% confidence level), and Behrend *et al.*,[30] $B_5 = 0.010 \pm 0.004$, established that the 5-prong branching ratio was smaller than B_3. Subsequent measurements, including a preliminary version of the analysis presented here, showed that B_5 was less than 1% (see Table 3). After these upper limits had been published two experiments observed an unambiguous signal of about a dozen 5-prong tau decays (see Table 3). The average of their measurements is $B_5 = 0.0014 \pm 0.0004$, where the statistical and systematic errors have been added in quadrature.

Since the inclusive branching ratio B_{2n-1} falls rapidly with increasing n, it is assumed that contributions to the total decay rate from

TABLE 3. Measurements of B_5, the branching ratio of tau to five charged hadrons. Limits are at the 95% confidence level except where noted otherwise. The result listed for the MAC experiment is from a preliminary version of the analysis presented here.

Experiment	B_5 (%)
HRS[31]	0.13 ± 0.04
Mark II[32]	$0.16 \pm 0.08 \pm 0.04$
CELLO[33]	< 1.0
TASSO[21]	< 0.7
Mark II[27]	< 0.5
TPC[28]	< 0.3 (90% C.L.)
JADE[18]	$0.3 \pm 0.1 \pm 0.2$
MAC[26]	< 0.17

decay modes with charge multiplicity $2n - 1 \geq 7$, if any, are negligible and that $B_1 + B_3 + B_5 = 1$. Therefore, the 1-prong branching ratio is, by definition,

$$B_1 = 1 - B_3 - B_5 = (86.7 \pm 0.3)\%.$$

1.6.2 Measurements of the Tau Lifetime

A fundamental parameter of the tau is its lifetime. Measurements of the tau lifetime and electronic branching ratio and the muon lifetime can be compared for a test of the universality of the lepton couplings to the weak charged current. Results of the five experiments with significant contributions to the lifetime measurement are shown in Table 4.

TABLE 4. Measurements of the tau lifetime. The statistical and systematic errors of each experiment have been added in quadrature for the calculation of the average. The two results of the MAC experiment are from separate data samples.

Experiment	τ_τ ($\times 10^{+13}$ sec)
Mark II[34]	$2.86 \pm 0.16 \pm 0.25$
MAC[35]	$2.67 \pm 0.24 \pm 0.22$
MAC[26]	$3.15 \pm 0.36 \pm 0.4$
HRS[36]	$2.8 \pm 0.4 \pm 0.5$
TASSO[37]	$3.18^{+0.59}_{-0.75} \pm 0.56$
Average	2.84 ± 0.19

1.6.3 Tau Branching Ratios to Exclusive Channels

Table 5 summarizes the measurements of the tau branching ratios to exclusive channels. Gilman and Rhie[24] have made a careful study of how well the sums of the 1-prong and 3-prong portions of the measured exclusive decay modes agree with the measured inclusive branching ratios and find a discrepancy of about 7% in the 1-prong modes. One way to resolve the discrepancy is to assume that previous measurements of the tau lifetime and the leptonic branching ratios have yielded results below their true values; if the electronic branching ratio were increased to 19.3% (a 2.3 standard deviation change) then most of the discrepancy would go away. This is an unlikely solution, however, since many of the other measured branching ratios, which can be predicted from the electronic branching ratio, are consistent with both the measured tau lifetime and B_e. The most likely channels in which to look for this "missing" 7% are those with η's or multiple π°'s in the final state since the experimental results for these are either poor or non-existent.

TABLE 5. Tau branching ratios to exclusive channels. The results listed by the Particle Data Group[14] used to calculate the average muon and electron branching ratios shown here do not include the published results of this experiment.[41]

Decay mode	B_1 (%)	B_3 (%)	References
$\tau \to \nu_\tau e \bar{\nu}_e$	17.9 ± 0.6	-	14,38
$\tau \to \nu_\tau \mu \bar{\nu}_\mu$	17.1 ± 0.7	-	14,38
$\tau \to \nu_\tau \pi$	10.9 ± 1.4	-	14,38
$\tau \to \nu_\tau K$	0.67 ± 0.17	-	14
$\tau \to \nu_\tau \rho$	22.1 ± 1.2	-	8,39,40
$\tau \to \nu_\tau K^\star$	1.1 ± 0.3	0.3 ± 0.1	14,40
$\tau \to \nu_\tau\,(3\pi)$	6.0 ± 3.5	7.3 ± 0.5	39,10,38,26
$\tau \to \nu_\tau\,(4\pi)$	3.0 ± 2.7	5.3 ± 0.5	39,10,38,26
$\tau \to \nu_\tau K \bar{K}$	-	-	-
$\tau \to \nu_\tau K^\pm \bar{K}^\mp \pi^\pm$	-	$0.22^{+0.17}_{-0.11}$	14
$\tau \to \nu_\tau K^\pm \pi^\pm \pi^\mp (\pi^\circ)$	-	$0.22^{+0.17}_{-0.11}$	14
Sum	78.8 ± 4.8	13.3 ± 0.8	

1.7 Summary of Predictions

In order to test whether the tau lepton has the same couplings as the electron and muon to the weak neutral current it is possible to measure the polarization asymmetry A_P which is sensitive to g_v^τ.

Measurements of tau leptonic branching ratios and comparisons with the tau lifetime test the strength of the coupling of tau and ν_τ to the weak charged current. Also, precise measurements of the leptonic and pionic branching ratios add information to help resolve the discrepancy between the measured inclusive 1-prong branching ratio and the sum of the exclusive 1-prong branching ratios.

Finally, measurement of tau decay to five charged pions probes the axial-vector current in the region near the τ mass where no resonances are known.

CHAPTER 2

APPARATUS

This chapter contains descriptions of the apparatus used in this experiment.[42] A brief overview will be given first and more detailed descriptions of the detector components will follow. The experiment was performed at the PEP electron-positron storage ring at the Stanford Linear Accelerator Center in Stanford, California. Data were collected starting in the spring of 1981 until spring of 1984.† The products of electron and positron collisions at a center of mass energy of 29 GeV were observed with the MAC (MAgnetic Calorimeter) detector which was designed to provide lepton identification and hadronic energy measuring for 95% of the solid angle. The center of the MAC detector was a ten layer cylindrical drift chamber (CD) inside a conventional solenoid which provided charged particle tracking and momentum measuring for polar angles θ such that $|\cos\theta| < 0.95$. Surrounding the solenoid was a hexagonal barrel of lead sheets interspersed with proportional wire chambers (PWC's) for measuring electromagnetic showers with $|\cos\theta| < 0.8$. Surrounding these chambers was an iron hadron calorimeter of 5.5 absorption lengths also instrumented with PWC's. The ends of the central calorimeters were closed by endcaps consisting entirely of iron plates interspersed with PWC's. The calorimeters were enclosed by a hexagonal barrel of four layers of cylindrical drift tubes oriented transverse to the beam, except for the plane under the detector which

† After modifications to the detector, additional data, not used in this analysis, were collected from the fall of 1984 to the spring of 1986.

consisted of three layers of planar drift chambers. The ends of the detector were covered with six planes of drift tubes. The iron calorimeters were magnetized with a toroidal field and the outer drift system (OD) measured the bend angle of a charged particle emerging from the iron thus providing momentum measurement for muons. Scintillators, placed immediately inside the central hadron calorimeter and in the endcaps near electromagnetic shower maximum, provided trigger and time-of-flight (TOF) information. The total volume occupied by the detector was 400 cubic meters and it weighed 600 tons. Figures 3 and 4 show the main features of the detector.

2.1 Electron-Positron Colliding Beams

A two mile long linear accelerator was used to accelerate beams of electrons and positrons to an energy of 14.5 GeV and then the beams were injected into a storage ring (PEP) where they circulated, the electrons and positrons in opposite directions. Each beam consisted of three groups of particles ("bunches") that were equally spaced around PEP and therefore there were six points ("interaction points" or IP's) at which the beams collided. The number of times two bunches crossed each other (one "beam crossing") during one second at each IP was given by the circumference of PEP ($C_{\mathrm{PEP}} = 4400\mathrm{m}$), the velocity of the beams ($c = 3 \times 10^8 \mathrm{m/sec}$), and the fraction of the distance around the ring between each IP (1/6). There were therefore $c/(C_{\mathrm{PEP}}/6) = 409\,000$ beam crossings per second or one every $2.44\,\mu$sec. The radio frequency cavities used to supply the beams with energy to replace losses due to synchrotron radiation supply an electronic pulse which was used to determine when the next beam crossing was going to occur. This signal was an important component in the electronic logic that controlled the timing of the data acquisition system.

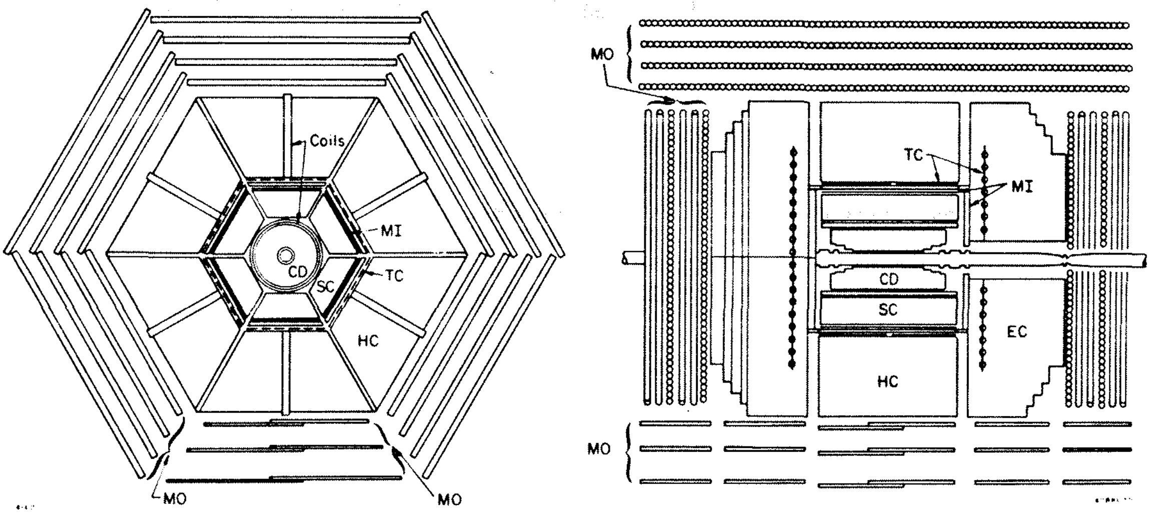

MAC Detector Components:

CD - Central Drift Chamber
SC - Shower Chamber (Central)
TC - Trigger/TOF Scintillators
HC - Hadron Calorimeter (Central)
EC - End-cap Shower and Hadron Calorimeters
MO, MI - Muon Drift Chambers
Coils - Solenoid and Toroid

FIGURE 3. Front and side views of the MAC detector. The left view shows the central section from along the beam axis. The right view shows the entire detector from the side.

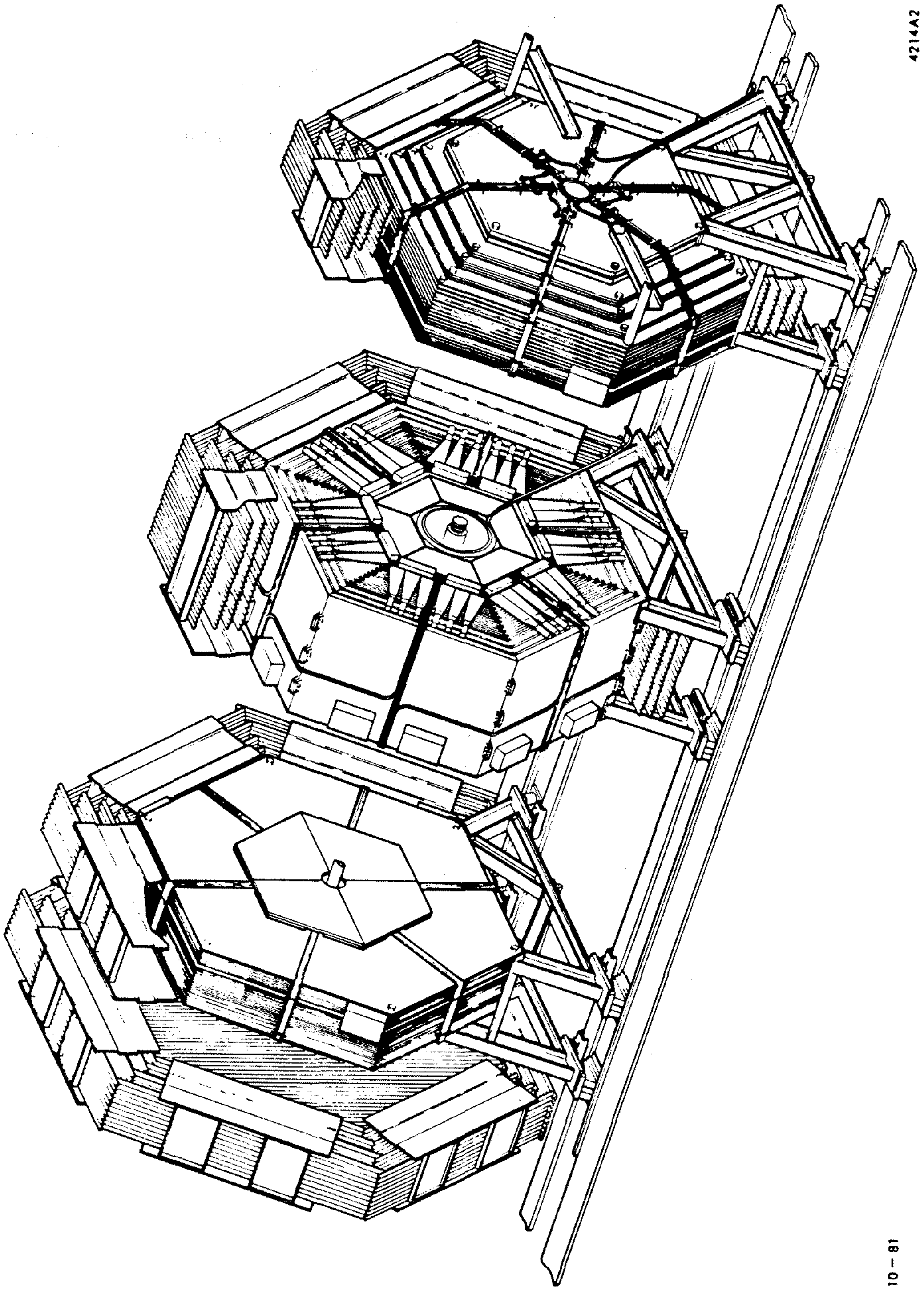

FIGURE 4. Isometric view of the detector. The endcaps are in their rolled-back positions (for repairs, etc.) and portions of the outer drift chambers have been omitted for viewing convenience.

2.1.1 Characteristics of the Interaction Point

Ideally the size of the IP would be smaller than the sensitivity of the detector and the location of the IP would coincide with the center of the detector. In reality neither of these conditions existed and also the location of the IP was subject to fluctuations. The volume in which e^+e^- interactions occurred was roughly an ellipsoid 16 mm long (along the beam axis), 0.5 mm wide (in the plane of the storage ring), and 0.1 mm high (out of the plane of the storage ring). These dimensions are the one standard deviation limits of approximately Gaussian distributions. The position of the centroid of the IP was monitored by the offline analysis.

2.1.2 Beam Energy

One of the experiments described in this thesis involves measuring the mean of a momentum spectrum. Since this measurement is directly sensitive to the beam energy, it was important to determine how well the beam energy was known. The energy of the beams was determined by the integral of the bend magnetic fields around the ring.[43] The current dependent field of each magnet was carefully measured and one magnet which was determined to have the average characteristics of the magnets used in the ring was set aside to serve as a monitor. The bend magnets were hooked up in series, including the monitor, so that they all received identical currents and therefore it was possible to keep track of the bend field. The quadrupole and sextupole focusing magnets also had small contributions to the integral of the bend field when the beams deviated from their ideal orbits at the centers of the focusing fields. The corrections that accounted for deviations from the ideal beam orbit amounted to less than 0.2% of the beam energy. The total error on the absolute beam energy was estimated to be less than 0.05%, including possible systematic biases of the rotating coil used to measure the magnetic field in the monitor magnet. The beam energy was a constant 14.50 GeV throughout the entire data sample used in this experiment. The amount by which the beam energy wandered, mostly due to changing orbits, was less than 0.2% and the width of the beam energy distribution was 0.1%.

2.1.3 Experimental Coordinate System

The z-axis of the right-handed coordinate system used by the detector event reconstruction and in this thesis was defined to be the direction in which the positron beam travelled through the experimental hall (the "interaction region" or IR). The x-axis was defined to point into the center of the storage ring and therefore the y-axis pointed vertically upward. The corresponding spherical coordinates are defined by

$$\begin{aligned} x &= r \sin\theta \cos\phi \\ y &= r \sin\theta \sin\phi \\ z &= r \cos\theta, \end{aligned} \tag{2.1}$$

where r was the distance from the origin and ϕ was the azimuthal angle ($\phi = 0$ for $x > 0, y = 0$) was used for most purposes.

2.2 Central Drift Chamber and Solenoid Magnet

The e^+e^- annihilations occurred inside an evacuated aluminium pipe ("beampipe") of radius 8.711 cm and thickness 0.178 cm. The central drift chamber (CD) surrounded the beampipe with 833 drift cells arranged in a cylindrical geometry consisting of 10 layers coaxial with the beams. The CD was inside a conventional solenoid which had a field strength of 5.7 kGauss. The CD provided charged particle tracking and momentum measuring for $|\cos\theta| < 0.95$.

The geometrical properties of the CD are listed in Table 6. The stereo angles which are listed in column 5 of the table are defined as the azimuthal rotation of one wire of a layer with respect to the center of the chamber. This property of the CD made it possible to measure polar angles and z-intercepts of charged particles.

TABLE 6. Physical parameters of the central drift chamber.

Layer	# cells	radius (cm)	length (cm)	stereo angle (mrad)
1	48	11.930	112.56	0
2	63	15.659	112.56	+50
3	78	19.938	140.42	-50
4	62	23.114	168.32	0
5	72	26.843	187.96	+50
6	82	30.571	187.96	-50
7	92	34.300	187.96	0
8	102	38.026	187.96	+50
9	112	41.755	187.96	-50
10	122	45.484	187.96	0

The entire CD was enclosed in a common gas volume. A 90% argon, 10% methane gas mixture was circulated through the chamber at three cubic feet per hour from three inputs at one end of the chamber to three outputs at the other end. The inner wall of the gas volume was a 0.2 cm thick aluminium pipe with an inner radius of 9.77 cm and the outer wall was a 0.64 cm thick stainless steel pipe with a radius of 47.8 cm. The endplates of the chamber were made from 1.9 cm thick plates of stainless steel with steps (the horizontal pieces of the steps were only 1.0 cm thick) for the shorter inner layers as shown in Figure 5. The total tension between the endplates exerted by the sense and field wires of the CD was about 9240 lbs or 4200 kg and was supported by the stainless steel outer wall.

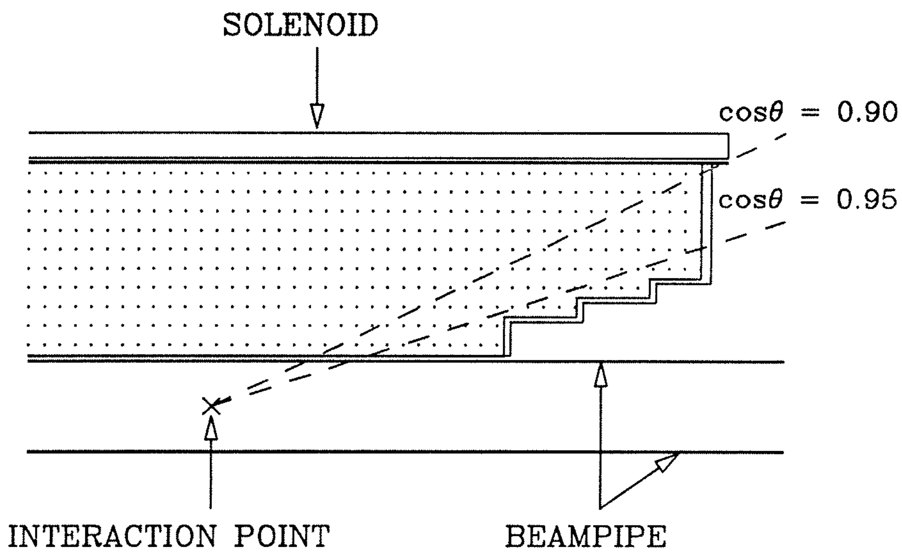

FIGURE 5. Cross section of central drift chamber.

The solenoid consisted of two layers of 16 aluminium windings which carried a current of 6000 amperes. Cooling for the magnet was accomplished by circulating chilled water in the hollow (a 1.1 cm hole) 3.75 cm wide by 2.45 cm deep aluminium windings. Additional cooling was provided by a water cooled jacket on the outer surface of the solenoid and by circulating chilled water through copper coils built into the stainless steel outer wall of the CD. These precautions kept the temperature in the region of the solenoid under $40°C$. Iron plates in the calorimeters (described in more detail in the calorimeter description) provided a return path for the field lines of the solenoid.

The structure of a drift cell is shown in Figure 6. The copper-beryllium field and field shaper wires were 200 microns in diameter and were suspended at a tension of 700 grams. The 20 micron sense wires were made of gold plated tungsten and were suspended at a tension of 55 grams. The sense wire pairs were connected to differential amplifiers at one end of the chamber, while the other ends were left floating, and the sign of an output voltage determined which half of a cell a track had traversed. The double sense wire cells were introduced primarily because 10 layers were not enough to reliably resolve the left-right ambiguity on the basis of a χ^2 test. The reduction in the number of combinations of hits it was necessary to try while reconstructing tracks also resulted in a substantial savings of computing time. Nevertheless, in events with two tracks the typical reconstruction time per track was 45 msec on the IBM 3081K computer at SLAC while in multihadron events in which the average charge multiplicity was ~13, the reconstruction time per track was 250 msec. The inner three layers had a smaller cell size in order to reduce the frequency of two tracks passing through the same cell.

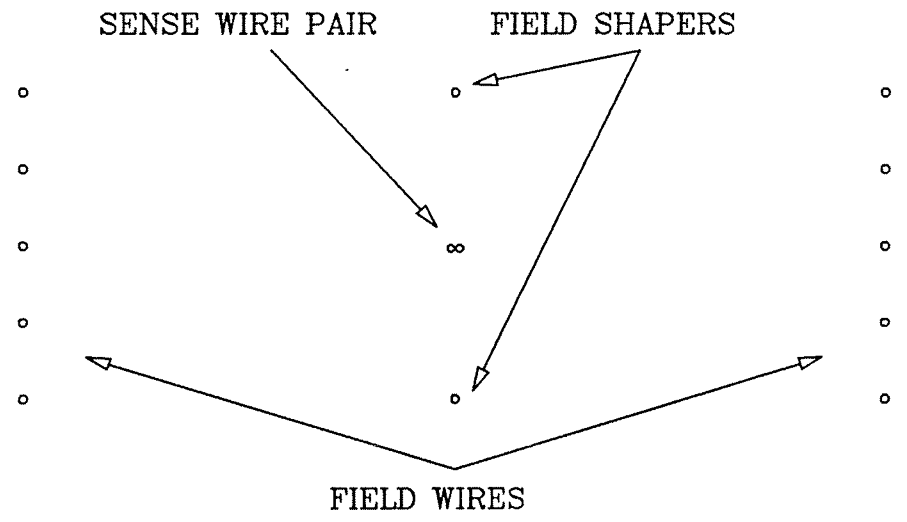

FIGURE 6. Structure of central drift chamber cell. The wire diameters are not to scale.

The sense-wire pairs were read out by differential preamplifiers mounted directly on one end of the chamber and the signals were fed to discriminators (DCD's) placed next to the detector. The polarities of the pulses fed to the discriminators were preserved in the polarities of the output pulses of the discriminators. These signals were then transported about 35 meters to time-to-voltage-conversion electronics (TVC's). A voltage ramp, common to all the TVC channels, was started at the beginning of the beam crossing interval and when a discriminator pulse arrived at a TVC channel, the current value of the ramp voltage was saved on one of two capacitors, depending on the polarity of the DCD signal. The other capacitor had the full value of the ramp voltage at the end of the beam crossing interval and an operational amplifier was used to compare the voltages so that the polarity of the TVC output voltages still preserved the information about which side of a cell was traversed by a charged track. The TVC voltages were digitized by scanning units upon the request of the trigger electronics and sent to the online computer.

A charged particle trajectory can be approximately described as a circle in the plane normal to the solenoid field direction and a straight line in a plane parallel to the solenoid which contains the track (tracks with momenta less than 40 MeV/c loop inside the CD and have a sinusoidal trajectory in the side view). This is the description of a helix. The parameters of a helix are the following:

- the curvature (1/radius) in the x-y plane;
- the polar or dip angle (θ), measured at the point of closest approach of a track to the origin;
- the vector between the origin and the point of closest approach of a track to the origin (measured only in the x-y plane), described in cylindrical coordinates (r_0,ϕ_0,z_0).

The first step in the track reconstruction was a search for a track consisting of at least five hits of which no more than three could be in the same view. The search began with a scan for hits in the outermost layer of the chamber. When a hit was found the next layer was scanned for hits that were within an azimuthal "road" between the first hit and the center of the chamber. The width of the road (3-4% of the circumference of the current layer) was large enough to be efficient at finding hits in the stereo layers and hits produced by low momentum particles. Hits were added to a candidate track in this manner until five hits (no more than three on the axial layers) were found and then a four parameter fit to the hits was performed. This preliminary fit assumed $r_0 = 0$ and was made to a linear approximation of a helix. If the χ^2 of the fit exceeded a fairly large value then a new fifth hit was searched for. If this failed then a new fourth hit was searched for, etc. When a five hit track candidate was found the track was extrapolated to the inner layers to search for additional hits. As each new hit was added to the track candidate (as a result of satisfying a χ^2 test), the track parameters were recomputed for extrapolation to the next layer. When all 10 layers had been searched in this manner the hits were fitted to a helix, this time without the approximations used to linearize the problem. Corrections to the hit positions were made due to:

- time-of-flight between IP and computed hit position (including the displacement of the hit along the sense-wire pair);
- distortions of the electron drift paths caused by the solenoidal magnetic field;
- the time delay for pulse propagation along the sense wires;
- a tilt of the endplates of the inner layers which inadvertently occurred from alignment errors made during construction.

After the search for tracks was completed, the tracks were examined to determine if pairs of them fitted a gamma conversion pair, kaon, or lambda hypothesis. The remaining tracks were fitted to the hypothesis that they all originated from a common vertex which was constrained (by an additional term in the χ^2) to be within the IP ellipsoid. Tracks with a large contribution to the χ^2 of the vertex hypothesis were removed from the main vertex and the event vertex was recomputed. Tracks which were fitted to the main vertex with a satisfactory χ^2 will be referred to as "vertex-fit" tracks.

Table 7 summarizes the performance of the CD. The point resolution of the Monte Carlo simulation was adjusted to reproduce the confidence level distribution (for an assumed value of the resolution) of track fits in the data. The other resolutions come from a comparison of input Monte Carlo track parameters with those of the track reconstruction. The average efficiency of detecting a charged track when it traversed an active cell† was about 97%.

2.3 Calorimeters

2.3.1 Central Section Electromagnetic Calorimeter

The central section electromagnetic shower chamber (CSC) surrounded the solenoid and central drift chamber with a hexagonal barrel of alternating layers of material with a short radiation length and proportional wires chambers (PWC's). The PWC's detected charged particles, either those produced in interactions with the radiators or charged particles that pass through the entire detector.

The radiator plates were made of type-metal (83% lead, 12%

---

† Typically about 5% of the cells were inactive: 0.5% had sense wires which were broken outside the CD; 0.6% oscillated at such a high rate that they were useless; 0.7% were broken inside the chamber (and had to be extracted carefully); 1.4% had their cathodes disabled because they produced noise which affected an intolerable number of nearby cells (usually in the same layer) or repeatedly tripped off high voltage supplies; and 1.8% had electronics which malfunctioned.

TABLE 7. Performance of the CD (resolutions).

parameter	resolution
hit position	200 microns
momentum	$\sigma_{\frac{1}{p}}/\frac{1}{p} = 0.052\,p(\,\mathrm{GeV}/c)\,\sin\theta$
phi	$\sigma_\phi = 0.2$ degrees
theta	$\sigma_\theta = 0.7$ degrees
impact parameter	$\sigma_{r_0} = 600$ microns
vertex z-position	$\sigma_{z_0} = 0.6$ cm

antimony, 5% tin) and were 0.254 cm thick, 218.0 cm long, and, depending on the layer, varied in width from 68.2 to 115.5 cm. At normal incidence each plate presented 0.39 radiation lengths.

A single layer gas (85% argon, 15% methane) PWC filled the 1.0 cm gap left between each radiator. The PWC's were constructed from channeled extruded aluminium plates with the channels aligned along the beam axis. A 40 micron stainless steel wire was suspended in the center of each channel. At the faces of the chamber the wires were grouped together to form 3 layers in depth and 32 azimuthal segments in each sextant. Layer 1 included the first 7 radiator/PWC planes, layer 2 included 13 planes, and layer 3 was comprised of the last 12 planes. The total radiation length in layers 1, 2, and 3 was 2.7, 5.1, and 4.7 respectively. Each azimuthal segment was composed of 33×1.8 cm wide channels in the first plane and up to 58 channels in the last plane. The wire groups were formed at both ends of the chamber and read out by low input-impedance amplifiers. Because of the 6Ω/cm resistance of the signal wires the ratio of the charge collected at either end of a wire group was a linear function of the z position of the charge deposition.

The signals read out for a wire group provided three independent measurements of a shower:

- ϕ, determined by the azimuthal segment which was hit;
- θ, determined by the ratio of the pulse heights;
- energy, determined by the sum of the pulse heights.

After being decoupled from the chamber with transformers, the signals were preamplified at the detector and transported to Sample, Hold, And Multiplex (SHAM) modules in CAMAC crates located just on the other side of the concrete wall which separated the detector from the rest of the IR. "Brilliant" (because of internal microprocessors) Analog to Digital Converters (BADC's) examined the voltages stored by the SHAM's, digitized them, performed pedestal subtractions (pedestals were measured at the beginning of each run), and reported the addresses and voltages of channels above a given threshold to the online computer.

2.3.2 Central Section Hadron Calorimeter

The central section hadron calorimeter (CHC) surrounded the CSC with a hexagonal barrel of 24 layers of 2.54 cm thick iron plates and three 10.16 cm thick iron plates with 1.90 cm gaps between each plate instrumented with PWC's. The CSC and CHC had identical gas and readout systems. The first 24 layers of PWC's were grouped into three layers of equal depth and 32 azimuthal segments per sextant. The first two layers were read out at both ends for z position measurement but the third was read out only at one end. The PWC's in the outer, thick plates were not read out for a large fraction of the data analysed in this experiment and were therefore not used here. The thickness of the entire calorimeter was 91.44 cm or 5.5 nuclear absorption lengths at normal incidence and thus served as an effective muon filter. The calorimeter iron, with the exception of the inner three plates, was magnetized with a water cooled aluminum toroid consisting of four turns around each sextant which carried a current of 2500 amperes; the magnetic field strength in the iron was about 1.8 Tesla. The inner three iron plates served as a return path for the solenoid flux and had stainless steel inserts to prevent the production of stray toroidal fields from the nearby toroid coils.

2.3.3 Endcap Calorimeters

The solid angle coverage of the central section calorimeters was completed by two endcap calorimeters which were mounted on rails so they could be moved when it was necessary to gain access to the central section to perform repairs. Each endcap consisted of 28× 2.54 cm thick iron plates instrumented in the 1.91 cm gaps between each plate with PWC's. There were also two 10.16 cm iron plates at the back of each endcap and a 2.54 cm thick plate mounted on the face of each endcap. The face-mounted plates had the same area as a cross section of the CSC and, along with the section of the first four endcap plates covered by the face-mounted plates, served as flux returns for the solenoid. The hexagonal plates were normal to the beam and apart from the solenoid flux returns were magnetized to a field strength of about 1.8 Tesla with toroids exactly like those in the central section.† The flux return section of the first four plates and the face-mounted plate had 7.6 cm wide stainless steel inserts placed parallel to the toroid coils which prevented the production of toroidal fields. Depending on polar angle each endcap was between 5.5 and 6.5 nuclear absorption lengths thick.

The endcap PWC's differed from those of the central section calorimeters. The anodes were 50 micron beryllium-copper wires which were

† All three toroids were connected in series to the same power supply to produce a field which was as uniform as possible.

strung approximately normal to radii from the beams and the cathodes were radial aluminum strips (see Figure 7). Both the anodes and cathodes were read out; this allowed the measurement of both ϕ and θ of an energy hit. The anodes were found to be less susceptible to noise and large pulse-height fluctuations and were used for energy measurement. Each plane of PWC consisted of 12 half-sextants as shown in Figure 8. The edges of the endcap PWC's were not active and therefore there were dead regions about 4-6° wide every 30°.

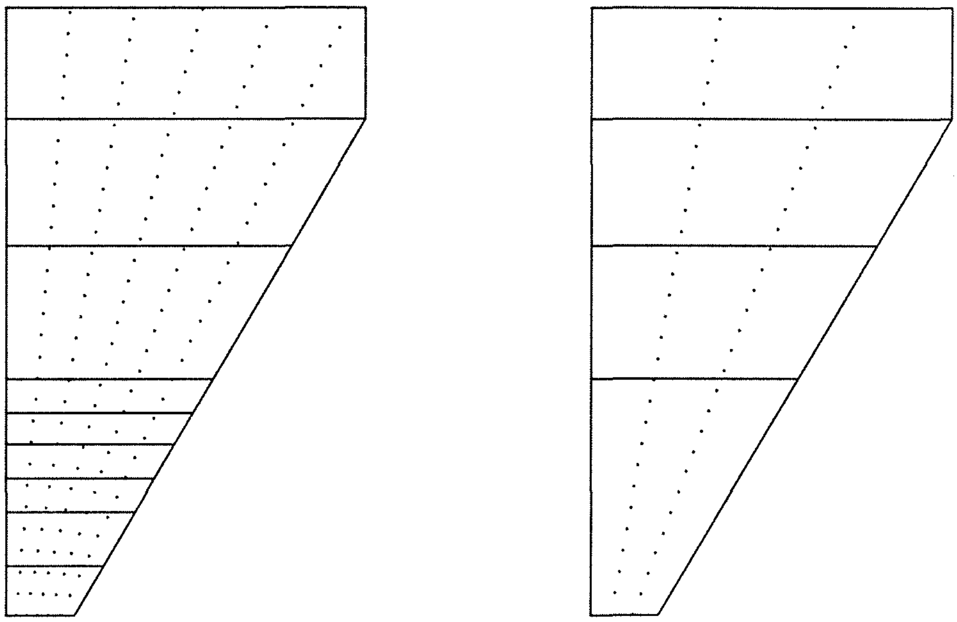

FIGURE 7. Segmentation of endcap PWC's. The PWC on the left shows the segmentation of the first nine PWC layers and the PWC on the right shows the segmentation of PWC layers 10-28. The horizontal solid lines indicate boundaries between anode wire groups and the dotted lines indicate boundaries between cathode strips.

The segmentation of the endcap PWC's near the interaction point was finer than in the rest of the endcap because this region (approximately 13 radiation lengths at normal incidence) served as endcap electromagnetic shower chambers (ESC's) and the rest of each endcap served as endcap hadron calorimeters (EHC's). The segmentation of the PWC's and the formation of

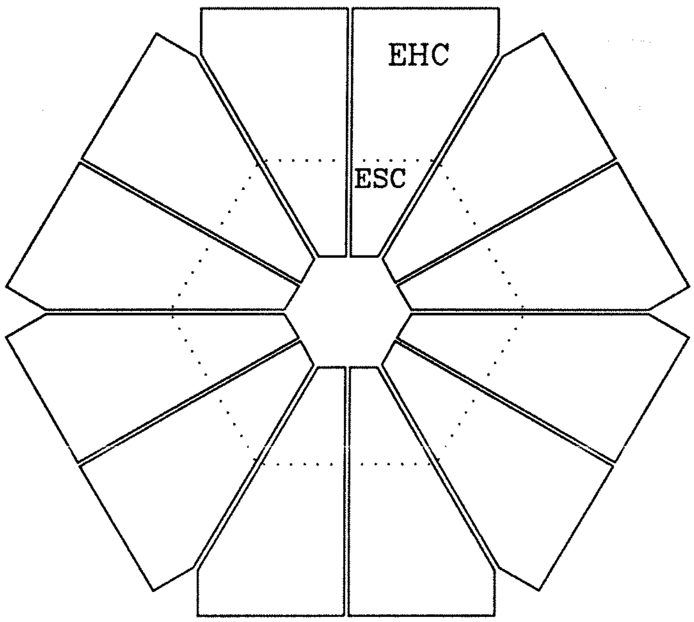

FIGURE 8. Geometry of endcap PWC's viewed from along the beams. The division of the first nine endcap PWC layers into the ESC and EHC is indicated by the dotted hexagon.

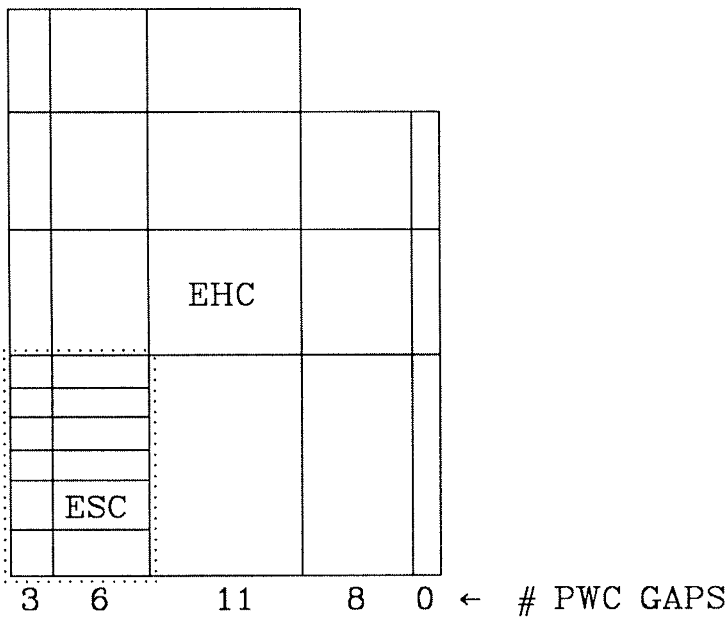

FIGURE 9. Side view of endcap segmentation. The division of the endcap into the ESC and EHC is indicated by the dotted box and the number of vertical PWC gaps in each layer is indicated across the bottom.

layers from the PWC planes is shown in Figures 7 and 9.

The endcap PWC's used the same 85% argon, 15% gas mixture as the central section calorimeters and the same readout electronics except that the preamplifiers were decoupled from the chambers with capacitors instead of transformers.

2.3.4 Calorimeter Summary

Table 8 summarizes the parameters and performances of the various calorimeters. Note that the CSC and ESC will be referred to as a unit as the SC and similarly the CHC and EHC will be referred to as the HC.

TABLE 8. Summary of calorimeter parameters and performance.

	CSC	ESC	CHC	EHC
# layers	3	2	3	2
# PWC planes	32	9	24	19
ϕ resolution (degrees)	0.6	1.2	1.0	3.0
θ resolution (degrees)	1.2	1.5	2.0	2.5
energy resolution $(\%/\sqrt{E}(\mathrm{GeV})$	23	45	75	75
total radiation lengths	12.4	12.9	51.7	39.0
total absorption lengths	0.5	1.4	5.5	4.1

2.4 Outer Drift Chambers

The outer drift chamber system (OD), shown in Figures 3 and 4 was used to identify muons and to measure their momenta. The chambers were designed with the goal of being able to measure muon momenta with a resolution that would be dominated by multiple scattering uncertainties at beam energy.† A straightforward calculation showed that the momentum error due to multiple scattering alone in the MAC detector was approximately $\sigma_{(1/p)}/(1/p) = 0.25$, where p is the momentum in units of GeV/c.[44]

The OD consists of three distinct subsystems:

- a hexagonal barrel of cylindrical drift tubes which covered all except the bottom sextant (hex chambers);
- three layers of planar drift chambers which covered the bottom sextant (bottom chambers);
- six layers of cylindrical drift tubes which covered the ends of the detector (endplug chambers).

The tubes used to construct the hex and endplug chambers were aluminum cylinders with 0.476 cm thick walls and radii of 5.0 cm. The gas filled (85% argon, 15% methane) tubes were grounded and 50 micron gold plated tungsten sense wires (which were operated at high voltage) were strung down the center of each tube.

The hex system tubes were oriented transverse to both the beams and the bend direction of a charged particle in the toroid spectrometer. Each layer consisted of 86 tubes per sextant or $4 \times 86 \times 5 = 1360$ tubes for the entire hex system. The middle layers were offset by 0.953 cm with respect to layers one and four to aid in resolving the left-right ambiguity during track

---

† The typical multiple scattering uncertainty at the OD for a 14.5 GeV muon passing through the MAC detector was approximately 0.6 cm.

reconstruction.

Each endplug consisted of six layers of 58 tubes or $2 \times 6 \times 58 = 696$ tubes for the entire system. The tubes in successive layers were oriented parallel to successive mid-sextant axes, i.e., there were two layers in each of three views. The gaps between layers were about 13 cm wide.

Because of the support structure for the detector it was more convenient to build the bottom chamber system out of planar, double sense wire drift chambers. The three layers had approximately 30 cm gaps between them. The chambers were 2.54 cm thick and the drift cells were 10.16 cm wide. The cathodes were grounded sheets of 0.08 cm thick aluminum foil and there were aluminum I-beams between the cells held at negative high voltage which served as field shapers. There were 360 channels total in the bottom chamber system.

The readout electronics for the OD were nearly identical to the CD electronics except that the tubular cells, having only a single sense wire, had dual-input differential preamplifiers with one input connected to ground.

Tracks in each of the three OD subsystems were reconstructed independently of the other two subsystems and independently of other pieces of the detector. Reconstructed OD tracks consisted of at least three (two, five) hits in the hex (bottom, endplug) system. Figure 10 shows a reconstructed track in the hex system. The reconstructed tracks were assigned momenta by extrapolating them back to the reconstructed CD vertex taking into account the bend due to the toroid spectrometer and energy losses in the material between the IP and the OD.

To be efficient at finding tracks in regions where the subsystems overlapped, a special tracking program (2HIT) which relied on already reconstructed CD tracks was developed. Central drift chamber tracks that didn't already match with an OD track were extrapolated to the OD and the

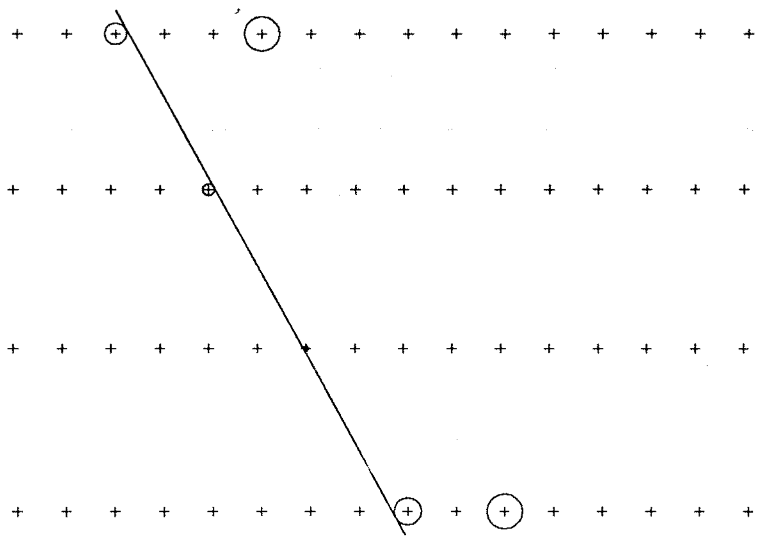

FIGURE 10. A reconstructed track in the hex part of the outer drift chambers. The crosses mark wire positions and the circles represent the equal time contours of hits. Note that the reconstructed track (the straight line) is tangent to the time contours.

χ^2 was formed for the match of the CD track to all possible OD tracks in that region consisting of two hits. If the best match passed a χ^2 cut then all pertinent information concerning that match was saved.

Because the OD measured momentum and polar angle, the matching χ^2 was formed from these two quantities. The errors in these quantities were formed from the quadratic sums of the CD errors (from the CD error matrix), the errors expected from multiple scattering, and a term, which was determined empirically, due to measurement errors in the OD system. Since both the CD and OD measure inverse momentum rather than momentum with gaussian errors, the inverse momentum was used in the χ^2 calculation. The correlation between inverse momentum and θ was accounted for correctly.

2.5 Time-of-Flight System

The time-of-flight of a particle in the MAC detector was measured by the TOF system which consisted of 144 plastic scintillation counters with photomultiplier tubes (PMT's) for scintillation light amplification and conversion into analog electronic pulses. With typical distances from the IP of 2-4 meters TOF hits on opposite sides of the detector caused by cosmic rays ($\beta \sim 1$) had a time difference of approximately 10 nanoseconds, while hits produced by tracks from e^+e^- annihilations occurred at roughly the same time. The two purposes of the TOF system were (1) to provide electronic signals notifying the trigger system of activity in the detector (details in the next section) and (2) to provide a means for reducing cosmic ray background during offline analyses.

The TOF counters covered 97% of the solid angle. The 36 counters in the central section formed a hexagonal barrel enclosing the central section electromagnetic calorimeter. The distance from the IP to the center of a sextant plane was 127.6 cm. Each of the counters was 112.4 cm. long (parallel to the beams) and 24.3 cm wide (transverse to the beams). Each sextant consisted of an array that was six counters wide and two counters long. Light produced by charged particles penetrating a TOF counter was brought to the PMT's through light guides connected to the scintillator faces at the ends of the central section. The light guides were bent at 90° angles and the PMT's laid along the faces of the central section. The positions of the central section TOF counters, light guides, and PMT's can be seen in Figures 4 and 3.

The other 72 counters provided particle detection at low angles and were placed, 36 in each endcap, in planes located at $z = \pm 158.7$ cm (between the sixth and seventh iron plates of the endcap calorimeter, the region in which electromagnetic showers deposited most of their energy). Unlike the central section, the light guides between the counters and the PMT's were not bent. The counters ranged in length from 213.0 cm. to 114.9 cm. and were 20.0 cm. wide. The arrangement of the TOF counters in an endcap can be seen in Figure 11.

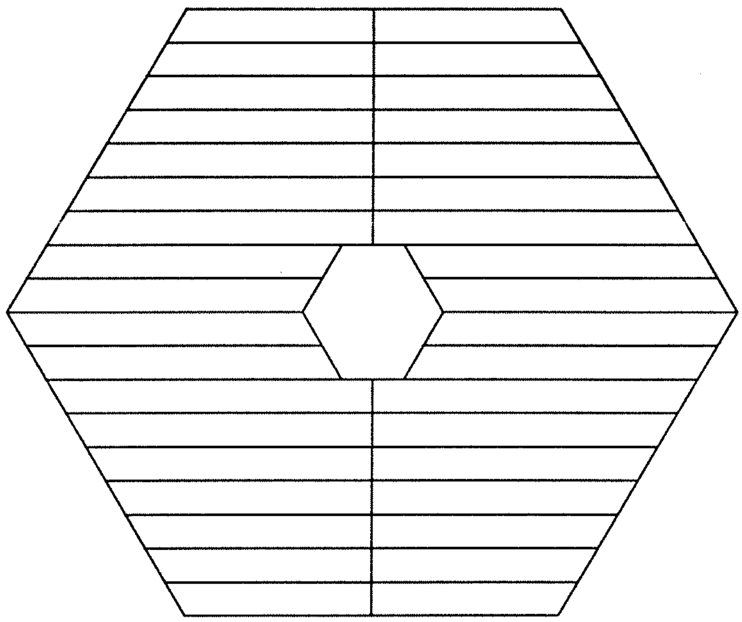

FIGURE 11. Endcap TOF counters viewed from along the beams. The dotted outline indicates the extent of the endcap calorimeter.

The signal from each PMT was divided and sent to a rise-time compensating discriminator and also to an analog-to-digital converter (ADC) for the pulse height of the signal to be digitized. The output of each discriminator was sent to the hardware trigger logic and also digitized by a time-to-digital converter (TDC) the output of which represented the time between beam collision and when the TOF counter in question was struck.

2.5.1 Time-of-Flight Calibration

Digitized times produced by the TDC's had to be corrected for the time delay between the TOF hit and the arrival of the signal at the input to the TDC's. Because of variations in the properties of the TOF counters, the PMT's, and the discriminator thresholds it was necessary to correct the TDC output times on a counter by counter basis. Such a calibration was performed at the beginning of each period of data accumulation (one "run" usually lasted from one to two hours). The calibration consisted of pulsing light-emitting diodes (LED's) that were placed on the light guides near the PMT's. The LED's were pulsed 40 times and the averages of the times produced by the TDC's were stored and included with the data record that was written to disk at the beginning of each run. In the offline event reconstruction the TDC raw times were corrected by the LED pulser calibration average times.

2.5.2 Offline Corrections to Time-of-Flight

Several additional corrections to the TOF measurements were made in the offline event reconstruction. The distance from the IP to the TOF system was not constant since the geometry of the TOF system was not spherical. Tracks reconstructed in the drift chamber were extrapolated out to the TOF system and the distance between the IP and the point at which an extrapolated CD track passed through a TOF counter was divided by c, the speed of light in vacuum, and subtracted from the LED-corrected time if that TOF counter was hit. A correction was also made for the time it took for light to travel, with a velocity of about $c/2$, from the point at which a TOF counter was struck to its PMT. A final correction was made to TOF measurements to accurately compensate for the dependence of the time on the pulse height of the signal measured by the ADC's (the rise-time compensating discriminators only partially compensated for this effect).

2.6 Hardware Trigger

While there existed the possibility of an interaction during each beam crossing, it wasn't possible to record the condition of the detector every 2.44 μsec due to the limited speed of the data acquisition system nor was it necessary since the actual rate of beam-beam interactions producing particles in the detector was less than 1 Hz. At typical PEP luminosities of $1.5 \times 10^{31}\,\mathrm{cm}^{-2}\,\mathrm{sec}^{-1}$ tau-pair events were produced at a rate of approximately 0.002 Hz. For these reasons it was necessary to make a decision after each beam crossing (the electronics were inhibited from processing signals except for a 40 nsec wide "gate" centered on the beam crossing interval) whether to reset all the electronics and wait for the next beam crossing or to inhibit the reset and instruct the data acquisition system to read the detector electronics and allow time for the data to be transferred to disk by the online computer (a Digital Equipment Corporation VAX 11/780). The decision making electronics ("hardware trigger") read out various detector signals and determined if a configuration of signals was likely to have been produced by an e^+e^- interaction. A description of how detector signals were formed into signals which caused a hardware trigger follows.

The discriminators of all 144 TOF counters were "latched" at read-out time. The latch signals were combined to form 14 signals corresponding to eight endcap quadrants (four at each end of the detector) and six faces of the central section hexagonal barrel.

The "Back to Back SCintillator" (BBSC) trigger was satisfied by TOF "hits" in either opposing endcap quadrants or opposing central section sextants. The "MULTiplicity" (MULT) trigger required three or more TOF hits in any of the six barrel faces or the two endcap planes.

The "Single MUon" (SMU) trigger made use of information from the central drift chamber, the TOF counters and the hadron calorimeter. A bit was set for each CD cell that had a signal during a beam crossing gate and the cells were formed into 18 slightly overlapping azimuthal wedges. A small angle wedge signal was formed if there were three or more hits in the inner five layers of a CD wedge and fewer than three hits in the outer five layers of the same wedge. A large angle wedge signal was formed if there were three or more hits in both the inner and outer five layers of the wedge. The central section TOF counters were grouped to form 18 wedges that overlapped the CD wedges in ϕ and the signals from the central section calorimeter were summed in a similar fashion. A large angle SMU trigger was satisfied by an azimuthal coincidence of a large angle CD wedge, a TOF wedge and an HC wedge (the energy threshold of the HC requirement was about 400 MeV). Since the endcap TOF counters were summed into quadrants due to their geometry, the corresponding CD wedges and endcap calorimeter energy sums were different from the ones in the central section. The small angle CD wedges were grouped to overlap a TOF quadrant and the endcap hadron calorimeter sextants were summed in a similar manner. A small angle SMU trigger was satisfied by an azimuthal coincidence of an endcap TOF quadrant, an EHC grouping with more than 400 MeV and a CD quadrant wedge. The trigger information used to form the SMU signal was saved for each logged event so that it was possible to determine which region of the detector caused the SMU trigger. This feature also allowed the SMU efficiency to be measured since an arbitrary number of SMU triggers could be present in an event.

The "ENERGY" trigger was formed from analog sums of the pulse height information in the calorimeters and TOF hits. The pulse heights were summed to form a total pulse height for each central shower chamber sextant, one for the entire central section hadron calorimeter and one for each endcap. The ENERGY trigger required at least two of nine signals consisting of: the six central section shower chamber sextant sums; the central section hadron calorimeter sum in coincidence with any central section TOF hit; and the two endcap sums in coincidence with a corresponding endcap TOF hit. The thresholds of the energy sum discriminators corresponded to roughly the energy deposition of a 2 GeV electromagnetic particle.

At the beginning of 1983 an additional hardware trigger was constructed which was designed to detect single electromagnetic showers in the CSC. This trigger was operational in about one-half of the data sample. The "Single ELectromagnetic particle" (SEL) trigger was satisfied by having at least two adjacent layers in the same sextant of the central shower chamber with more than 300 MeV and a total energy in that sextant above 2 GeV.

The primary trigger for tau-pair events was the SMU trigger since most events contained either muons or pions. The ENERGY trigger was moderately efficient until approximately the same time that the SEL trigger was installed. At this time the ENERGY trigger thresholds were almost doubled, rendering it much less efficient, and for one-third of the data (overlapping the period when the SEL trigger was active) five of the six CSC sextant energy sums malfunctioned and were essentially inactive. The SEL trigger efficiency more than made up for the deterioration of the energy trigger in the central section. The BBSC and MULT triggers also had moderate trigger efficiencies except for events containing electrons since the central section TOF counters were placed after the CSC.

2.7 Data Collection and Management

A data taking cycle ("run") began with the filling of PEP with electron and positron beams. When the beam orbits had been adjusted to produce collisions, the high voltage systems of the detector were turned on and calibration procedures for the detector were started. The calibrations took approximately five minutes and then data were collected for approximately the next two hours, until the beams needed to be replenished. At the end of the run the data file which had been written to disk was closed and a flag was set to notify the offline computer (the SLAC Computing Services IBM 3081K and 3033U computers) that the file was available for transfer. A continuously running process on the IBM checked every two hours for new data files on the VAX and if any were found, they were transferred to disk on the IBM, written to tape, and a job was submitted to perform the first pass analysis (PASS1) on each new file. The PASS1 filter further refined the data sample, rejecting approximately 90% of the logged events which consisted mostly of cosmic rays, noise, and beam-gas interactions. Large fractions of the filtered data (called "SLO" files) were left on disk during the course of a year to allow physicists easy access to the data. As the disks filled up, space was made available by moving the SLO files to tapes. The strategy adopted for most analyses was to process the SLO data through yet another filter (PASS2) which was tailored for a specific analysis and resulted in a data set small enough to reside on disk permanently or on a reduced number of tapes.

CHAPTER 3

EVENT SELECTION

3.1 Final States

The process of forming a sample of tau-pair events consists of rejecting all possible backgrounds. The large variety of final states necessitates the consideration of a large number of different background processes. There are 14 decay modes listed in chapter 1 and these can be combined to form 105 final states. Fortunately many final states are quite similar and can be formed into a smaller number of groups. The six distinct decay products (neglecting neutrinos) are e, μ, one charged hadron (π and K), one charged hadron plus neutrals (ρ and single charged particle decays of $A_1, K^\star, Q_1, Q_2$, and ρ'), three charged hadrons and possibly neutrals (contributions from $K^\star, A_1, Q_1, Q_2$, and ρ'), and five charged hadrons and possibly neutrals. For many purposes it is useful to classify tau decays simply by charge multiplicity: Decays producing one (three, five) charged particles(s) are called "1(3,5)-prong" decays respectively. This scheme is complicated by the facts that a fraction of 1(3,5)-prong decays are reconstructed with two (two or four, four) charged tracks respectively and that there are secondary vertices. Tracks in reconstructed e^+e^- photon conversion pairs are not counted as prongs but those in reconstructed K_s^0 vertices are counted. The reconstruction efficiency for the latter is much smaller than for the former.

3.2 Backgrounds

Several tau-pair final states have such large backgrounds that no attempt was made to keep events with these final states. The 2-prong final states in which both of the prongs were either electrons or muons were ignored due to enormous backgrounds from the processes

$$e^+e^- \to e^+e^-(\gamma), \tag{3.1}$$

$$e^+e^- \to \mu^+\mu^-(\gamma), \tag{3.2}$$

$$e^+e^- \to (e^+e^-)e^+e^-, \tag{3.3}$$

$$e^+e^- \to (e^+e^-)\mu^+\mu^-, \tag{3.4}$$

and background from cosmic rays. The cross sections of two-photon processes 3 and 4 are largest when the initial state electron and positron scatter at low angles and do not appear in the detector. The ee and $\mu\mu$ final states constitute roughly 6% of all produced tau-pairs.

Final states where both taus decay into a 3-prong or 5-prong have large backgrounds from the processes

$$e^+e^- \to q\bar{q}(\gamma), \text{ and} \tag{3.5}$$

$$e^+e^- \to (e^+e^-)q\bar{q}. \tag{3.6}$$

Since events with three or more prongs from each tau decay constitute only 2% of produced tau-pairs, eliminating them from the event selection reduces the background appreciably while reducing event selection efficiency only slightly.

Background from the process

$$e^+e^- \to (e^+e^-)\tau^+\tau^- \tag{3.7}$$

turned out to be the largest background in the final sample, since it closely resembles the signal.

3.3 Event Selection Requirements

The list of selection criteria ("cuts") used to form the general tau-pair data sample are listed and described here. Since the momentum resolution of the CD was rather poor, especially for tracks with the full beam energy, many cuts were needed to reject large backgrounds from processes such as $e^+e^- \rightarrow e^+e^-(\gamma)$. Because of the large number of cuts, they are formed into groups for the discussion which follows, and the motivation for each group is given. The most complicated cuts were designed to reject a very small fraction of real tau-pair events while removing background from the sample. Many of these were developed as physicists examined displays of background events and observed what requirements would remove them from the sample. The effect of the cuts on a Monte Carlo sample of events (with full detector simulation) was monitored and also guided the development of the cuts. In order to gain confidence that the Monte Carlo was able to simulate correctly the quantities which were used to select the tau-pair data sample (and thus reliably estimate the selection efficiency), various distributions of the selected data were compared with the predictions of the Monte Carlo. A representative sample of some of the more important distributions has been included with the discussion of the cuts. The Monte Carlo curves which are compared with the data do not include backgrounds.

1. Events were required to have at least two and no more than six CD tracks of which at most two were allowed to come from reconstructed photon conversion pairs. One track was required to be separated from all others (excluding pair conversion tracks) by at least 120° and the charged particle sphericity was required to be less than 0.05. In events with little activity in the HC (less than 4 GeV in the HC or fewer than 9 hits in the CHC and fewer than 2 in the EHC), the

transverse momentum of the two prongs (or the isolated prong and the prong with the largest momentum in multi-prong decays) with respect to the thrust axis† was required to be less than 1.5 GeV/c. The transverse momentum distribution for events in the final sample is shown in Figure 12. These requirements reduced the background from beam-gas interactions and multi-hadron events produced in e^+e^- annihilation and two-photon collisions.

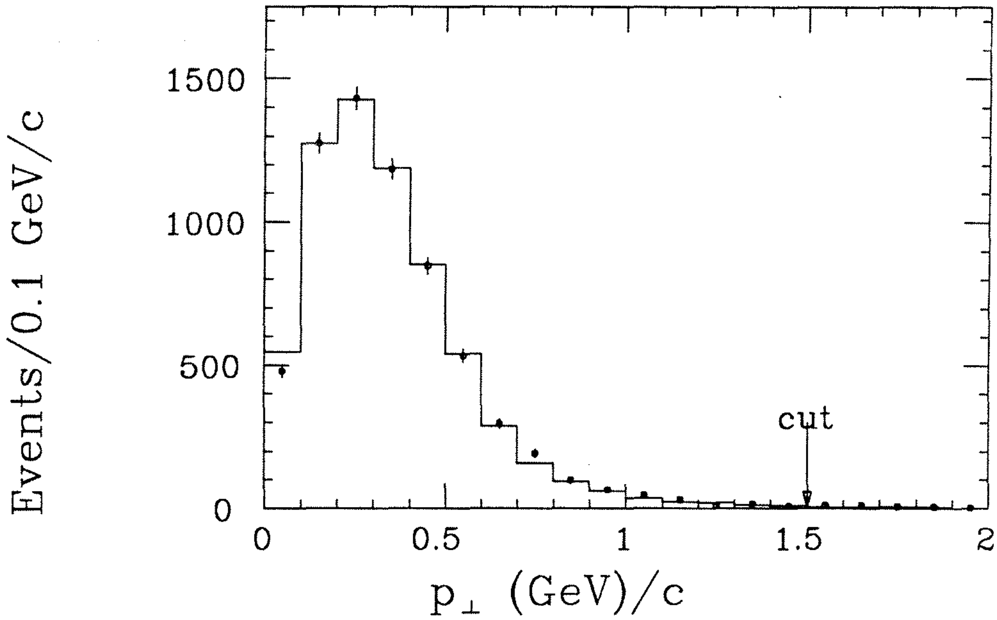

FIGURE 12. Transverse momentum ($p_\perp$) of 2-prong events and of isolated prong and jet prong with the largest momentum in 4-prong events. The solid line is for the Monte Carlo. The maximum $p_\perp$ under the conditions described in cut 1 of section 3.3 is indicated.

---

† The thrust axis $\hat{T}$ maximizes the thrust:

$$T = \frac{\Sigma_i |\vec{p_i} \cdot \hat{T}|}{\Sigma_i |\vec{p_i}|},$$

where $\vec{p_i}$ are momentum vectors. It is straightforward to show that the thrust axis for a system of two particles is $\hat{T} = (\vec{p_1} - \vec{p_2})/(|\vec{p_1} - \vec{p_2}|)$.

2. Events with two prongs were removed from the sample if both prongs were identified as electrons and there were no neutral showers present. This removed background from processes with only electrons in the final state, i.e., $e^+e^- \rightarrow e^+e^-$ and $e^+e^- \rightarrow e^+e^-e^+e^-$.
3. The total energy in the calorimeters was required to be greater than 6 GeV and the scalar sum of the CD momenta was required to be greater than 2 GeV/c. This reduced the background from all two-photon collision processes, cosmic rays, and the process $e^+e^- \rightarrow \mu^+\mu^-(\gamma)$. Figure 13 shows the effect of the 6 GeV energy requirement.

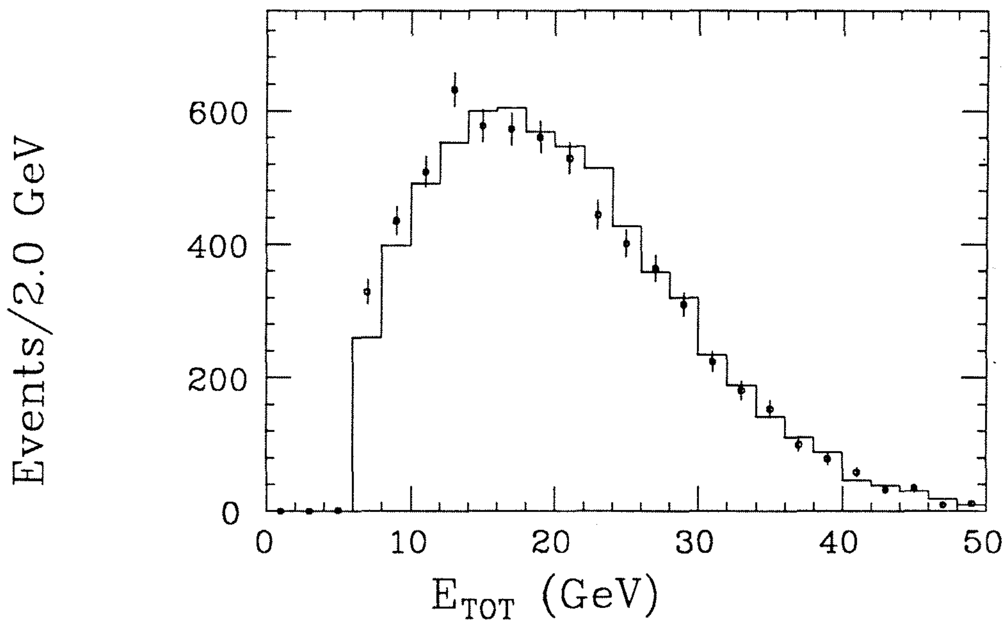

FIGURE 13. Total energy in the detector of selected events. The energy was calculated from constants appropriate for the mix of hadronic and electromagnetic energy found in multi-hadron events. The solid line is for the Monte Carlo. The minimum energy cut at 6 GeV is apparent.

4. Events with two prongs were rejected if both prongs were identified as electrons or the total energy in the electromagnetic calorimeters, calculated from constants appropriate for electromagnetic showers, was greater than 23 GeV. However, events were not rejected if one

track was identified as a muon, or if there was sufficient activity in the hadron calorimeter (more than 5 GeV and either at least seven hits in the CHC or at least two hits in the EHC) and one track was at least 1.5 (3.0) degrees from all sextant boundaries in the central section (endcaps) or 3.0 degrees from all mid-sextant planes in an endcap. These requirements were mostly effective for reducing the background from the process $e^+e^- \rightarrow e^+e^-(\gamma)$. The SC energy distribution after all cuts is shown in Figure 14.

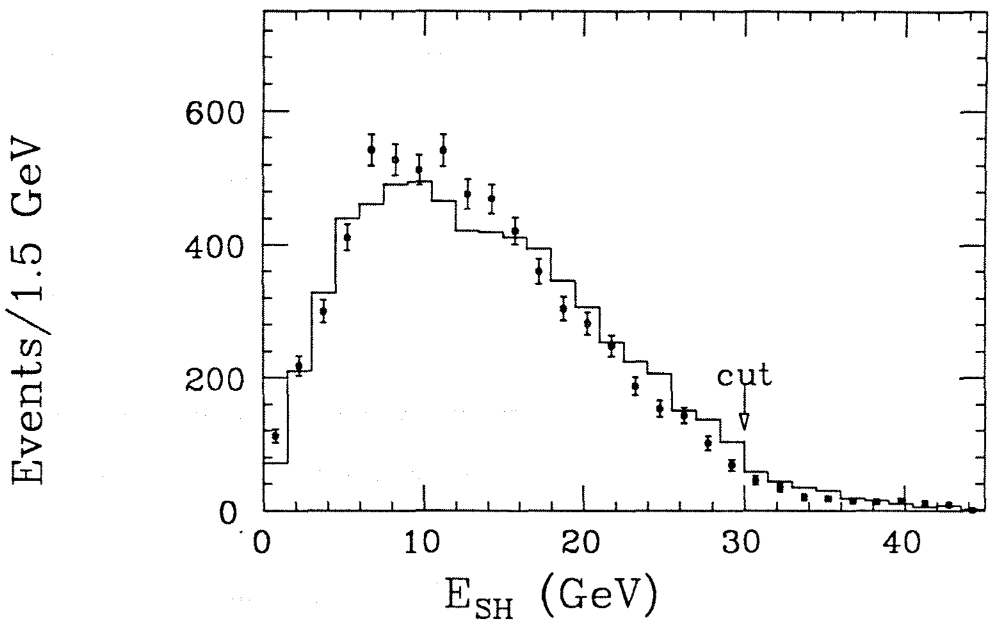

FIGURE 14. Total energy in the SC for selected events. The energy was calculated using constants appropriate for the mix of hadronic and electromagnetic energy found in multi-hadron events. The solid line is for the Monte Carlo. The energy cut (calculated using multi-hadron constants) which was applied under various conditions described in section 3.3 is indicated.

5. Events with total energy in the HC less than 8 GeV and total energy in the HC which was matched to CD tracks less than 5 GeV were rejected if there were two adjacent scintillator hits in both endcaps or more than 4 GeV in the CSC and two adjacent scintillator hits in at least one endcap. Since the endcap scintillators were located near

electromagnetic shower maximum and covered the dead regions of the endcap PWC's efficiently, these requirements served to reduce background from the process $e^+e^- \rightarrow e^+e^-(\gamma)$ in events where the CD tracks were poorly measured and the total energy was low due to the dead regions of the endcaps.

6. Events from the process $e^+e^- \rightarrow e^+e^-(\gamma)$ at very low angles tended to produce showers in the staircase shaped endplates of the CD, resulting in many stray CD hits and poor quality tracks that were not easily identified as electrons. Therefore an event was rejected if it had more than 30 hits in the CD, less than 2 GeV in the HC, no identified muons, at least two "bad" tracks (only five hits) or fewer than two "good" tracks (good vertex fit and at least eight hits), and some indication of activity at very low angles in the endcaps (at least one endcap TOF hit with either a second endcap TOF hit , more than 3 GeV in the ESC, or more than 5 GeV in the SC). This extremely complicated requirement was effective at rejecting most staircase events while leaving the signal virtually untouched.

7. Several requirements were made of electromagnetic showers matched to CD tracks regardless of whether or not the CD tracks were identified as electrons. In order to describe this rather complicated set of requirements it is necessary to define two variables: E_{sh} is the energy in the electromagnetic calorimeters matched to a CD track and E_e is the weighted average $(1/\sigma^2)$ of CD momentum and E_{sh}. The momentum errors came from the error matrix for the CD and the error in the shower energy was assumed to be the empirical energy resolutions of the CSC and the ESC for electromagnetic showers. Events were rejected if, for either track in a 2-prong event or the isolated track in all other events, E_e was greater than 8 GeV

or E_{sh} was greater than 12 GeV and either $|\cos\theta|$ of the shower was greater than 0.6 or the ratio of the track matched energy in the HC to E_e was less than 5%. Also, for 2-prong events, one of the tracks was required to have $E_e|\cos\theta| < 4$ GeV and $E_{sh}|\cos\theta| < 7$ GeV. These cuts removed events with hard electrons at low angles, i.e. , events from the process $e^+e^- \rightarrow e^+e^-(\gamma)$ and all two-photon collision processes.

8. Background from the processes $e^+e^- \rightarrow \mu^+\mu^-(\gamma)$ and $e^+e^- \rightarrow e^+e^-\mu^+\mu^-$ as well as cosmic rays was reduced by rejecting events containing two prongs where both prongs satisfied a loose muon identification and there were no neutral showers in the SC.
9. In order to reduce the background of radiative events from the process $e^+e^- \rightarrow e^+e^-(\gamma)$ that passed the previous requirements and contained neutral showers, all events with two tracks and at least one electron and exactly one neutral shower were fitted to the kinematic hypothesis of $e^+e^- \rightarrow e^+e^-\gamma$ with the SQUAW fitting package and rejected if the fit had an acceptable χ^2. The background from radiative events produced by the process $e^+e^- \rightarrow \mu^+\mu^-(\gamma)$ was reduced with a similar SQUAW fit.
10. Events for which the total number of hits in the HC was less than 10 and the quantity consisting of the sum of the total energy in the SC and 2.5 times the second largest of the prong momenta was greater than 55 were rejected. This quantity was chosen due to the clear separation of the signal and background from the process $e^+e^- \rightarrow e^+e^-(\gamma)$.
11. Unless there was more than 5 GeV in the HC or four or more tracks in an event where the isolated track was a muon, the quantity formed from the sum of the total energy in the calorimeters and twice the

scalar sum of the prong momenta was required to be larger than 15 GeV. This cut was designed to reduce the background from the processes $e^+e^- \to e^+e^-e^+e^-$ and $e^+e^- \to e^+e^-\mu^+\mu^-$.

3.4 Additional Requirements for 2-prong Events

In order to further reduce the background from processes with only electrons and/or muons in the final state (especially the process $e^+e^- \to e^+e^-(\gamma)$) and cosmic ray events, events with two prongs were required to satisfy some additional criteria. Except for radiative events in which the photon is at a large angle from the beam or carries off a large fraction of the beam energy, the two tracks in events from the processes $e^+e^- \to e^+e^-(\gamma)$ and $e^+e^- \to \mu^+\mu^-(\gamma)$ tend to be collinear† and coplanar.‡ Events produced by two-photon collisions, except those in which the initial state electron or positron is scattered at a large angle, also tend to be coplanar. Since tau-pair events include two or more neutrinos, the angles between CD tracks tend to be much larger. Therefore it was required that both the acollinearity and acoplanarity angles of the two prongs be greater than 1° unless there was more than 8 GeV in the HC. The distributions of these two variables in the

---

† The acollinearity angle ξ is defined by:

$$\xi = \pi - \cos^{-1}\left(\frac{\vec{p_1} \cdot \vec{p_2}}{|\vec{p_1}||\vec{p_2}|}\right).$$

‡ The acoplanarity angle ψ is defined by:

$$\psi = \pi - \cos^{-1}\left(\frac{p_{1x}\,p_{2x} + p_{1y}\,p_{2y}}{\sqrt{p_{1x}^2 + p_{1y}^2}\,\sqrt{p_{2x}^2 + p_{2y}^2}}\right).$$

tau-pair data are shown in Figures 15 and 16. Apart from the peak at 0, the acoplanarity distributions of two-photon collision processes are fairly flat and therefore the acoplanarity angle was also required to be smaller than 40°. Background from the processes $e^+e^- \rightarrow e^+e^-(\gamma)$ and $e^+e^- \rightarrow \mu^+\mu^-(\gamma)$ was further reduced by requiring one of the CD tracks to have a momentum less than 10 GeV/c.

Cosmic ray background was reduced by rejecting events for which the primary vertex was more than 5.0 cm from the beam centroid along the z-axis or more than 0.5 cm from the beam centroid in the x-y plane. The distributions of these variables in the tau-pair data sample can be seen in Figures 17 and 18. Additional cosmic ray rejection was achieved by rejecting events in which the time difference between two scintillator hits on opposite sides of the detector was greater than 8 nsec, i.e. , the time difference was inconsistent with a pair of particles produced at the IP (this time difference was typically about 10 nsec for cosmic ray events as shown in Figure 19). Since cosmic rays only rarely crossed the interaction point, the vertex constraint on the CD track fits tended to pull the vertex away from the true point of closest approach of the cosmic ray to the beam centroid, especially along the beam direction. The problem was exacerbated by the fact that cosmic rays also tended not to arrive in coincidence with beam crossing and therefore confused the time to distance conversion of the CD hits resulting in poor quality CD tracks. In order to reject these problematic events, and to reduce the cosmic ray background in general, cut 9 in the previous section and the vertex position cut described above were repeated after the hits on the CD tracks were used to construct a single track across the diameter of the CD. This diametric fit, in addition to giving a more accurate measurement of the point of closest approach to the beam centroid, improved the quality of the matches between the CD and the rest of the detector and therefore improved

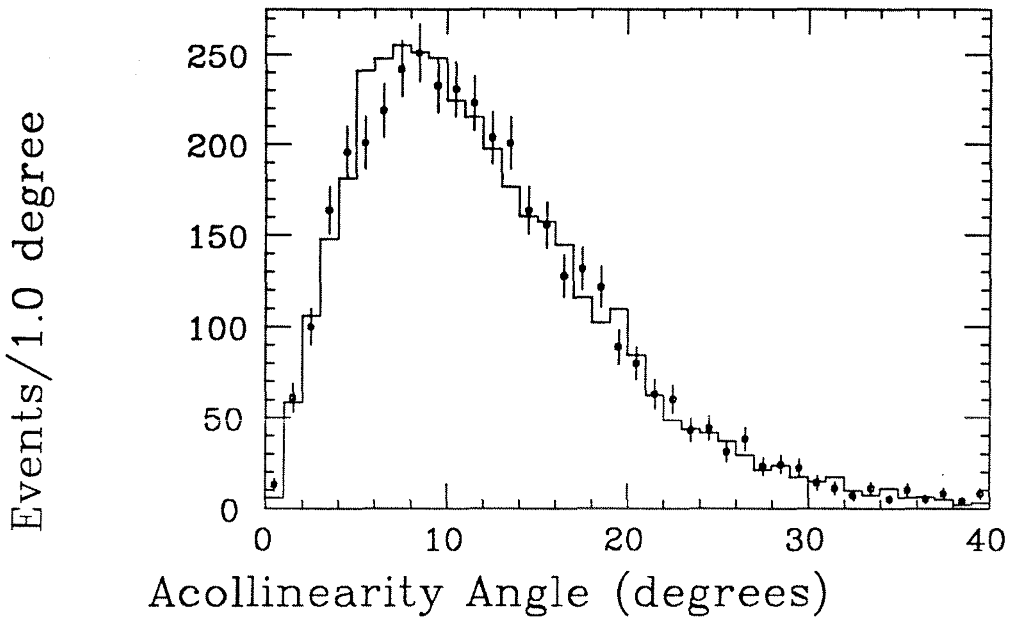

FIGURE 15. Acollinearity angle distribution for two prong events. The solid line is for the Monte Carlo.

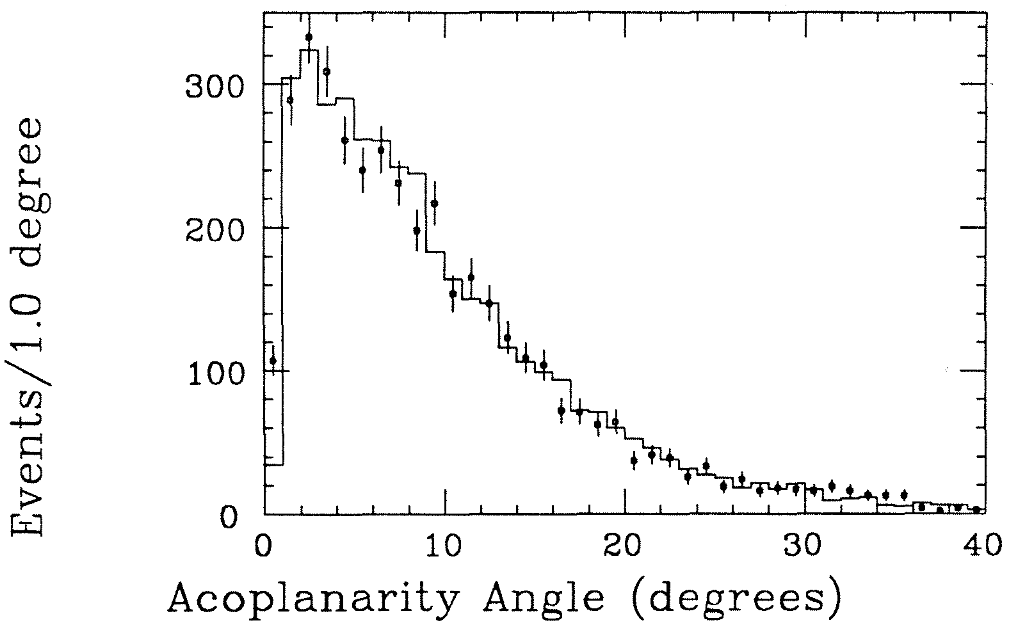

FIGURE 16. Acoplanarity angle distribution for two prong events. The solid line is for the Monte Carlo.

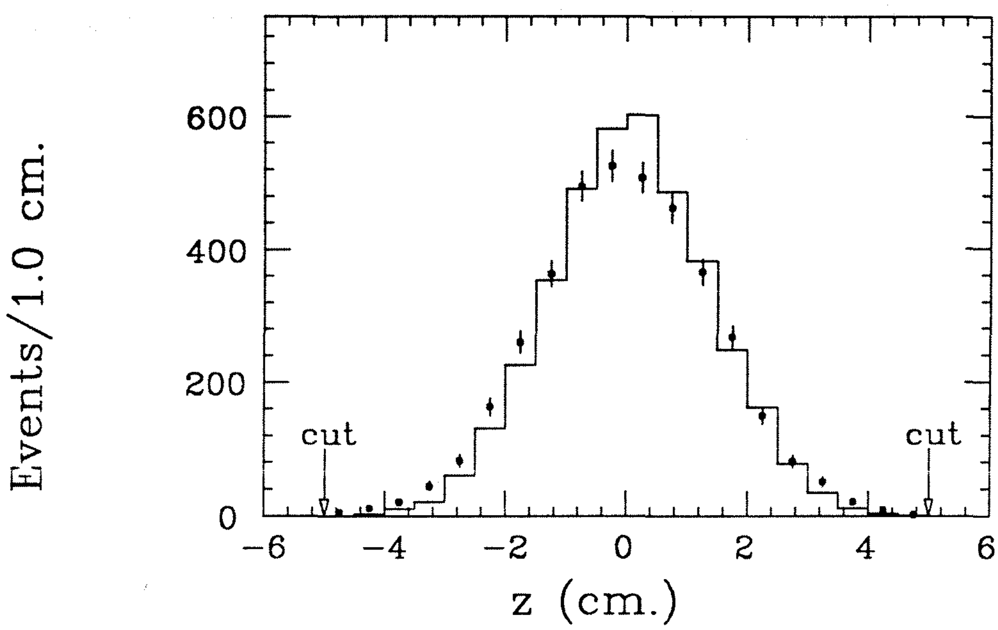

FIGURE 17. Distance from vertex to beam centroid along z-axis for selected events. The solid line is for the Monte Carlo. The maximum allowed $|z|$ for 2-prong events is indicated.

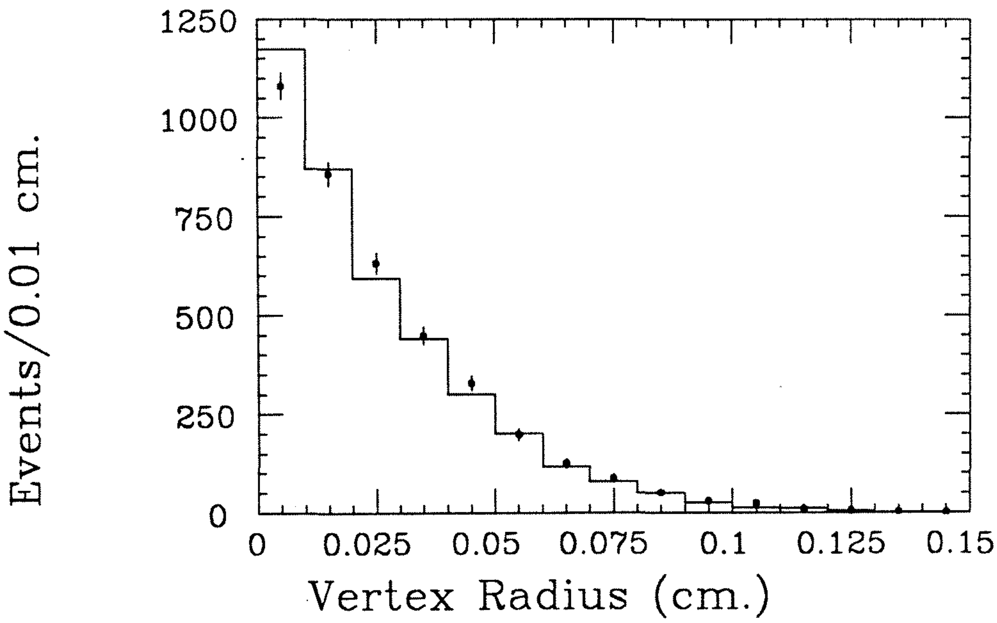

FIGURE 18. Radial distance from beam centroid to vertex for all events. The solid line is for the Monte Carlo. The maximum allowed radius for 2-prong events was 0.50 cm.

the muon identification efficiency for cosmic ray events. Most of the events rejected by this procedure were cosmic rays but a small fraction of them were produced by the processes $e^+e^- \to \mu^+\mu^-(\gamma)$ or $e^+e^- \to e^+e^-\mu^+\mu^-$.

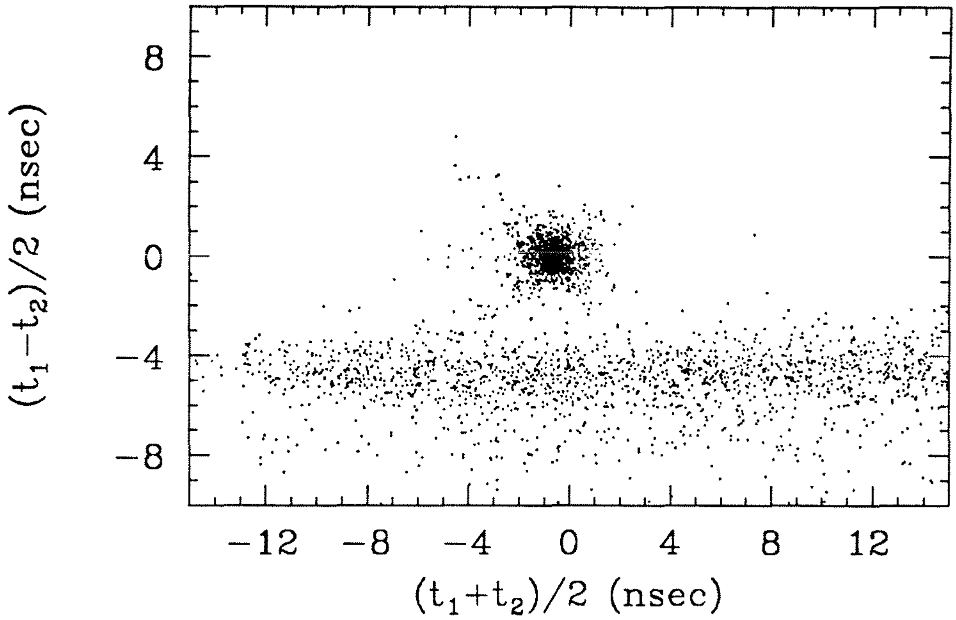

FIGURE 19. Average time and time difference for events in the raw data with two CD tracks and at least one reconstructed OD track. The TOF hits at times t_1 and t_2 were ordered such that t_1 was in the upper half of the detector. The cosmic ray band at $(t_1 - t_2)/2 = 5$ nsec is clearly seen. Note that the width of the beam crossing gate was ± 22 nsec.

3.5 Special Treatment of Events with Three Charged Tracks

It was important to allow three track events in the sample to be able to investigate possible systematic errors introduced by incorrectly modeling the track separation resolution. The most significant backgrounds for events with three tracks are from the two-photon collision processes $e^+e^- \to e^+e^-e^+e^-$ and $e^+e^- \to e^+e^-\mu^+\mu^-$. Events with three tracks were rejected if the total energy in the HC was less than 4 GeV or two of the tracks were identified as muons or two of the tracks were electrons and the third was a muon. In order to reduce the background from the process $e^+e^- \to e^+e^-(\gamma)$

with this charge topology (due to various problems causing a third track to be reconstructed) it was required that at least one of the tracks have a momentum less than 10 GeV/c and that all three tracks be fitted to the primary vertex with a satisfactory χ^2. Also, events containing two electrons or with a total energy in the SC of more than 23 GeV were removed unless there was also either a loose muon or more than 5 GeV in the HC and the crack cut described in item 4 of section 3.3 was satisfied.

3.6 Cuts Unique to Events with Four CD Tracks

This set of requirements was designed to reduce background from the processes $e^+e^- \rightarrow e^+e^-(\gamma)$ and $e^+e^- \rightarrow e^+e^-e^+e^-$. Events from the former that survived the previous cuts tended to have unreconstructed conversion pairs, poor quality tracks, and the isolated track was not labeled as a high energy, low angle electron. Events were rejected if two or more momenta in the jet were less than 0.75 GeV/c, the total energy in the HC was less than 1 GeV, two jet tracks had an invariant mass (assuming the tracks were electrons) less than 75 MeV/c^2, and either the total energy in the SC was greater than 20 GeV or two of the four tracks were identified as electrons. Events were also rejected if they contained no neutrals, there was more than 20 GeV in the SC and less than 5 GeV in the HC, the maximum CD momentum was greater than 7 GeV/c, the minimum momentum in the jet was greater than 3 GeV/c, and two jet tracks had an invariant mass of less than 75 MeV/c^2 (again assuming that they were both electrons). Events which were such a mess in the central drift chamber that the track reconstruction was extremely unreliable were removed by requiring that the isolated track and at least one other track have at least one hit in any of the outer three layers and that the average number of hits per jet track be more than 5.5 (the rejected events are mostly those from the process $e^+e^- \rightarrow e^+e^-(\gamma)$ which showered in the CD staircase).

CHAPTER 4

ANALYSIS

4.1 Monte Carlo Simulation of the Experiment

Monte Carlo techniques were used to calculate the tau-pair selection efficiency, some particle identification efficiencies, and particle misidentification and non-tau backgrounds levels. The simulation of the experiment consisted of four steps.

1. The reaction $e^+e^- \to \tau^+\tau^-$ was simulated with the lepton-pair generator written by Berends, Kleiss, and Jadach (BKJ),[45] based on their calculations of the process $e^+e^- \to \mu^+\mu^-$ to order α^3 but modified to exclude the lowest order weak terms.
2. The output of step (1) served as input to the tau decay simulation, based on a calculation of the spin dependent cross section for tau-pair production in e^+e^- annihilation.[13] The Monte Carlo event weights were renormalized to account properly for the fact that the production cross section had already been determined in step (1).
3. The output of step (2) (a list of particle momenta, identification codes, and vertex positions) served as input to a simulation of the detector. Electromagnetic showers were simulated by the EGS code of Ford and Nelson[46] and hadronic showers and minimum ionizing particle propagation were simulated by the High Energy Transport Code (HETC) of Armstrong.[47] These programs traced particles (primary and secondary) through a detailed description of the composition, geometry, and segmentation of the detector

(particles were traced until their energies were less than 5 MeV). The results of the HETC and EGS code were used to calculate positions and pulse heights of calorimeter and scintillator hits and positions of drift chamber hits for the OD and CD. This information was digitized, assigned hardware addresses, and saved in files with the same structure as the real data. After the detector response to an event was recorded, the hardware trigger efficiency was simulated. The detector simulation was quite slow; generation of 100 pb^{-1} of tau-pair events required about 12 CPU hours on the IBM 3081K.

4. From this point on, the Monte Carlo data (MCdata) and the real data were analysed with exactly the same software. The MCdata were filtered through PASS1, the tau-pair event selection, and the selection programs for the various experiments reported in this thesis. The input Monte Carlo momenta (output of step(2)) were available for each event during the analysis.

To study background processes, steps (1) and (2) above were replaced by analogous procedures for producing MCdata events. The event generators were based on calculations by Sjöstrand[48] for $e^+e^- \to q\overline{q}$, Smith and co-workers[49] for $e^+e^- \to e^+e^-e^+e^-$, $e^+e^- \to e^+e^-\mu^+\mu^-$, $e^+e^- \to e^+e^-q\overline{q}$, and $e^+e^- \to e^+e^-\tau^+\tau^-$ (the tau decay simulation was performed with the same program used for step (2) above). The BKJ lepton-pair generator was used for processes $e^+e^- \to e^+e^-$ and $e^+e^- \to \mu^+\mu^-$.

Following the method of Tsai[23] it is possible to derive the differential cross section for coherent tau-pair production and decay from the spin dependent differential cross section and the differential tau decay rate. The differential decay rates for the τ^+ and τ^- can be written

$$\frac{d\Gamma(\tau^\pm \to X^\pm)}{d^3p^\pm\, d\Omega} = A^\pm + B^\pm\, p_i^\pm w_i^\pm \qquad (4.1)$$

where $p^\pm$ are the decay product momenta and $w^\pm$ are the $\tau^\pm$ polarization vectors and $A^\pm$ and $B^\pm$ can be taken from the differential decay rates in section 1.5. The spin dependent production cross section (equation (1.7)) can be written

$$\frac{d\sigma(\vec{s_-}, \vec{s_+})}{d\Omega} = D + E_i^+ \, s_i^+ + E_j^- \, s_j^- + G_{ij} \, s_i^+ \, s_j^- . \tag{4.2}$$

The components of the τ^+ polarization vector w_i^+ can be found by the definition of polarization:

$$w_i^+ = \frac{E_i + G_{ij} \, s_j^-}{D + E_j^- s_j^-} . \tag{4.3}$$

The angular distribution of the τ^+ decay product is found by substituting this result in (4.1):

$$\frac{d\sigma(\vec{s_-}, \vec{s_+})}{d\Omega \, d^3p^+ \, d\Omega^+} \propto A^+ \left(D + E_j^- \, s_j^-\right) + B^+ \left(E_i^+ + G_{ij} \, s_j^-\right) p_i^+ . \tag{4.4}$$

Now the components of the τ^- polarization vector can be found:

$$w_j^- = \frac{A^+ \, E_j^- \; + B^+ \, G_{ij} \, p_i^+}{D \, A^+ + B^+ \, E_i^+ \, p_i^+} . \tag{4.5}$$

Substituting this result in (4.4) yields the simultaneous angular distributions of both decay products at a given production angle:

A^-B^+

$$\frac{d\sigma(\vec{s_-}, \vec{s_+})}{d\Omega \, d^3p^+ \, d\Omega^+ \, d^3p^- \, d\Omega^-} \propto A^+A^-D \; + \; A^+B^-E_j^-p_j^- \; + \; E_i^+p_i^+ \; + \; B^+B^-G_{ij} \, p_i^+ p_j^- . \tag{4.6}$$

This result, divided by the spin-averaged production weight D, was the event weight used in the tau decay Monte Carlo.

The branching ratios in the tau decay Monte Carlo were chosen to reflect what was known about the branching ratios from both theory and experiment at the time the MCdata files were created (mid-1984). Table 9 lists these branching ratios and their contributions to the inclusive branching ratios to one and three charged particles (e^+e^- pairs from Dalitz decays of π^o's were not included as "particles" although the pions from K_S^o decays were).

TABLE 9. Branching ratios used in tau decay Monte Carlo simulation. All known decay modes of the ρ'[14] were included in the Monte Carlo.

Decay mode	B.R.	1-prong B.R.	3-prong B.R.
$\tau \to \nu_\tau e \bar{\nu}_e$	0.183	0.183	...
$\tau \to \nu_\tau \mu \bar{\nu}_\mu$	0.178	0.178	...
$\tau \to \nu_\tau \pi$	0.111	0.110	...
$\tau \to \nu_\tau \rho$	0.234	0.234	...
$\tau \to \nu_\tau K$	0.005	0.005	...
$\tau \to \nu_\tau K^*$	0.012	0.009	0.003
$\tau \to \nu_\tau A_1$	0.200	0.100	0.100
$\tau \to \nu_\tau Q_1, Q_2$	0.007	0.003	0.004
$\tau \to \nu_\tau \rho'$	0.068	0.026	0.042
$\tau \to \nu_\tau (5\pi)$	0.002	...	0.0006

4.2 Particle Identification

4.2.1 Muons

A muon in the MAC detector was recognized by the presence of a track in the outer drift chambers which matched to a CD track, and energy deposition in the calorimeters consistent with that of a minimum ionizing particle. Due to continuous energy losses (dE/dx) only muons with momenta of at least 1.3 GeV/c penetrated the entire detector and produced a track in the OD. See Figure 20 for an example of an event containing two muons which were detected in the outer drift chambers.

A charged track was identified as a muon if:

- the χ^2 (two degrees of freedom) for a match of the CD and OD tracks was less than 75.0 for the normal OD tracking or it was less than 12.0 for the 2HIT tracking;
- the pulse height in the SC within a 45° cone about the CD track was less than 350 SHAM counts (1 GeV if electromagnetic energy conversion constants are used) times a geometrical factor which was introduced to force the efficiency of this cut to be independent of θ (see Figure 21);
- the pulse height in the HC within a 45° cone about the CD track was less than 1800 SHAM counts (about 6 GeV using hadronic energy conversion constants) times a geometrical factor which was introduced to force the efficiency of this cut to be independent of θ (see Figure 22);
- the CD momentum was greater than 2 GeV/c.

The effect of these cuts on the various decay channels, starting with the selected tau-pair data sample, is outlined in Table 10.

Since it was possible to obtain a pure and unbiased sample of events

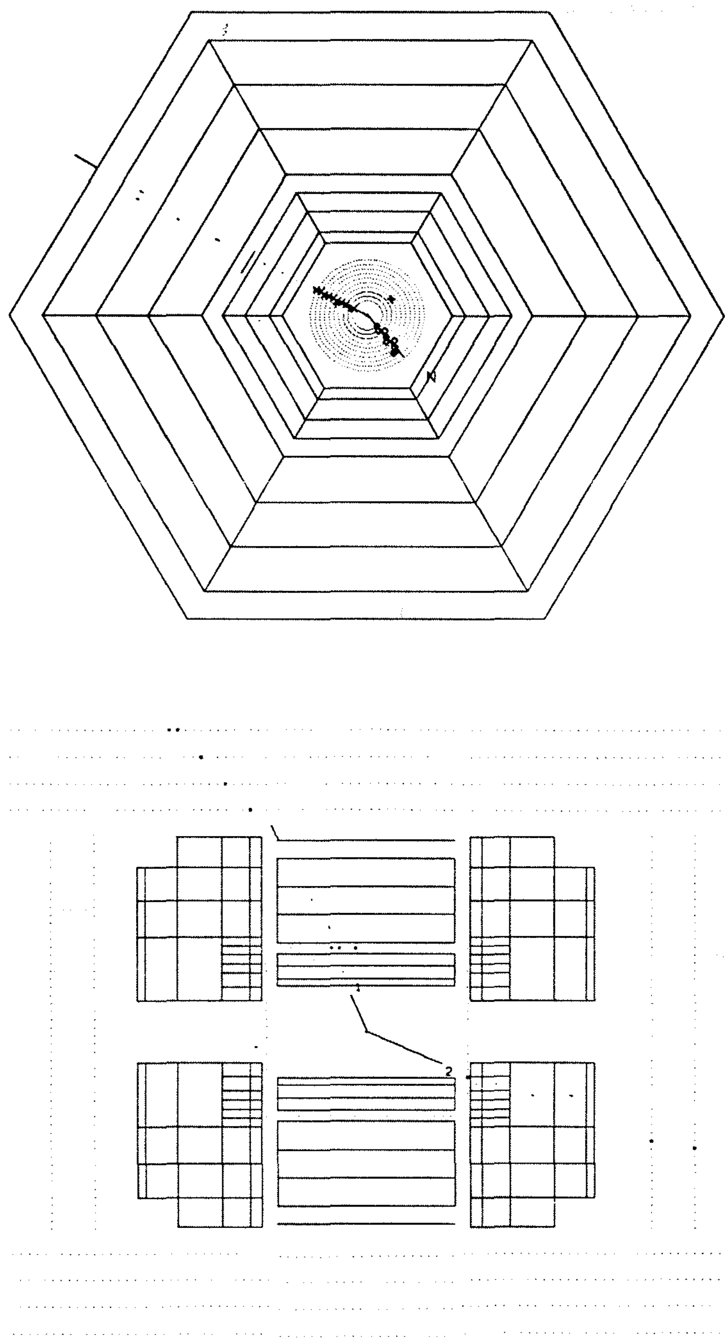

FIGURE 20. Offline display of an event containing two muons. The upper view shows the central section viewed from along the beams and the lower is a side view of the two sextants containing the most energy.

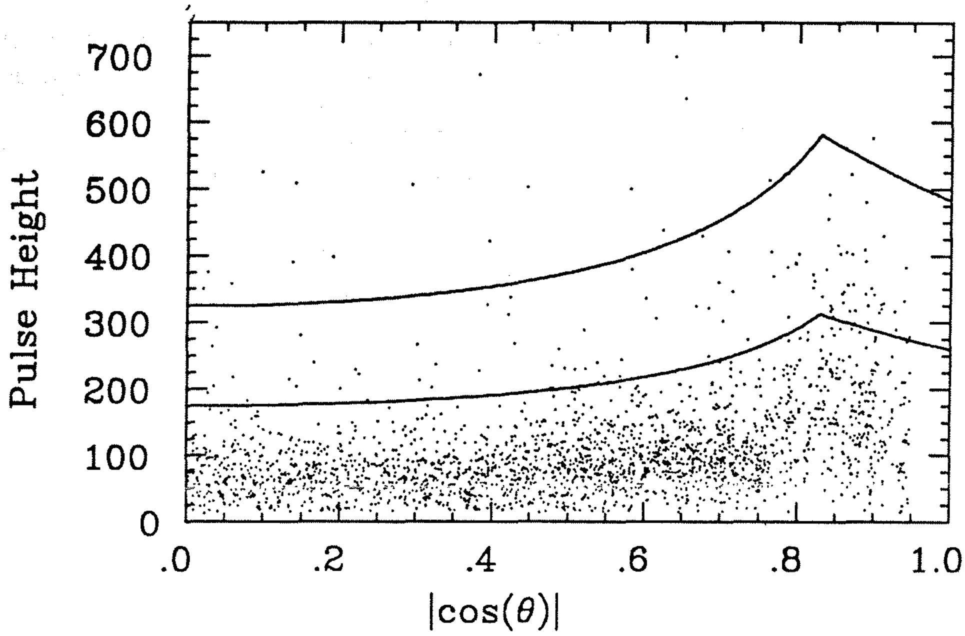

FIGURE 21. Plot of SC pulse height versus $|\cos\theta|$ for muons in $e^+e^- \rightarrow \mu^+\mu^-$ events. The upper curve is the maximum allowed pulse height of the muon identification. The lower curve is a tighter requirement used to check uncertainties in the muon identification and background rejection in Chapter 4.

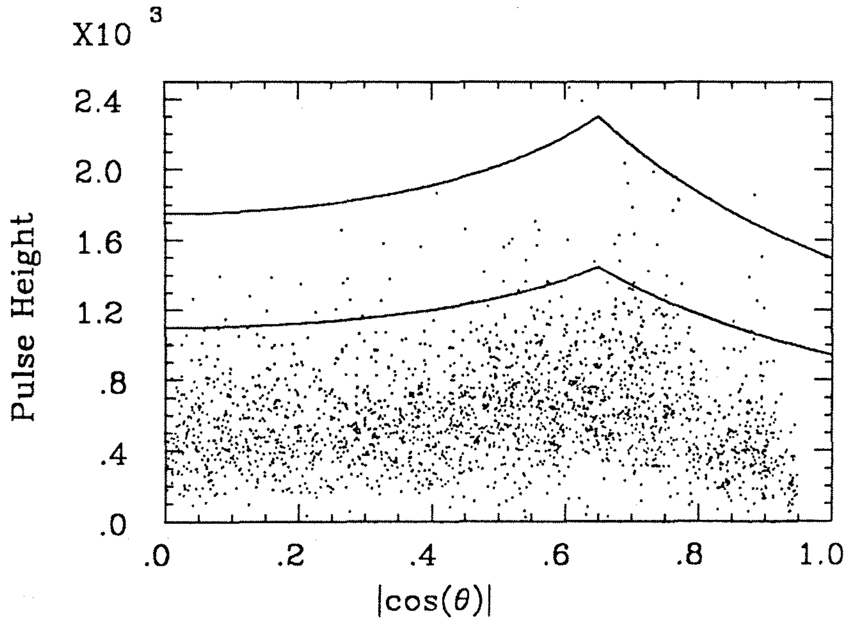

FIGURE 22. Plot of HC pulse height versus $|\cos\theta|$ for muons in $e^+e^- \rightarrow \mu^+\mu^-$ events. The upper curve is the maximum allowed pulse height of the muon identification. The lower curve is a tighter requirement used to check uncertainties in the muon identification and background rejection in Chapter 4.

TABLE 10. Effect of muon identification cuts on a tau Monte Carlo data sample. The first row shows the number of tau decays after the tau-pair event selection and the preliminary particle identification requirements such as the minimum allowable momentum cut ($p_\mu > 2$ GeV/c) and the requirement $|\cos\theta_\mu| < 0.9$ have been applied. The following rows demonstrate what happens as the cuts are applied successively.

Cut	$\tau \to \nu_\tau e \bar{\nu}_e$	$\tau \to \nu_\tau \mu \bar{\nu}_\mu$	$\tau \to \nu_\tau \pi(K)$	$\tau \to \nu_\tau \rho$	$\tau \to \nu_\tau \pi + n\pi^0$
	2640	3268	3065	4642	3948
CD-OD match	0	2784	111	93	80
SC pulse height	0	2775	102	25	16
HC pulse height	0	2774	65	18	8
No neutrals	0	2733	65	13	8

with muons at various angles and momenta, the efficiency of identifying a charged track as a muon was measured and used directly (it was not necessary to rely on Monte Carlo calculations) in the branching ratio measurements made later in this chapter. A sample of events produced by $e^+e^- \to e^+e^-\mu^+\mu^-$ was selected with the following requirements:

- there were two charged tracks in the CD with a satisfactory vertex-fit χ^2;
- the acollinearity angle between the two charged tracks was $> 20°$;
- both tracks satisfied loose muon identification cuts and one of the tracks matched with an OD track with a satisfactory χ^2.

The loose muon identification cuts required either that a CD track match with calorimeter tracks with a total energy consistent with a minimum ionizing particle and some energy in the outer layer of the HC or that the CD track match with a track in the OD.

For each event in this sample it was determined which track passed the tight calibration cuts and then the other track was examined to determine whether it would pass cuts on the CD-OD match since it was not forced to meet this requirement in order for the event to appear in the sample. The efficiencies of the energy cuts were measured with all tracks having CD-OD matches. Figure 23 shows the CD-OD matching efficiency as a function of momentum for $|\cos\theta| < 0.9$ and Figure 24 shows the efficiency of the muon identification as a function of $|\cos\theta|$ for CD momenta greater than 2 GeV/c. The last muon identification requirement above was introduced because the efficiency levels off by about 2 GeV/c independent of θ; this made the efficiency correction straightforward.

Since muon misidentification by penetration of the calorimeters by hadronic showers ("punchthrough") is difficult to model accurately, the muon misidentification probability was measured with the data. The result of this measurement, described in appendix A, was that the data and Monte Carlo agreed well.

4.2.2 Electrons

The signature for an electron in the MAC detector was a charged track in the central drift chamber which matched to a single shower in the electromagnetic sections of the calorimeters. See Figure 25 for an example of an event with two electrons, one in the central section and the other in the endcap calorimeter.

The requirements for a track to be identified as an electron were motivated by the strengths of the MAC detector and the properties of the expected backgrounds. These identification requirements were:

- no match between the CD track and an OD track;
- no energy in the outer layer of the hadron calorimeter;
- track energy 90% contained in the electromagnetic calorimeters;

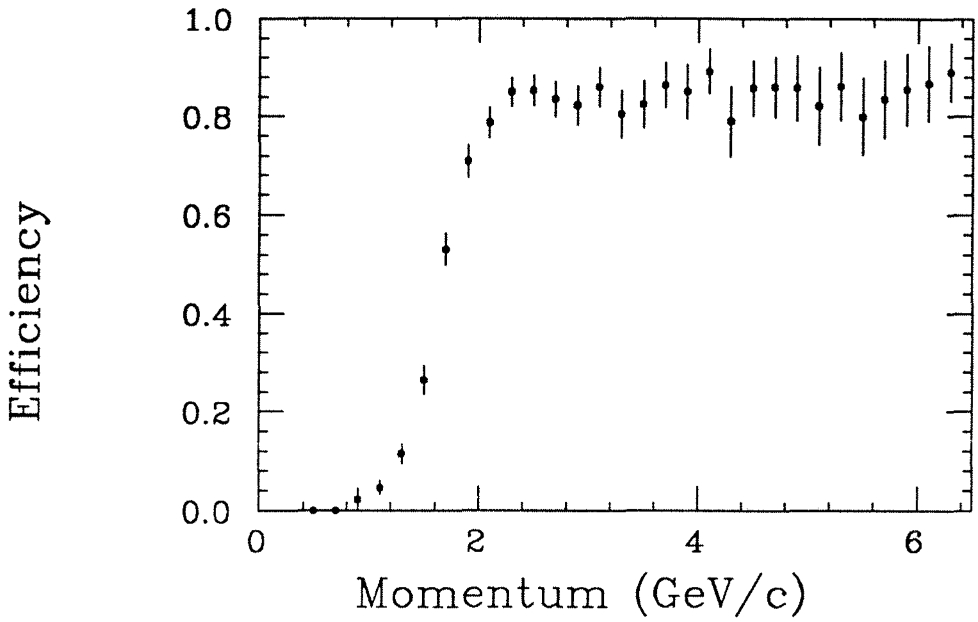

FIGURE 23. The CD-OD matching efficiency for muons as a function of momentum (measured with events from the process $e^+e^- \rightarrow e^+e^-\mu^+\mu^-$).

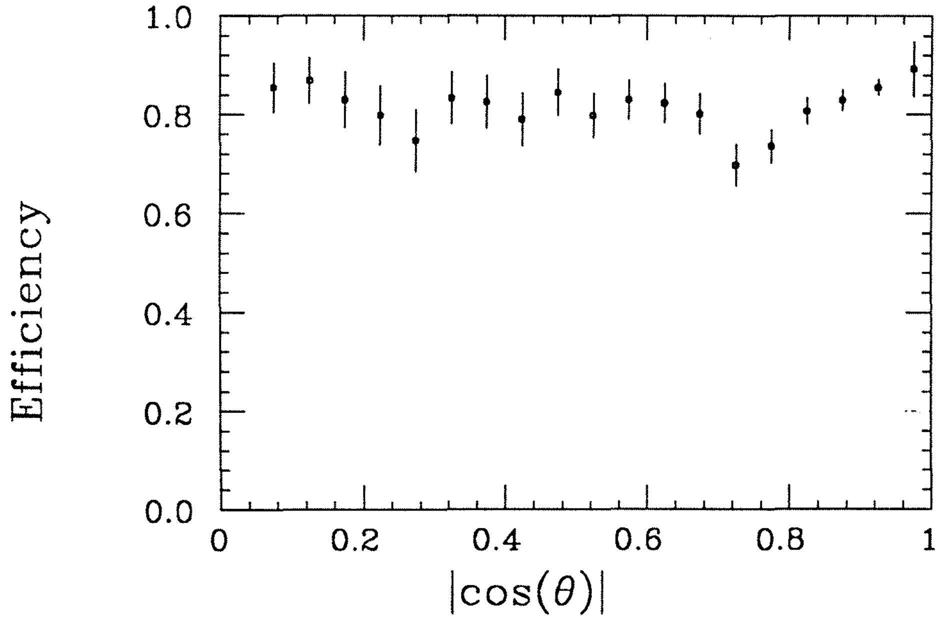

FIGURE 24. The muon identification efficiency as a function of $|\cos\theta|$ for muon momenta greater than 2 GeV/c (measured with events from the process $e^+e^- \rightarrow e^+e^-\mu^+\mu^-$).

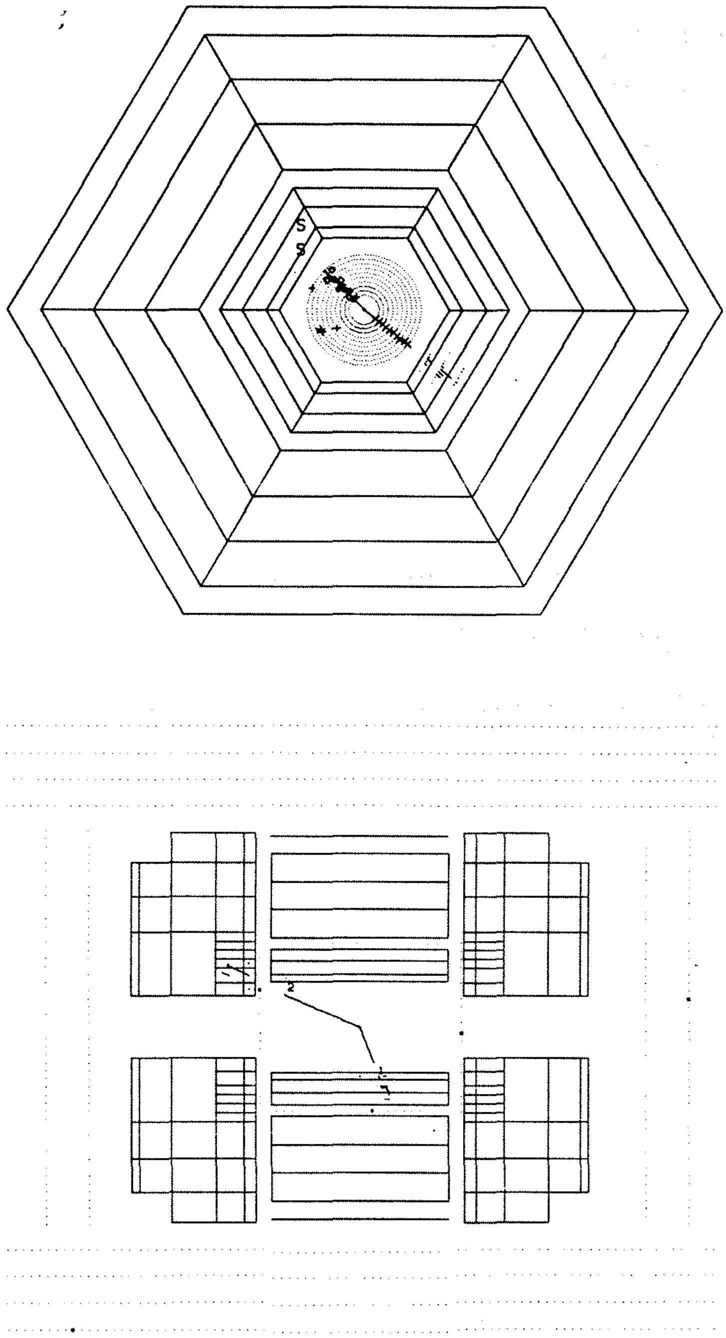

FIGURE 25. Offline display of an event containing two electrons. The upper view shows the central section viewed from along the beams and the lower is a side view of the two sextants containing the most energy.

- track hadronic energy < 10% of track momentum;
- rms azimuthal width of associated shower < 4°;
- azimuthal angle between CD track and associated shower < 2°;
- no neutral shower within 65° of CD track with an energy greater than 500 MeV;
- CD momentum > 1 GeV/c.

The effect of these cuts on the various decay channels, starting with the selected tau-pair data sample, is outlined in Table 11.

TABLE 11. Effect of electron identification cuts on a tau Monte Carlo data sample. The first row shows the number of tau decays after the tau-pair event selection and the preliminary particle identification requirements such as the minimum allowable momentum cut ($p_e > 1$ GeV/c) and the requirement $|\cos\theta_e| < 0.75$ have been applied. The following rows demonstrate what happens as the cuts are applied successively.

Cut	$\tau \to \nu_\tau e \bar{\nu}_e$	$\tau \to \nu_\tau \mu \bar{\nu}_\mu$	$\tau \to \nu_\tau \pi(K)$	$\tau \to \nu_\tau \rho$	$\tau \to \nu_\tau \pi + n\pi^0$
	3073	3693	3305	5867	2866
No CD-OD match	3073	802	3188	5770	2806
Non-penetrating	2946	1	460	1381	674
$\delta\phi$(CD-SC), σ_ϕ(SC)	2930	1	220	238	73
No neutrals	2879	1	211	142	45

Almost 100% of muons were rejected by requiring that there be no OD track matched to the CD track and that there be no energy in the outer layer of the hadron calorimeter. Charged hadrons were rejected by the requirement that the total energy of the hits in the calorimeters within a 45° cone about the CD track be more than 90% contained in the electromagnetic calorimeters and that the total energy in the hadron calorimeters inside this cone be less than 10% of the central drift track momentum. Since the electromagnetic calorimeters consist of 0.5-1.4 nuclear absorption lengths of material, a pion will begin a hadronic shower before it enters the hadron calorimeter about 60% of the time. The cuts on the matching between the CD track and the electromagnetic shower and the width of the shower reduced the background from pions because hadronic showers tend to be wider and more asymmetric than electromagnetic showers and the background from rhos was reduced because π^0's from rho decays tended to produce showers that are wider than those produced by a single electromagnetic particle and the π° showers also tended not to coincide with the charged pion CD track. The angular resolution of the endcap electromagnetic calorimeters was not sufficient to identify electrons adequately.

Because the cross sections for processes with several electrons in the final state are so large it was possible to obtain a sample of events with a small number of electrons and no other particles in the detector to study in detail the properties of electromagnetic showers in the MAC detector without relying on Monte Carlo calculations. The cross section for $e^+e^- \rightarrow e^+e^-$ is so large and the signal so distinctive that it was trivial to obtain a sample of electrons with momenta of 14.5 GeV/c^2. This part of the electron calibration sample was formed with the following cuts:

- two charged tracks with acollinearity $< 5°$;
- total energy in the calorimeters $>E_{beam}$;
- two electromagnetic showers with acollinearity $< 20°$.

A sample of events with a softer momentum spectrum (which was more appropriate for tau decays) was obtained with requirements that selected events produced by $e^+e^- \rightarrow e^+e^-e^+e^-$:

- two charged tracks in the CD with acollinearity $> 20°$;
- total energy in the calorimeters < 25 GeV;
- no identified muons in the detector;

- at least one identified electron.

Figure 26 shows the measured efficiency of the electron identification requirements for $|\cos\theta| < 0.75$ as a function of momentum and Figure 27 shows the efficiency, measured with tracks with energies between 2 and 10 GeV, as a function of $|\cos\theta|$. The efficiency measured with events from the process $e^+e^- \rightarrow e^+e^-$ was found to be consistent with the efficiency measured with the softer spectrum extrapolated to beam energy. These efficiencies were used directly in the branching ratio measurements described later in this chapter.

4.2.3 Rhos

A charged rho was recognized in the detector by the presence of a charged track in the central drift chamber and a "neutral" electromagnetic shower (one that did not match with the CD track). In the crowded environment of multihadron events where the average charged multiplicity is 13 and the average total multiplicity is 20 it is not possible to identify rhos with this signature but in tau-pair production there is one tau in each hemisphere of the detector and charged and neutral tracks can be unambiguously associated in each event. An unusually wide electron or pion (kaon) shower could occasionally imitate a separated shower but these backgrounds were greatly reduced with a simple minimum energy requirement on the neutral shower. There were backgrounds from $K^*, Q_{1,2}$, and ρ' decays (one charged hadron and one or more neutrals) but the sum of these branching ratios is only about 7% so they did not pose a serious problem. Background from radiative events was reduced to near negligible levels by requiring that the neutral shower be within 50° of the charged track. The most significant background for the ρ signal was due to the decay $A_1 \rightarrow \pi\pi^\circ\pi^\circ$. This background was reduced by requiring that there be only one separated neutral

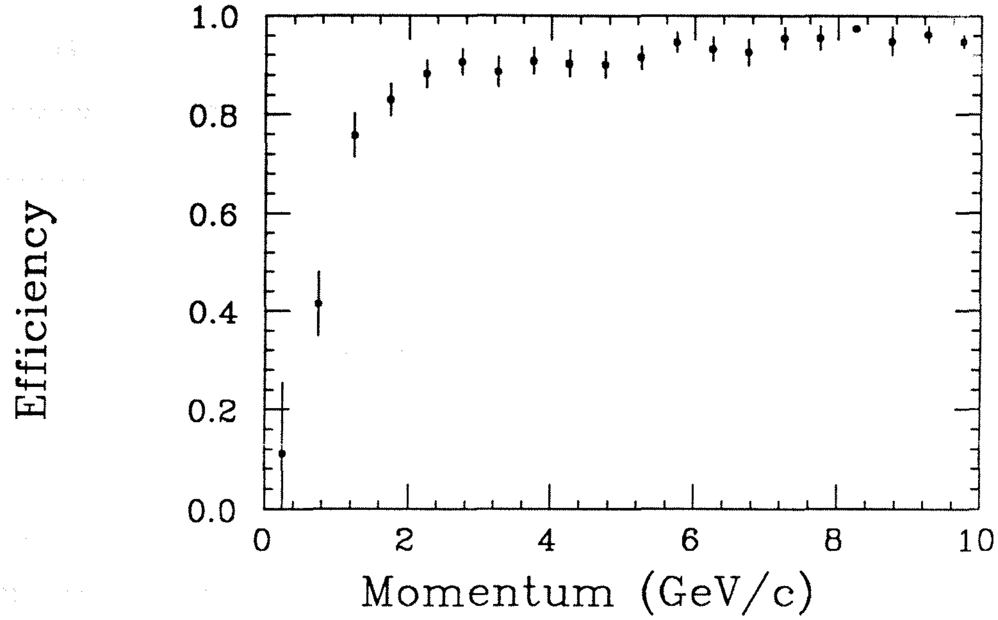

FIGURE 26. Electron identification efficiency as a function of momentum (measured with events from the process $e^+e^- \to e^+e^-e^+e^-$).

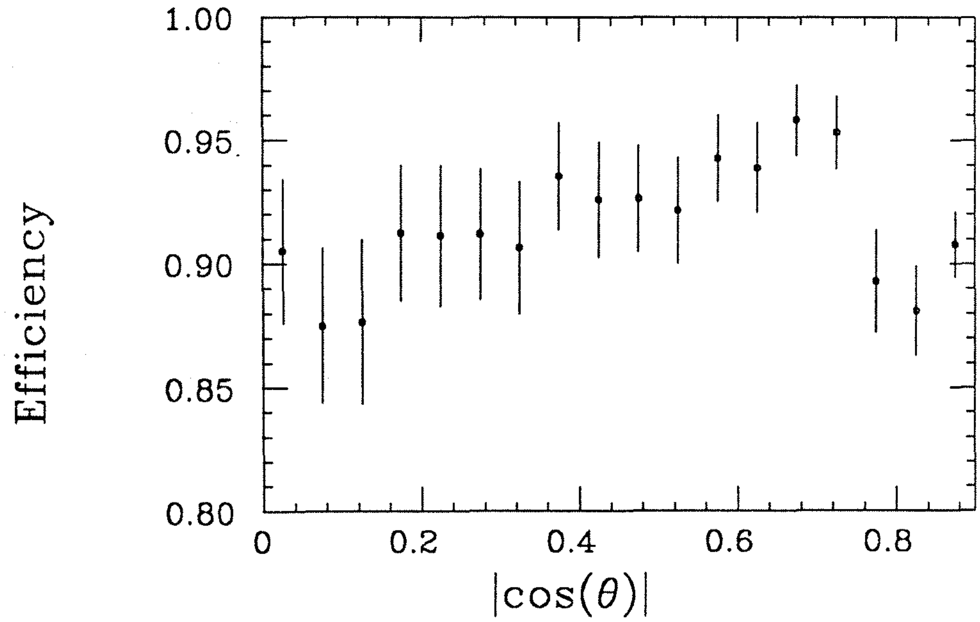

FIGURE 27. Electron identification efficiency as a function of $|\cos\theta|$ (measured with events from the process $e^+e^- \to e^+e^-e^+e^-$).

shower. Unfortunately more than half of the single charged prong decays of the A_1 have only one detectable shower. For the purpose of counting neutrals, showers were required to have at least two layers with energy depostion greater than 50 MeV. After the events with zero or two or more neutrals were rejected, the remaining shower was required to have two layers with energy deposition greater than 100 MeV and total energy greater then 500 MeV to reduce background from detector noise and false showers created from wide hadronic showers. The background from A_1 decays was reduced further by requiring the shower which matched to the CD track to have an energy deposition in the first layer of the SC which was consistent with the expectation of a minimum ionizing particle. Rejection of tracks with a CD-OD match achieved a small reduction in the residual $\tau \rightarrow \nu_\tau \mu \bar{\nu}_\mu$ background. The detector Monte Carlo provided the only estimate of the rho identification efficiency. Figures 28 and 29 show the rho identification efficiency as a function of momentum for $|\cos\theta| < 0.9$ and as a function of $|\cos\theta|$ for all momenta. The effect of these cuts on the various decay channels, starting with the selected tau-pair data sample, is outlined in Table 12.

TABLE 12. Effect of rho identification cuts on a tau Monte Carlo data sample. The first row shows the number of tau decays after the tau-pair event selection and the preliminary particle identification requirements such as the requirement $|\cos\theta_\rho| < 0.90$ has been applied. The following rows demonstrate what happens as the cuts are applied successively.

Cut	$\tau \rightarrow \nu_\tau e \bar{\nu}_e$	$\tau \rightarrow \nu_\tau \mu \bar{\nu}_\mu$	$\tau \rightarrow \nu_\tau \pi(K)$	$\tau \rightarrow \nu_\tau \rho$	$\tau \rightarrow \nu_\tau \pi + n\pi^\circ$
	1779	2354	1915	3420	1640
no CD-OD match	1779	547	1813	3321	1597
1 neutral	20	6	86	2138	682
Min. Ion.	1	6	64	1771	493

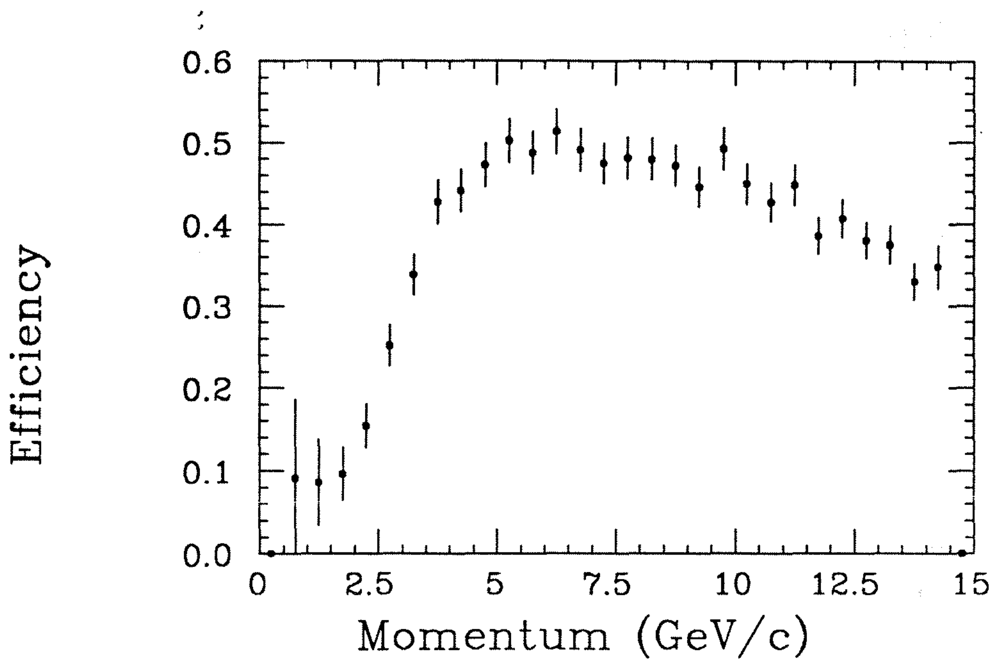

FIGURE 28. Rho identification efficiency as a function of momentum (measured with a Monte Carlo calculation).

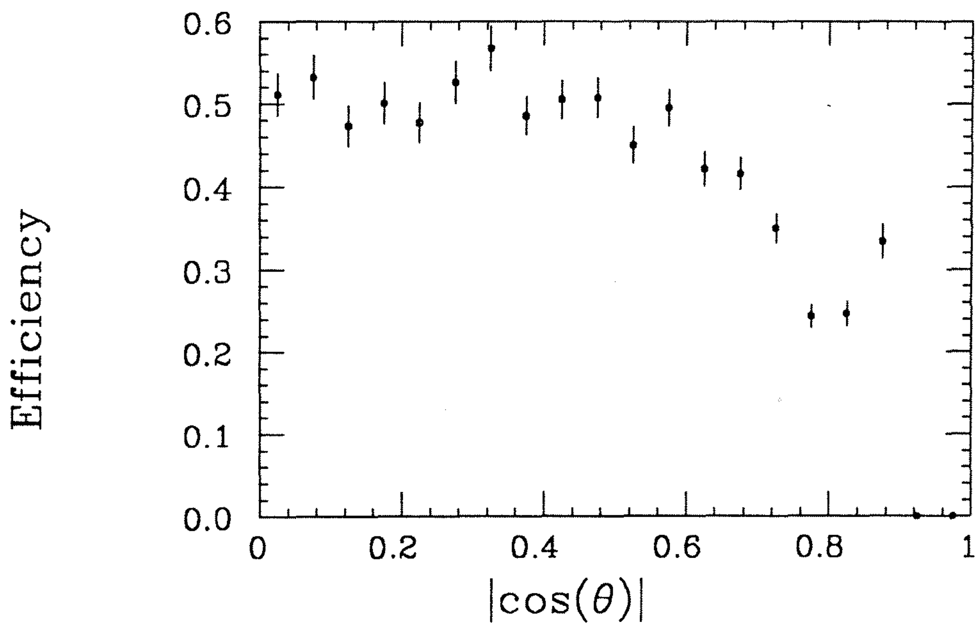

FIGURE 29. Rho identification efficiency as a function of $|\cos\theta|$ (measured with a Monte Carlo calculation).

4.2.4 Pions

In all discussions of charged pions it should be understood that kaons are to be included since the MAC detector had no π/K separation capabilities. In studies of tau decays this is not a serious problem since the branching ratio B_K has been measured and found to be only $\sim$ 6% of B_π. The ideal signature for a pion in the MAC detector was a shower in the hadron calorimeter with energy consistent with the CD track momentum. Because the branching ratio B_π is small compared with B_μ and $B_{\pi+N\pi^0}$ the pion identification requirements were fairly tight and inefficient.

The pion identification requirements were the following:

- no match between the CD track and an OD track;
- the CD track extrapolated to the active area of the OD;
- more than 25% of the track calorimeter energy was in the hadron calorimeter;
- there was a single shower in the vicinity of the CD track with a total energy in the first layer of the CSC or the ESC that did not exceed the expectation for a minimum ionizing particle;
- the CD momentum was greater than 2 GeV/c.

The effect of these cuts on the various decay channels, starting with the selected tau-pair data sample, is outlined in Table 13.

The detector Monte Carlo provided the only estimate of the pion identification efficiency since there was no background free source of pions in the data with which to measure the efficiency. Figures 30 and 31 show the pion identification efficiency as a function of momentum for $|\cos\theta| < 0.9$ and as a function of $|\cos\theta|$ for all momenta.

TABLE 13. Effect of pion identification cuts on a tau Monte Carlo data sample. The first row shows the number of tau decays after the tau-pair event selection and the preliminary particle identification requirements such as the minimum allowable momentum cut ($p_\pi > 2$ GeV/c) and the requirement that the CD track extrapolate to active areas of the OD and the calorimeters. The following rows demonstrate what happens as the cuts are applied successively.

Cut	$\tau \to \nu_\tau e \bar{\nu}_e$	$\tau \to \nu_\tau \mu \bar{\nu}_\mu$	$\tau \to \nu_\tau \pi(K)$	$\tau \to \nu_\tau \rho$	$\tau \to \nu_\tau \pi + n\pi^0$
	2515	3208	3090	4722	2133
No CD-OD match	2515	22	2635	4473	2048
$E_{HC}/E > 0.25$	7	21	2003	2168	669
Min. Ion.	1	20	1555	563	104
No neutrals	1	14	1346	132	19

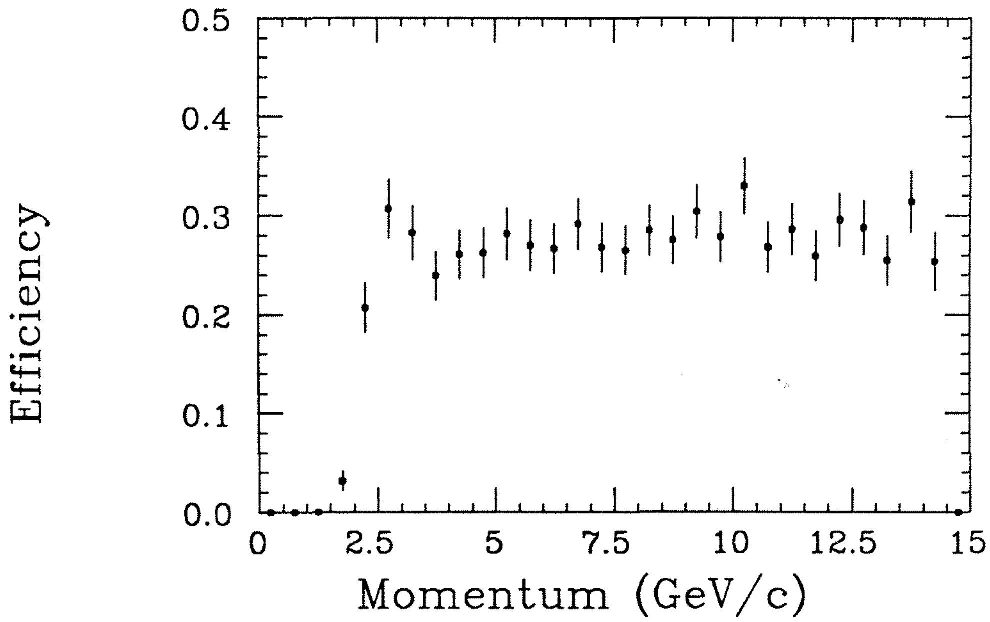

FIGURE 30. Pion identification efficiency as a function of momentum (measured with a Monte Carlo calculation).

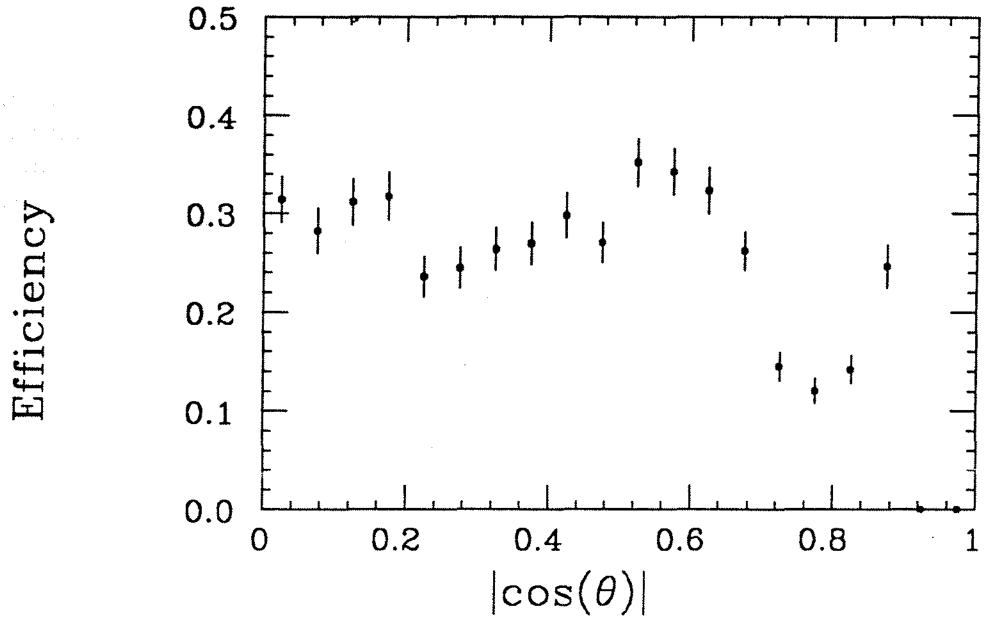

FIGURE 31. Pion identification efficiency as a function of $|\cos\theta|$ (measured with a Monte Carlo calculation).

4.3 Single Muon Trigger Efficiency

The single muon (SMU) trigger efficiency, for muons with energies greater than 2 GeV which were not near the calorimeter cracks, was 100% in the detector simulation but somewhat less than this in reality. The two-photon muon pair events described in section 3.1.1 were used to measure the true efficiency. Only a single SMU trigger was required for an event to be logged but all the information used by the trigger electronics was saved in the data and could be used to reconstruct how many SMU triggers were satisfied and in what regions of the detector they occurred. Although the segmentation of the trigger was fairly coarse (the solid angle was divided into 44 pieces) it was straightforward to require the CD tracks to be far enough apart that no confusion was possible.

Two successes were recorded for events in which both CD tracks satisfied the SMU trigger and one failure was recorded for events in which only one CD track fired the trigger. The efficiency was measured as a function of polar angle and averaged over time. Figure 32 shows the measured single muon trigger efficiency as a function of the polar angle. The efficiency appears to be uniform out to $|\cos\theta| \sim 0.75$ (near the edge of the central section TOF counters) and then drops with increasing $|\cos\theta|$. To simplify the trigger efficiency correction, an average efficiency was formed. The first 14 bins of Figure 32 were fitted with a line of zero slope and the last four bins were fitted with a separate straight line. The lowest order angular distribution for tau-pair events of

$$\frac{dn}{d\cos\theta} \propto (1+\cos^2\theta), \tag{4.7}$$

was used to form the weighted average of the fitted efficiency of 0.938 ± 0.002.

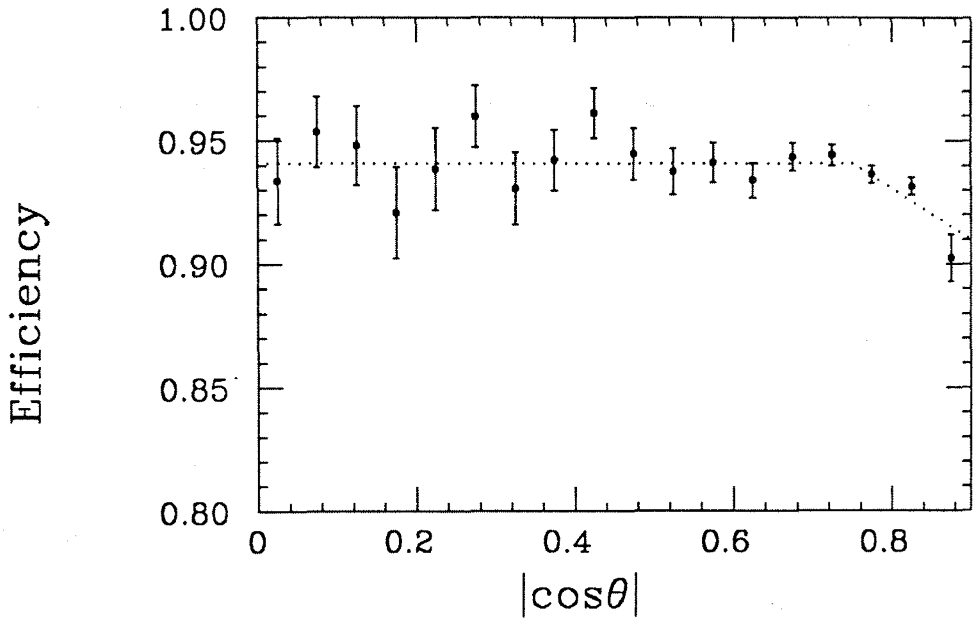

FIGURE 32. Single muon trigger efficiency versus $|\cos\theta|$. The points are measurements using a sample of two-photon produced muon pairs. The Monte Carlo efficiency was 100%. The dotted line is a fit to the efficiency (described in the text).

4.4 Measurements of the Leptonic Branching Ratios

4.4.1 Branching Ratios from 1-3 Event Sample

Leptonic branching ratios were extracted from the 1-3 event sample by measurement of the fraction of events in which the 1-prong was an identified lepton, that is,

$$B_l = B_1\,(N_{l-3}/\epsilon_{l-3})/(N_{1-3}/\epsilon_{1-3})$$

where N_{1-3} and N_{l-3} are background subtracted numbers of observed 1-3 and l-3 events, ϵ_{1-3} and ϵ_{l-3} are efficiencies for detecting these types of events, and B_1 is the 1-prong branching ratio. This method has several advantages over the one in which the branching ratio is calculated from the integrated luminosity, the number of observed l-3 events, and the l-3 detection efficiency. The integrated luminosity and total cross section do not enter directly in the above method and many other systematic uncertainties tend to cancel, including those in the 1-3 selection efficiency and the background due to unidentified photon conversion pairs.

Table 14 shows the numbers relevant to the calculations of B_e and B_μ. The branching ratios were extracted with an iterative procedure in which the backgrounds which were dependent on the branching ratios were adjusted. Since the results were fairly close to the values used in the Monte Carlo the effects of iterating were negligible. The l-3 detection efficiencies in Table 14 are the products of the event selection efficiencies measured with the Monte Carlo and the measured lepton identification efficiencies.

The systematic errors in the branching ratios were estimated by variation of the requirements used to define the various event samples. The systematic errors associated with the uncertainty in the photon-conversion pair background to the 1-3 sample were estimated by variation of the required

TABLE 14. Numbers from l-3 analysis used to calculate leptonic branching ratios. Numbers of observed events and significant predicted backgrounds for the 1-3 and l-3 samples and the product of geometrical acceptance and efficiency for each sample (errors are statistical only).

	Data samples			
	1-3	e-3	1-3	μ-3
	($\lvert\cos\theta\rvert < 0.7$)		($\lvert\cos\theta\rvert < 0.9$)	
No. of observed events	2452±50	390±20	3339±58	473±22
Efficiency (%)	35.4±0.3	25.4±0.5	47.4±0.3	30.9±0.5
Backgrounds:				
Misidentification	...	45±3	...	11±2
Pair conversion	99±5	9±2	133±5	28±2
$ee\tau\tau$	36±5	5±2	52±5	13±3
$eeq\bar{q}+q\bar{q}$	92±10	1±1	126±13	4±3

number of vertex-fit tracks in the 3-prong. Neither of the branching ratios changed by more than 0.002 when the required number of vertex-fit tracks was varied from its nominal value of two to one or three. A systematic error of 0.001 was assigned on the basis of these results. Since B_l is directly dependent on B_1, the experimental error in B_1 of 0.003 (see Section 1.6.1) leads to a systematic error in B_l of 0.001. The systematic errors due to uncertainties in the lepton identification were estimated by measuring the branching ratios for several sets of identification requirements which were all more restrictive than those used for the final result. Variation of these cuts also resulted in changes in the signal to background ratios and so uncertainties in the background rejection inefficiencies were accounted for by these variations. Table 15 lists the requirements that were varied and the effects on the branching ratios.

Systematic errors of 2.7% and 3.3% were assigned to B_μ and B_e respectively for these uncertainties. One final check of systematic uncertainty was made by calculating the branching ratios with the alternate method involving the integrated luminosity as mentioned above. Those results are also listed in Table 15 and are completely consistent with the final results. After adding all the systematic errors in quadrature the final l-3 branching ratio results are

$$B_e = 0.180 \pm 0.009 \pm 0.006,$$

$$B_\mu = 0.183 \pm 0.009 \pm 0.005,$$

where the first errors are statistical and the second are systematic.

4.4.2 Selection of Tau-pair $e\mu$ Events

The selection of events produced in the reaction

$$\begin{array}{l} e^+e^- \longrightarrow \tau^+\tau^- \\ \qquad\qquad \hookrightarrow \nu_\tau \mu^- \bar{\nu}_\mu \\ \qquad\quad \hookrightarrow \bar{\nu}_\tau e^+ \nu_e \end{array}$$

and the charge conjugate final state was performed from the raw data rather than the tau-pair sample, primarily because the minimum allowed energy cut of 6 GeV (see section 4.3) removed more events than was necessary to reduce backgrounds.

These events were required to have two vertex-fit charged tracks, one of which was identified as a muon and the other as an electron. In order to reduce backgrounds from the processes $e^+e^- \rightarrow e^+e^-(\gamma)$, $e^+e^- \rightarrow e^+e^-e^+e^-$, or $e^+e^- \rightarrow e^+e^-\mu^+\mu^-$ in events with a poorly measured θ it was required that each CD track have at least one hit in the outer three layers of the CD: Since these processes peak strongly at low angle this was an effective cut. Events that deposited large amounts of energy in both the north and south endcap scintillators were rejected to reduce background from any process with

TABLE 15. Changes in leptonic branching ratios due to variation of the requirements for lepton identification. The requirements and the variations thereof are discussed in detail in the text. These results were used to estimate the systematic uncertainties in lepton identification and background rejection.

Requirement changed	Correction to efficiency	B_e	B_μ
SC pulse height	0.98	...	0.184±0.009
HC pulse height	0.98	...	0.186±0.009
2 hit OD tracking	0.89	...	0.187±0.009
CD-OD χ^2	0.82	...	0.192±0.009
Minimum CD momentum	0.89	...	0.181±0.009
σ_ϕ, δ_ϕ	0.98	0.177±0.009	...
$\sigma_\theta, \delta_\theta$	0.95	0.179±0.009	...
Minimum energy	0.98	0.181±0.009	...
Minimum CD momentum	0.85	0.181±0.010	...
E_{had}/E_{tot}	0.90	0.186±0.010	...
$\int \mathcal{L}\,dt$ method	...	0.177±0.010	0.184±0.009

two high energy electrons at low angles. Based on Monte Carlo estimates it was suspected that the largest remaining background at this point was from the process $e^+e^- \to e^+e^-\mu^+\mu^-$. It was possible to use the sample itself to estimate the size of this background by exploiting the nearly 100% charge asymmetry of these events and the fact that in half of these events the total charge is ±2 rather than 0 as it is for tau-pair events. The fraction of events from this background process, $f_{ee\mu\mu}$, was estimated from

$$f_{ee\mu\mu} = 2\frac{N_f - N_b}{N},$$

where N_f (N_b) was the number of events in the sample with total charge ± 2 and $\cos\theta > 0$ ($\cos\theta < 0$) and N was the total number of events in the sample. The charge assignment was based on the electron charge. Subtracting the events in the backward hemisphere accounted for the small fraction of tau-pair events with charge misidentification of one of the tracks. The factor of two accounted for the half of the background events with total charge 0. The result of this measurement was $f_{ee\mu\mu} \sim 3\%$. In order to reduce this background the acollinearity angle was required to be less than 40° and the acoplanarity angle was required to be greater than 1°: This reduced the background from the process $e^+e^- \to e^+e^-\mu^+\mu^-$ to 1.5%, consistent with a Monte Carlo estimate of 1.2%.

Displays (similar to those shown in Figures 20 and 25) of the events that failed the 1° acoplanarity cut were scanned to look for possible backgrounds from the processes $e^+e^- \to e^+e^-(\gamma)$ and $e^+e^- \to \mu^+\mu^-(\gamma)$ since they have acoplanarity distributions which are highly peaked at 0 but none were found. There were, however, several events that may have been cosmic rays so the following additional cuts, similar to those in section 4.4, were introduced to reduce this background:

- the reconstructed event vertex was required to be consistent with the known beam centroid and size, i.e., $|z_0| < 5.0$ cm. and $r_0 < 0.5$ cm.
- events with two scintillator hits were required to hav. TOF information consistent with that of two particles produced at the origin during the time interval in which e^+e^- annihilations occurred, i.e., $|t_{avg}| < 12$ nsec and $t_{dif} < 8.0$ nsec.

Less than 1% of the sample was removed by these requirements and it was observed that none of the removed events were cosmic rays.

It was concluded that the above cuts reduced the backgrounds from the processes $e^+e^- \to e^+e^-(\gamma)$, $e^+e^- \to \mu^+\mu^-(\gamma)$, $e^+e^- \to e^+e^-e^+e^-$, and cosmic rays to negligible levels and that the background from the process $e^+e^- \to e^+e^-\mu^+\mu^-$ was 1.3%. The largest remaining background, apart from particle misidentification, was from tau-pair events produced in two-photon collisions.

4.4.3 Branching Ratios from $e\mu$ Event Sample

The observed number of $e\mu$ events is given by

$$N_{e\mu} = 2\, B_e\, B_\mu\, \epsilon_{e\mu} \mathcal{L}_T\, \sigma_{\tau\tau} + N_{BG}, \tag{4.8}$$

where $\mathcal{L}_T$ is the integrated luminosity, $\sigma_{\tau\tau}$ is the total cross section for the process $e^+e^- \to \tau^+\tau^-$, B_e and B_μ are the electronic and muonic branching ratios of the tau, $\epsilon_{e\mu}$ is the efficiency for detecting these events, and N_{BG} is the number of background events. Table 16 lists the numbers relevant to the calculation of $B_e\, B_\mu$. The dominant misidentification background was overlapping pions and showers from the decay mode $\tau \to \nu_\tau \rho$ which were classified as electrons. The efficiency is the product of the general selection efficiency from the Monte Carlo and the measured trigger and e, μ identification efficiencies. The backgrounds were adjusted to reflect the measured efficiencies. Since the background estimate depended slightly on B_e, B_μ, an iterative method was used to solve equation (4.8).

The SMU trigger efficiency was assumed in the Monte Carlo to be 100% for the muon identification requirements used to select this sample but the measured value was only $93.8 \pm 0.2\%$. Since these events also satisfied other triggers, the total measured trigger efficiency was somewhat higher. For data accumulated before 1983 (60% of the data) the ENERGY trigger was the next most efficient trigger and for the later data the SEL trigger was highly efficient. There were no events in the data sample with unique BBSC

TABLE 16. Numbers from $e\mu$ analysis used in calculation of $B_e B_\mu$. Numbers of observed events, significant predicted backgrounds, and the product of geometrical acceptance and efficiency (errors are statistical only).

No. of observed events	363 ± 19
Efficiency (%)	18.8 ± 0.4
Backgrounds:	
Misidentification	38 ± 3
$ee\tau\tau$	17 ± 4
$ee\mu\mu$	5 ± 3

or MULT triggers. The ENERGY (SEL) trigger efficiency was estimated by measurement of the fraction of events with an SMU trigger which also had an ENERGY (SEL) trigger. With this procedure it was determined that the ENERGY trigger was 23±3% efficient for this type of event and the SEL trigger was 78±4% efficient. Therefore, the total trigger efficiency was 95.3±0.4% in the earlier data and 98.5±0.3% in the later. The luminosity-weighted average of these two samples was 96.6±0.4%. A conservative systematic error of 2% was assigned to the total trigger efficiency since it was not possible to measure independently the ENERGY trigger efficiency for this type of event and to account for the different angular and momentum distributions of the muons in this process and the two-photon process used to measure the SMU trigger efficiency.

The integrated luminosity was measured with the processes $e^+e^- \rightarrow e^+e^-$ and $e^+e^- \rightarrow \gamma\gamma$ and was found to be 212.7 ± 3.3 pb^{-1} where the error quoted is predominantly systematic. The systematics were examined in great detail for a fraction of the data[50,51] and assumed to be no more than a factor of two larger for the data (comprising about 78 pb^{-1}) which was not monitored so carefully. The uncertainty in the integrated luminosity therefore contributed 1.6% to the systematic error in $B_e\, B_\mu$.

Variation of the lepton identification cuts showed similar effects to those observed in Table 15 for the $l-3$ analysis and therefore the uncertainties in the lepton identification efficiencies were assumed to be the same as in the $l-3$ analysis; the quadratic sum of these errors was 3.6%. The $e\,\mu$ selection was more dependent on the minimum allowed energies of the leptons so an additional systematic error of 4% was assigned to account for this effect. This effect was presumed to be due to incorrect modeling of the momentum dependence of the PASS1 data filter efficiency.

After adding all the systematic errors in quadrature, the final result is

$$B_e\, B_\mu = 0.0288 \pm 0.0017 \pm 0.0019,$$

where the first error is statistical and the second is systematic.

4.4.4 Discussion of Leptonic Branching Ratio Results

The result $B_\mu/B_e = 1.02 \pm 0.07 \pm 0.04$ from the e-3 and μ-3 results,

$$B_e = 0.180 \pm 0.009 \pm 0.006$$

$$B_\mu = 0.183 \pm 0.009 \pm 0.005,$$

is consistent with 0.973, the value expected from e-μ universality, the previous world average of 0.94 ± 0.05,† and previous universality tests.[52] The result of the $e\mu$ analysis,

$$B_e\, B_\mu = 0.0288 \pm 0.0017 \pm 0.0019,$$

can be used as a constraint to reduce the errors on B_e and B_μ in a combined fit without making any assumptions such as e-μ universality. This combined

† This value of B_μ/B_e was calculated from the results in Table 2.

fit yields

$$B_e = 0.174 \pm 0.008 \pm 0.005$$

$$B_\mu = 0.177 \pm 0.008 \pm 0.005.$$

These results are compared with other results in Figures 33 and 34. When these results were published[41] only the results above them in Figures 33 and 34 had been published (apart from the bottom entry in each figure which comes from a measurement of $B_e B_\mu$ and the assumption of universality). Only the measurement of B_μ by Althoff *et al.* is in disagreement with the results of this experiment; The χ^2 between this result and the value of B_μ measured in this experiment is 5.6 for one degree of freedom. The result of the $e\mu$ analysis is consistent with previous measurements of $B_e B_\mu$ by Bacino *et al.*,[54] 0.34 ± 0.009, and Blocker *et al.*,[9] 0.030 ± 0.005.

The three branching ratio results can be combined with the assumption of e-μ universality ($B_\mu = 0.973\, B_e$) to yield

$$B_e = 0.178 \pm 0.005.$$

As was shown in section 1.5.1, the tau lifetime is related to the electron branching ratio by $\tau_\tau = B_e/\Gamma_e$, where $\Gamma_e = G_F^2 m_\tau^5/(192\,\pi^3)$. Similarly, the total decay rate of the muon, neglecting the mass of the electron, is $\Gamma_{\mu\to\nu_\mu e\bar{\nu}_e} = G_F^2 m_\mu^5/(192\,\pi^3)$. Therefore, the tau lifetime is simply related to the muon lifetime and the electron branching ratio of the tau,

$$\tau_\tau = B_e \left(\frac{m_\mu}{m_\tau}\right)^5 \tau_\mu. \tag{4.9}$$

Substitution of $B_e = 0.178 \pm 0.005$ and $\tau_\mu = 2.2 \times 10^{-6}$ sec in equation (4.9), yields a predicted tau lifetime of $(2.86 \pm 0.09) \times 10^{-13}$ sec, consistent with the world average of $(2.84 \pm 0.19) \times 10^{-13}$ sec (see Table 4).

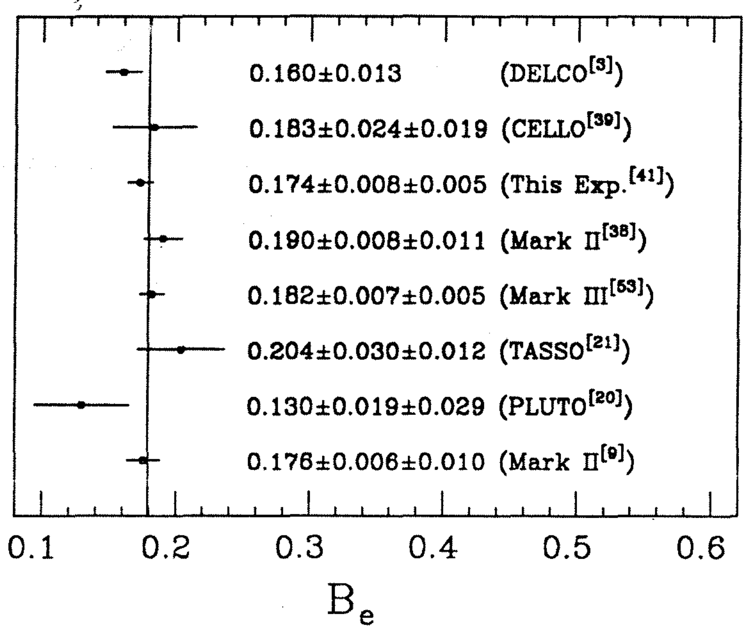

FIGURE 33. Measurements of B_e by different experiments. The vertical line indicates the world average value of B_e, 0.179 ± 0.006, excluding the result of this experiment. The result of Ref. 9 assumes e-μ universality.

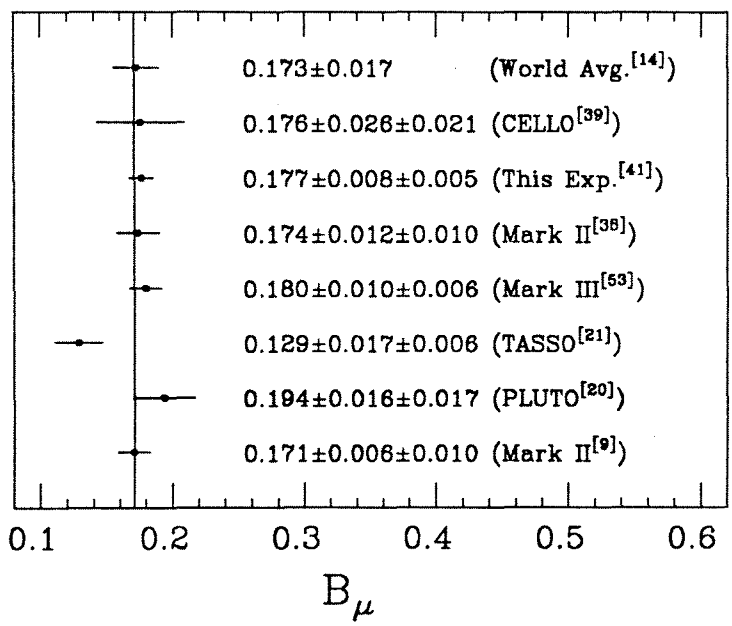

FIGURE 34. Measurements of B_μ by different experiments. The vertical line indicates the world average value of B_μ, 0.171 ± 0.007, excluding the result of this experiment. The "World Average" at the top of the figure is the average of six measurements made before the result of Ref. 41. The result of Ref. 9 assumes e-μ universality.

In section 1.6.3 there is a discussion of how well the sums of the 1-prong and 3-prong portions of the exclusive branching ratios agree with the measured inclusive branching ratios. One way to resolve the discrepancy is to assume that previous measurements of the tau lifetime and leptonic branching ratios have yielded results below their true values; if B_e were increased to 19.3% (a 3 standard deviation fluctuation of the present result) then most of the discrepancy would go away.[24] Since the present result is in agreement with previous and subsequent results, this is an unlikely solution to the discrepancy.

4.5 Measurement of the Pion Branching Ratio

The pion branching ratio was measured with data from the 1-1 and 1-3 samples. The branching ratio was extracted from the 1-3 sample with the same method used in the l-3 analysis, that is,

$$B_\pi = B_1\,(N_{\pi-3}/\epsilon_{\pi-3})/(N_{1-3}/\epsilon_{1-3}), \tag{4.10}$$

where $N_{\pi-3}$ and N_{1-3} are background subtracted numbers of observed $\pi - 3$ and $1 - 3$ events, $\epsilon_{\pi-3}$ and ϵ_{1-3} are efficiencies for detecting these types of events, and B_1 is the 1-prong branching ratio.

The pion branching ratio was measured in the 1-1 sample by observation of the fraction of tracks in the 1-1 sample that were identified pions, that is,

$$B_\pi = \frac{B_1}{2}\,(N_\pi/\epsilon_\pi)/(N_{1-1}/\epsilon_{1-1}), \tag{4.11}$$

where N_π is the number of tracks identified as pions, ϵ_π is the efficiency for detecting a pion in the 1-1 sample, N_{1-1} is the number of 1-1 events, and ϵ_{1-1} is the efficiency for detecting 1-1 events. This method, as opposed to the method in which the branching ratio is computed from the number of identified pion tracks in 1-1 events and the integrated luminosity times the cross section, tends to reduce systematic effects common to all 1-1 events such as uncertainties in the trigger efficiency, the hard electron cuts discussed in chapter 3, and the measurement of the integrated luminosity.

Table 17 shows the numbers relevant to the calculation of B_π for both samples. The branching ratios were computed with the same iterative procedure used in the $l-3$ analysis which allowed for the slight dependence of the background on the measured branching ratios. The most significant background was from the decay $\tau \rightarrow \nu_\tau \rho$ and so the study of systematics focused on how well these decays could be rejected from the sample. By variation of the cuts that defined a detected photon it was estimated that the uncertainty in the number of false showers and the soft photon detection efficiency contributed 0.004 to the systematic error in B_π. The results were also slightly sensitive to what fraction of the track calorimeter energy was required to be in the HC for which a systematic error of 0.002 was assigned. The $\pi-3$ result was completely insensitive to the number of vertex-fit tracks in the 3-prong (this is consistent with the observation of very slight dependence in the $l-3$ analysis) and no systematic error was assigned for uncertainty in the efficiency for reconstructing photon conversion pairs. The pion branching ratio measured with the luminosity method agreed well with the ratio method used for the 1-3 sample but for the 1-1 sample the results differed by about one standard deviation. Therefore a systematic error of about half the difference (0.003) was assigned to account for uncertainties in the ratio of the 1-1 selection efficiency to the efficiency for detecting 1-1 events containing one or two $\tau \rightarrow \nu_\tau \pi$ decays. The uncertainty in the background from $\tau \rightarrow \nu_\tau K$ decays was taken to be the 25% experimental error on the branching ratio B_K and contributed 0.0017 to the systematic error. The 5.4% experimental error on the branching ratio B_ρ contributed 0.001 to the systematic error.

Contributions to the systematic error from uncertainties in the branching ratios for multi-π^0 and multi-particle Cabbibo suppressed tau decays were negligible, due in part to the low level of these backgrounds. Uncertainties in the level of non-tau background in the 1-1, 1-3, π-3, and π-1 samples made negligible contributions to the systematic error in comparison with the other systematics listed here.

The branching ratio was observed to be dependent on the maximum allowed $|\cos\theta|$ of the detected pion, both in the 1-1 and 1-3 samples, possibly due to incorrect modeling of the pion detection efficiency or background rejection in various regions of the detector and a systematic error of 0.002 was assigned for this effect. The branching ratio was also found to be sensitive in both samples to the minimum allowed CD momentum and a systematic error of 0.004 was assigned for the uncertainty in the momentum dependence of the detection efficiency and background rejection that was perhaps not accounted for by variation of the pion identification criteria.

The final pion branching ratio results are

$$B_\pi = \begin{cases} 0.108 \pm 0.005 \pm 0.008 & \text{(1-1 sample)} \\ 0.103 \pm 0.010 \pm 0.007 & \text{(1-3 sample)} \end{cases},$$

where the first errors are statistical and the second are systematic (all the systematic errors discussed above were added in quadrature). These two results can be combined to yield

$$B_\pi = 0.106 \pm 0.004 \pm 0.008,$$

where the statistical and systematic errors have been combined in such a way as to reflect the fact that most of the systematic uncertainty is common to the two measurements. This result is consistent with previous measurements made by Blocker *et al.*,[9] $0.117 \pm 0.004 \pm 0.018$, and Behrend *et al.*,[39]

TABLE 17. Numbers relevant to the calculation of B_π for both 1-1 and 1-3 samples. An event with two identified pions in the 1-1 sample was counted as two "events" in the π_{1-1} column.

	1-1	π_{1-1}	1-3	π-3
No. of observed events	5432 ± 74	646 ± 25	3337 ± 58	152 ± 12
Efficiency (%)	25.2 ± 0.1	9.64 ± 0.18	47.4 ± 0.3	14.0 ± 0.5
Backgrounds:				
1-1	...	...	116 ± 5	8 ± 1
1-3	32 ± 2	14 ± 2	...	...
3-3	1 ± 1	$<< 1$	5 ± 1	$<< 1$
$\tau \rightarrow \nu_\tau \rho$	...	86 ± 4	...	23 ± 2
other tau decays	...	43 ± 3	...	11 ± 2
$ee\tau\tau$	17 ± 2	4 ± 2	44 ± 5	3 ± 1
$eeq\bar{q} + q\bar{q}$	33 ± 9	4 ± 1	142 ± 13	6 ± 3
$eeee + ee\mu\mu$	73 ± 11	< 1	$<< 1$	$<< 1$
$\mu\mu$ + cosmics	45 ± 15	< 1	$<< 1$	$<< 1$

$0.099 \pm 0.017 \pm 0.013$. The ratio of the pion to electron branching ratio of the tau is given by[23]

$$\frac{B_\pi}{B_e} = \frac{(f_\pi \cos\theta_c)^2}{m_\tau^2} 12\pi^2 \left(1 - \frac{m_\pi^2}{m_\tau^2}\right)^2 = 0.607,$$

where the quantity $f_\pi \cos\theta_c$, the form factor at the W-π vertex, is precisely determined in the decay $\pi \rightarrow \mu\bar{\nu}_\mu$. The ratio of B_π measured here to the world average value of B_e[14] is $B_\pi/B_e = 0.60 \pm 0.05$, where the errors, including the contribution due to the total error in the average electron branching ratio, have been added in quadrature. This result is consistent with the theoretical prediction of 0.607. The pion branching ratio is given by the product of the measured tau lifetime and the calculated decay rate $\Gamma_{\tau\to\pi}$. With $\tau_\tau = (2.84 \pm 0.19) \times 10^{-13}$ sec and $\tau_\pi = 2.6 \times 10^{-8}$ sec,[14] the predicted pion branching ratio is

$$B_\pi = \frac{\tau_\tau}{2\tau_\pi} \frac{m_\tau^3 \,(1 - \frac{m_\pi^2}{m_\tau^2})^2}{m_\pi \, m_\mu^2 \,(1 - \frac{m_\mu^2}{m_\pi^2})^2} = 0.109 \pm 0.007,$$

consistent with the value measured in this experiment.

4.6 Search for Tau Decays to Five Charged Hadrons

A sample of events with the 1-5 topology was formed, as a subsample of the general tau-pair event sample, by the event selection procedure described in Chapter 3 (see especially item 1 of Section 3.3). The branching ratio for tau decaying to five charged hadrons plus ν_τ (and perhaps a π^0), B_5, was measured by counting the number of events with the 1-5 charge topology in which the 1-prong was identified as something other than an electron. Elimination of the 3-5 and 5-5 topologies reduced the background from the processes $e^+e^- \to q\bar{q}$, $e^+e^- \to e^+e^-q\bar{q}$, and $e^+e^- \to e^+e^-\tau^+\tau^-$, especially the former. The requirement that the 1-prong not be an electron provided additional background rejection against multi-hadron or tau-pair events produced in two-photon collisions. The number of 1-5 events in which the 1-prong is not an electron represents about 70% of all events containing a tau decay to five charged hadrons.

Due to the radius and granularity of the central drift chamber and the smallness of the typical angle between tracks in the 5-prong jet, the probability that one of the charged tracks overlapped another was nearly 50%. Therefore, in order to reduce the possible systematic error for the probability of finding all five charged tracks and to increase the statistical sensitivity of this measurement, events with a 1-4 charge topology were allowed into the 1-5 sample.

The requirements discussed thus far produced a sample with a signal to background ratio much less than 1, assuming that $B_5 < 1\%$. In order to reduce hadronic and other similar backgrounds the following additional requirements were imposed on the data:

- total energy in the calorimeters between 6 and 23 GeV;
- charged particle sphericity less than 0.035;
- no neutrals with energy greater than 1 GeV more than 30° from the charged particle sphericity axis;
- if the single charged prong was called a ρ by the by the particle identification algorithm, its invariant mass, computed from the charged track and reconstructed neutral shower(s), was less than 1.5 GeV/c^2;
- the invariant mass of the 5-prong system, computed from the positions and energies of calorimeter hits, was less than 4 GeV/c^2;
- the scalar sum of all CD momenta was greater than 4 GeV/c.

These requirements reduced the background from processes other than $e^+e^- \rightarrow \tau^+\tau^-$ to manageable levels but the background from tau-pair events of the 1-3 charge topology with an additional pair of tracks from a conversion of a photon in the material before the CD (total of 0.036 radiation lengths at normal incidence) remained large. An estimate of this background can be formed from the conversion probability (P_c) and the fraction of 3-prong decays which are accompanied by a π^0 (f_{π^0}):

$$B_{3+pair} = B_3 \, f_{\pi^0} \, 2 \, P_c \simeq 0.4\%$$

where P_c is the conversion probability averaged over solid angle and f_{π^0} is the fraction of 3-prongs accompanied by a π^0. This background is large compared with previous measurements of B_5. In order to reduce this background, events with a satisfactory χ^2 for the fit to the pair conversion hypothesis were rejected. Events in the 1-4 sample were required to have all jet tracks pass a loose vertex fit and have a momentum greater than 0.25 GeV/c. The number of events left after imposing all the cuts discussed above was 11 of which only 2 were of the 1-5 charge topology. A closeup view of the CD hits and reconstructed tracks for these two events can be seen in Figure 35.

The detection efficiency for this type of event was $(9.2 \pm 1.5)\%$. It was assumed that half of the 5-prong tau decays were $\tau \rightarrow \nu_\tau 5\pi$ and half $\tau \rightarrow \nu_\tau 5\pi\pi^\circ$. Both decay modes were given continuum mass distributions with $m > 1100$ MeV/c^2. The uncertainty in the detection efficiency is dominated by the difference in the detection efficiencies for the two decay modes and the uncertainty (assumed to be $\pm 100\%$) in the admixture of the 5π and $5\pi\pi^\circ$ branching ratios. The detection efficiency for the former was 25% larger than for the later due to the larger opening angles between the charged tracks from the decays with fewer particles.

The estimated backgrounds, computed with Monte Carlo calculations, are listed in Table 18. Approximately 50% of the tau 1-3 background was from photon conversion pairs, 20% from π° Dalitz decays, and 30% from 1-3 events with spurious extra tracks. The number of observed events was completely consistent with the expected background and therefore only an upper limit on B_5 was set. The upper limit on B_5 was estimated with the maximum likelihood method. The numbers of 1-5, 1-3 + pair, and multihadron events were assumed to come from Poisson distributions and the likelihood function was therefore

$$L = \frac{(n_{mh})^{N_{mh}} e^{-n_{mh}}}{N_{mh}!} \frac{(n_{13})^{N_{13}} e^{-n_{13}}}{N_{13}!} \frac{(n_{15})^{N_{15}} e^{-n_{15}}}{N_{15}!},$$

where N (n) were the observed (fitted) numbers of events. The reason for

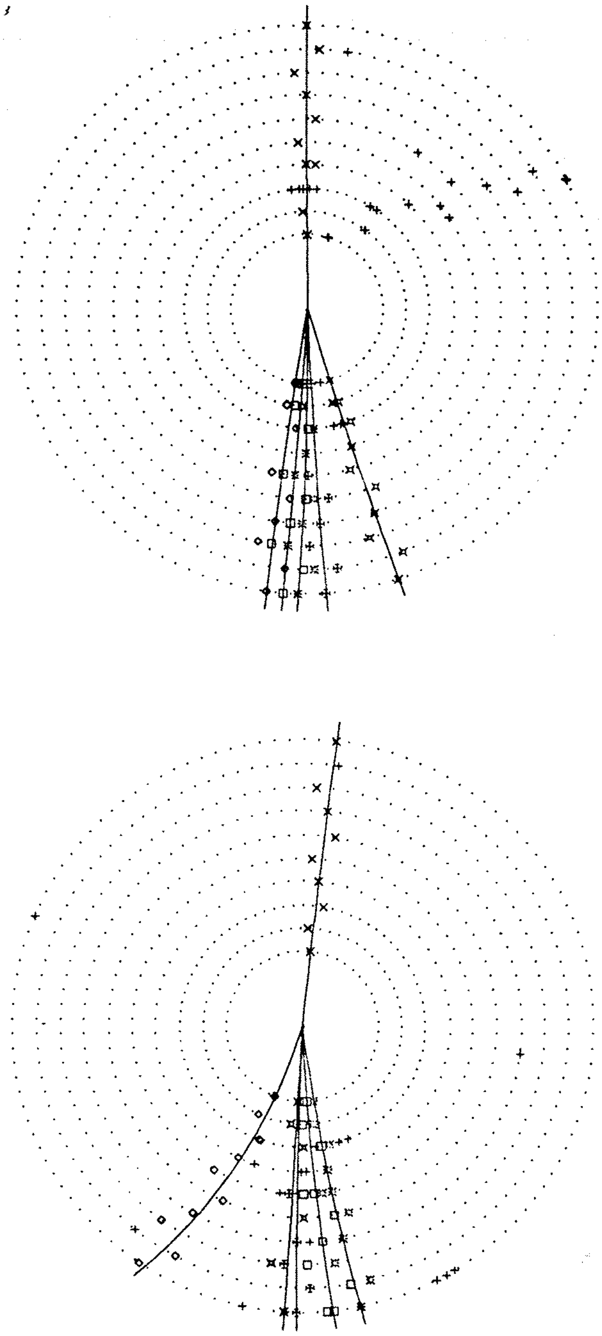

FIGURE 35. Closeup view of candidate 5-prong tau decays. In these end views of the CD, each track is assigned a different symbol for its hits. Hits not assigned to a track are denoted with a vertical cross. The staggering of the hits is due to the stereo layers. These are the only 5-prong candidates with six reconstructed tracks (another nine have five tracks).

including the numbers of multihadron and 1-3 events in the likelihood function was that the statistical errors on these background estimates were not at all negligible compared with the number of observed events. Since the systematic errors were substantial, they were incorporated into the error estimate in the following manner. First, the 95% confidence level upper limit on B_5 was found by locating the point at which the log likelihood was decreased by 2 from its maximum value while the likelihood was maximized with respect to both n_{mh} and n_{13}. This result ($B_5 < 0.0022$) was then multiplied by $(1+\delta)$ where δ was the quadratic sum of the following errors:

- 16% due to the error on the 1-5 efficiency;
- 3% due to the error on B_3;
- 15% due to the uncertainty in f_{π^0};
- 10% due to systematic uncertainty in the selection efficiency and background rejection.

TABLE 18. Estimated backgrounds in 1-5 event sample.

	1-4 events	1-5 events
No. of observed events	9	2
Multihadron background	1 ± 1	< 1
Tau 1-3 background	7.3 ± 0.9	1.5 ± 0.3

The systematic uncertainty in selection efficiency and background rejection was estimated by comparing the number of observed events with the predicted number of background events at several different stages as the selection criteria were successively applied. The systematic uncertainty was taken to be the average of the absolute values of the percentage differences between the data and the background predictions. The final result is that $B_5 < 0.0027$ at the 95% confidence level. This result is consistent with all the upper limits and measurements listed in Table 3. The calculation of B_5, rather than the upper limit on B_5, yielded $B_5 = 0.0003^{+0.0010}_{-0.0003}$ (error is statistical only), also consistent with the results of the other experiments.

After a previous version of this analysis was published[26], two experiments at PEP observed about a dozen 5-prong tau decays with little background. The average of their measurements[31,32] is $B_5 = 0.0014 \pm 0.0004$ (systematic and statistical errors were combined in quadrature). The successful observation of this rare topology with essentially no background by these other experiments was made possible by the large size and fine granularity of their central drift chambers and the small amount of material in front of them.

4.7 Tau Polarization Measurement

It was demonstrated in chapter 1 that the combination of a weak contribution to tau-pair production and the $V - A$ nature of tau decay affect the energy spectra of tau decay products. Both the average energy and the energy asymmetry were measured in this experiment and were interpreted as measurements of the average tau polarization and polarization asymmetry respectively. Since the PEP beams were not polarized, the only source of tau polarization was the weak production and therefore this experiment consisted of measurements of the products $g_v^e g_a^\tau$ and $g_a^e g_v^\tau$. Since g_a^τ, g_v^e, and g_a^e have already been more precisely measured elsewhere,[16–21,51,55] the focal point of this experiment was to measure the polarization asymmetry to determine g_v^τ. However, the measurement of the average polarization will be described along with the polarization asymmetry to bring attention to the fact that, whereas effects that bias the average energy have a large effect on the measurement of $g_v^e g_a^\tau$, the polarization asymmetry consists of a difference which reduces almost all systematic errors in $g_a^e g_v^\tau$ to negligible levels. This is true of both additive effects (such as particle misidentification background) and multiplicative effects (such as the beam energy).

The average energy as a function of polar angle $\langle E\rangle(\theta)$ can be calculated from the differential decay rates given in chapter 1 and can be written in the form

$$\langle E\rangle(\theta) = E_{beam}\left[a + b\,P(\theta)\right], \tag{4.13}$$

where E_{beam} is the beam energy, P is the polarization, and a and b are constants which are characteristic of a particular decay mode. It follows that the energy and energy asymmetry averaged over polar angle, $\langle E\rangle$ and A_E respectively, are

$$\langle E\rangle = E_{beam}\left(a + b\,\langle P\rangle\right) \tag{4.14}$$

$$A_E = b\,E_{beam}\,A_P. \tag{4.15}$$

The energy asymmetry is defined by $A_E = (\langle E\rangle_F - \langle E\rangle_B)/2$, where $\langle E\rangle_F$ and $\langle E\rangle_B$ are the average energies for $\cos\theta > 0$ and $\cos\theta < 0$ respectively. Radiative corrections to tau-pair production reduce the average tau energy and also introduce a small energy asymmetry to the taus. To account for these corrections as well as other effects such as momentum acceptance, solid angle acceptance (in the case of the polarization asymmetry), particle identification, and non-tau backgrounds, it is convenient to write equations (4.14) and (4.15) in terms of the weak coupling constants and the corresponding effective coefficients,

$$\langle E\rangle = E_{beam}\left(a' + b' g_a^\tau\, g_v^e\right) \tag{4.16}$$

$$A_E = b''\,E_{beam}\,g_a^e\, g_v^\tau + \delta_A. \tag{4.17}$$

Table 19 lists the average energies and energy asymmetries for the four decay modes used in this analysis and the Monte Carlo predictions for the standard model (i.e., $V-A$ tau decays, massless neutrinos, the values of weak coupling constants measured in other experiments, and the values of branching ratios listed in Table 9). The central drift chamber momenta were used for the energy measurements except in the case of $\tau \rightarrow \nu_\tau \rho$ decays for which it was necessary to use the SC to measure the energy of π°'s. To reduce the effect of the small fraction of decays with very large measured momenta ($p >> E_{beam}$) on the means and widths of the momentum spectra, the spectra were saturated at 20 GeV/c (the momentum was set to the minimum of the measured momentum and 20 GeV/c). Although it was possible to reduce the fraction of events with very large measured momenta (with a corresponding reduction in the widths of the momentum spectra) by combination of the CD momentum with the momentum measured by another device (the OD for muons, the SC for electrons, the SC+HC for pions), the systematic error introduced due to uncertainty in the energy calibration of these devices offsets any reduction of the statistical error achieved by reduction of the widths of the momentum spectra. The Monte Carlo predictions in Table 19 include the effects of backgrounds and efficiencies. The values of measured $\langle E \rangle$ and A_E in Table 19 have had non-tau backgrounds subtracted from them; the background fractions were less than 3% and had negligible effects on the results. The values of the energy spectrum parameters a and b are also listed in Table 19 along with the effective energy spectrum parameters a', b', b'', and δ_A. The errors have been omitted where they are negligible. Figures 36-43 show the $\cos\theta$ and momentum distributions for the four decay channels. The observed distributions are compared with the Monte Carlo predictions (not including non-tau backgrounds, which are negligible). Some of the bin to bin fluctuations in the Monte Carlo predictions are due to the limited statistics of the Monte Carlo sample. The structure seen in the $\cos\theta$ distribution of Figure 40 is due to the non-uniformity of the outer drift chamber coverage. The excellent agreement between the data and the Monte Carlo predictions of the $\cos\theta$ distributions for the four decay modes means that the effective coefficients b'' have been computed with the correct $\cos\theta$ dependence for the $3x^2/(3x+x^3)$ factor in equation 1.18. The Monte Carlo and observed momentum spectra are in good agreement except for the decay $\tau \to \nu_\tau \rho$ (Figure 43). This discrepancy will be discussed in Section 4.7.4.

TABLE 19. Measurements and constants for calculation of polarization. Quoted errors are statistical only.

	$\tau \to \nu_\tau e \bar{\nu}_e$	$\tau \to \nu_\tau \mu \bar{\nu}_\mu$	$\tau \to \nu_\tau \pi$	$\tau \to \nu_\tau \rho$
No. of obs. events	1823	1909	798	3158
$\langle E \rangle$ (GeV)	5.578 ± 0.101	6.761 ± 0.105	8.514 ± 0.201	8.073 ± 0.065
A_E (GeV)	-0.049 ± 0.101	-0.060 ± 0.093	-0.074 ± 0.201	0.065 ± 0.065
$\langle E \rangle$ (GeV) pred.	5.656 ± 0.047	6.646 ± 0.039	8.590 ± 0.077	8.768 ± 0.031
A_E (GeV) pred.	0.037 ± 0.047	-0.024 ± 0.035	-0.071 ± 0.077	-0.006 ± 0.031
a	0.350	0.355	0.503	0.598
b	-0.050	-0.051	0.168	0.063
a'	0.3901 ± 0.0032	0.4586 ± 0.0027	0.5898 ± 0.0027	0.6044 ± 0.0021
b'	-0.0110	-0.0146	0.0360	0.0134
b''	-0.0050	-0.0096	0.0259	0.0091
δ_A	0.038 ± 0.047	-0.021 ± 0.035	-0.072 ± 0.0077	-0.006 ± 0.031

The effective energy spectrum parameters were determined with a Monte Carlo calculation. The Monte Carlo sample, which corresponded to an integrated luminosity of 1200 pb^{-1} (which is about six times that of the data), was created with a record of all information needed to re-weight

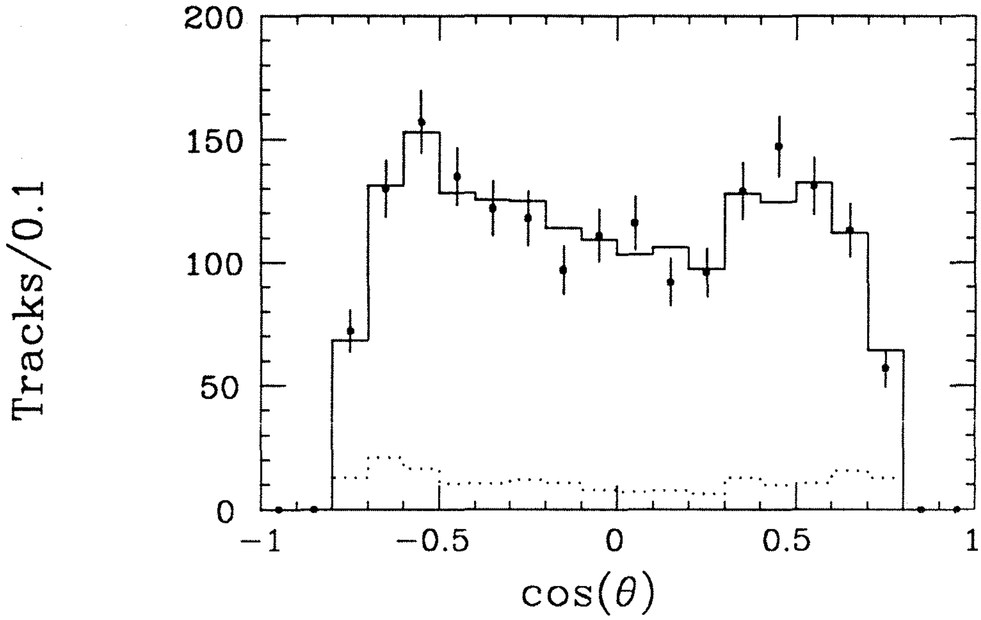

FIGURE 36. Observed charged $\cos\theta$ distribution for $\tau \rightarrow \nu_\tau e \bar{\nu}_e$. The solid curve shows the Monte Carlo prediction and the dotted curve shows the particle misidentification background.

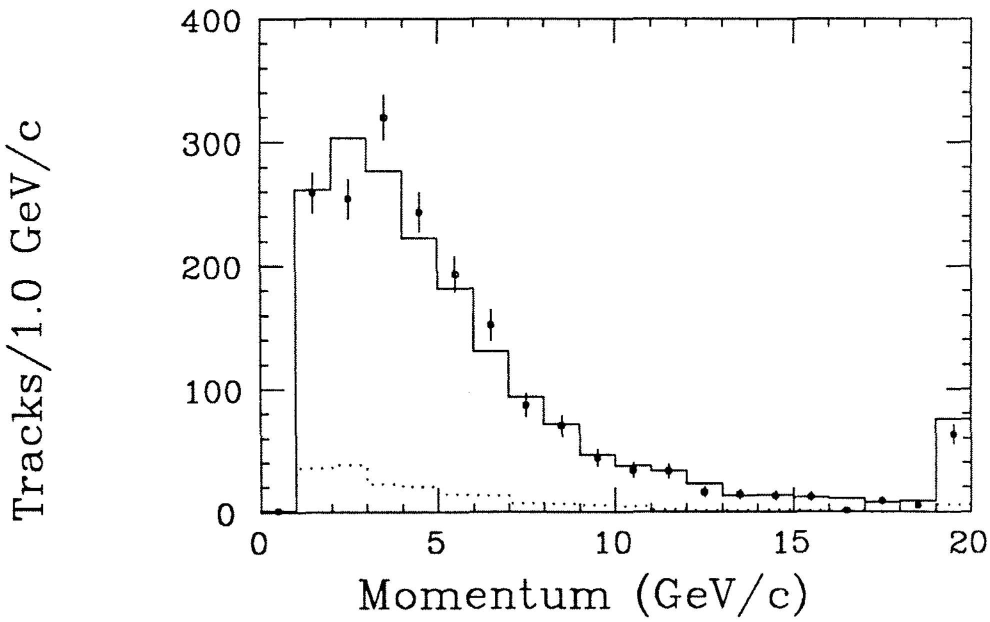

FIGURE 37. Momentum spectrum for $\tau \rightarrow \nu_\tau e \bar{\nu}_e$. The solid curve shows the Monte Carlo prediction and the dotted curve shows the particle misidentification background.

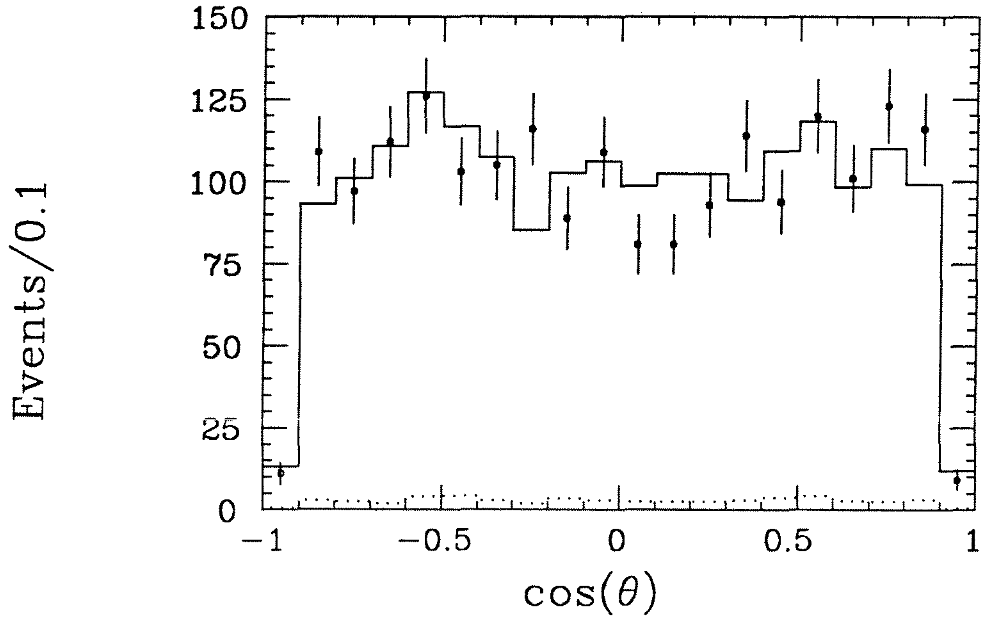

FIGURE 38. Observed charged $\cos\theta$ distribution for $\tau \to \nu_\tau \mu \bar{\nu}_\mu$. The solid curve shows the Monte Carlo prediction and the dotted curve shows the particle misidentification background.

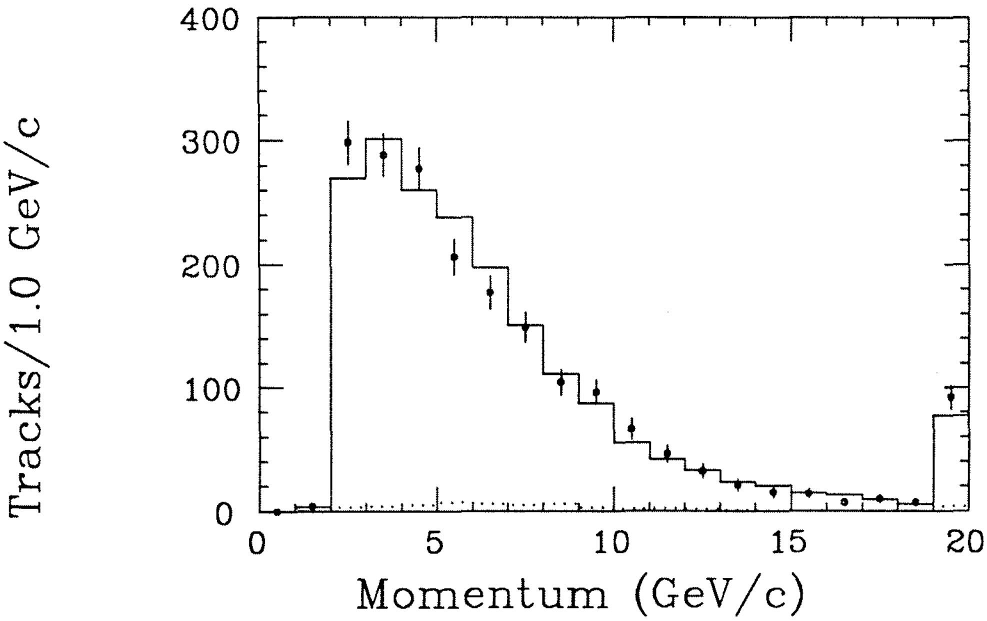

FIGURE 39. Momentum spectrum for $\tau \to \nu_\tau \mu \bar{\nu}_\mu$. The solid curve shows the Monte Carlo prediction and the dotted curve shows the particle misidentification background.

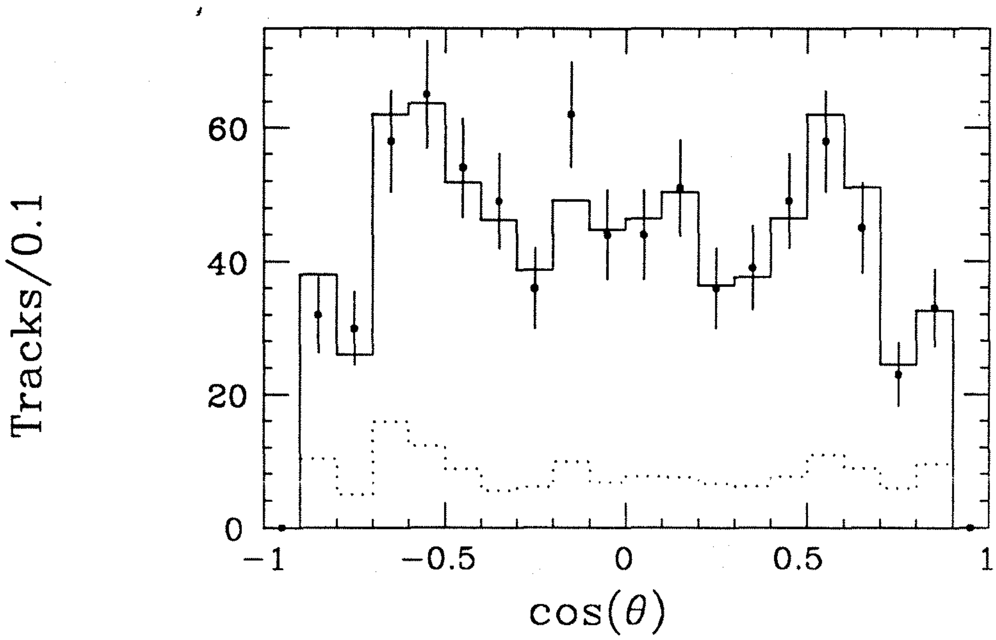

FIGURE 40. Observed charged $\cos\theta$ distribution for $\tau \rightarrow \nu_\tau \pi$. The solid curve shows the Monte Carlo prediction and the dotted curve shows the particle misidentification background. Most of the structure seen here is due to the portions of the solid angle not covered by the OD.

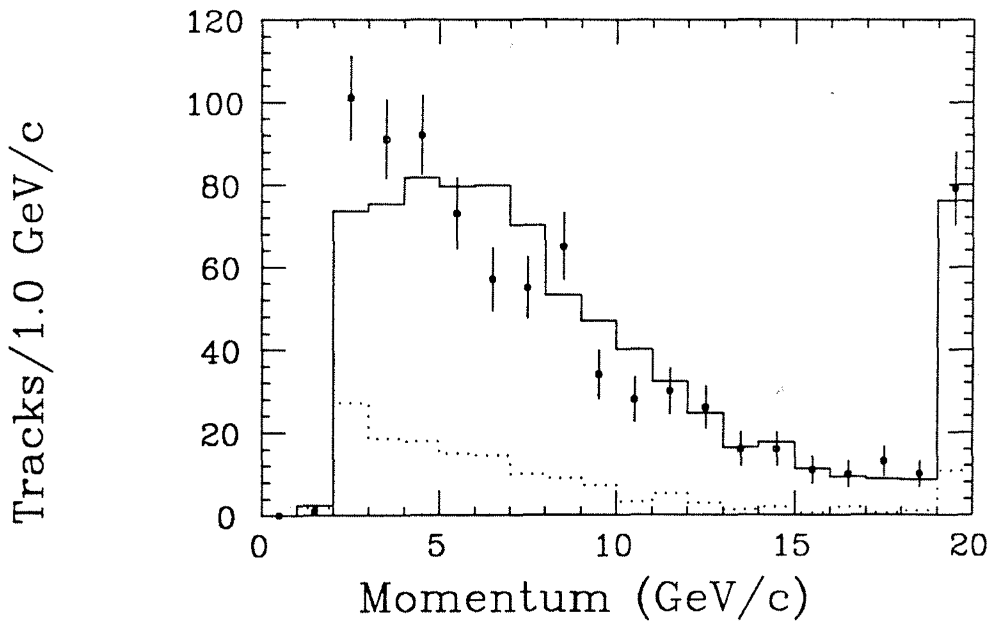

FIGURE 41. Observed momentum spectrum for $\tau \rightarrow \nu_\tau \pi$. The solid curve shows the Monte Carlo prediction and the dotted curve shows the particle misidentification background.

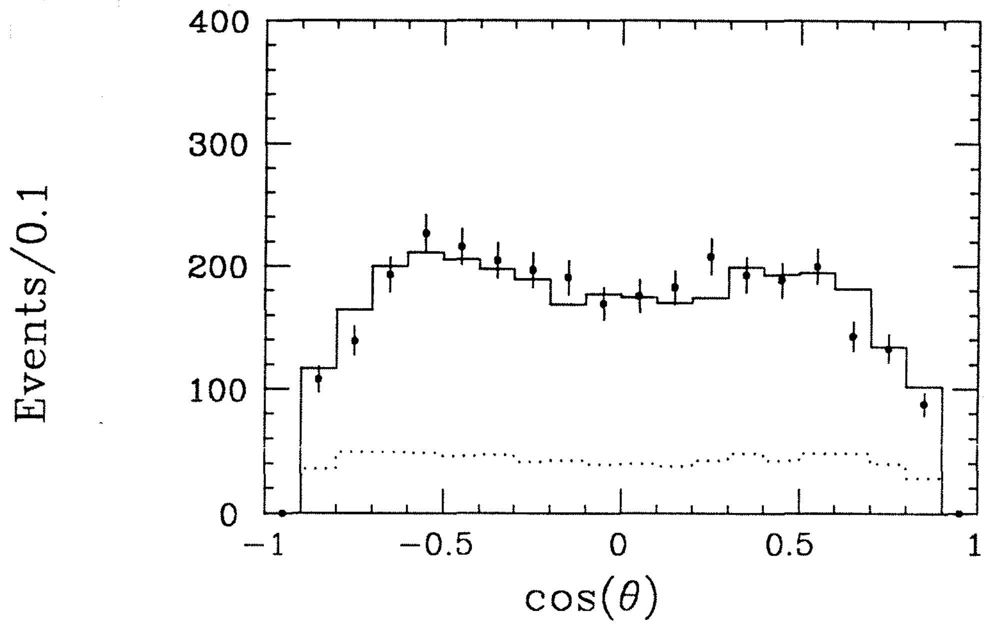

FIGURE 42. Observed charged $\cos\theta$ distribution for $\tau \to \nu_\tau \rho$. The solid curve shows the Monte Carlo prediction and the dotted curve shows the particle misidentification background.

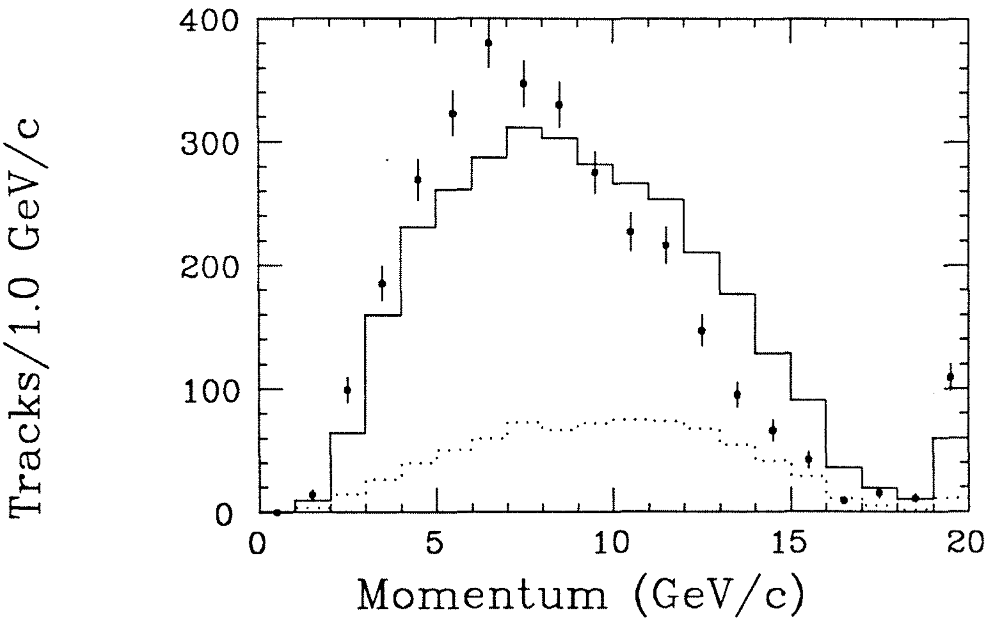

FIGURE 43. Observed momentum spectrum for $\tau \to \nu_\tau \rho$. The solid curve shows the Monte Carlo prediction and the dotted curve shows the particle misidentification background.

events with different values of the weak coupling constants. This allowed measurement of the sensitivity of a particular effect to changes in the coupling constants. Since the axial-vector couplings have been measured with much better precision than the current measurements of the vector couplings, it was assumed that these were known and only the vector coupling constants were varied. The average energy and energy asymmetries were almost perfectly linear in the vector coupling constants over the pertinent range. Negligible deviations of $\langle E \rangle$ and A_E from linearity in g_v^e and g_v^τ were observed when the vector coupling constants were allowed to vary as much as ± 2. These deviations occurred because the momentum spectra were changing and the momentum acceptance sightly modified the fraction of the spectra that were observed. There were also small effects caused by small changes in the signal to background ratios in the various channels. Although there were statistical errors on a' and δ_A, they were determined with a factor of six more events than the data and therefore their contribution to the total error was small. Since b' and b'' were determined by variation of the vector coupling constants, their statistical errors were expected to be negligible.†

4.7.1 Radiative Corrections to Tau Production

It is clear that initial state radiation can't cause a tau to flip its spin. Depolarization due to the flipping of the spin of a high energy tau by final state radiation is also negligible by approximate helicity conservation for high energy Dirac fermion currents.[56] Approximately 6% of the total cross section for tau-pair production has a radiated photon from the final state and since the bremsstrahlung spectrum is proportional to $1/k$, where k is the photon energy, the fraction of events for which the radiated photon energy

† It was noted that the distributions of b' and b'', for 10 equal subsamples of the Monte Carlo sample, indicated that the statistical errors on these quantities were less than 3%.

is large enough for the high energy approximation of the tau propagator to break down (~ 8 GeV) is very small.

The effects of soft bremsstrahlung and vertex corrections were estimated using the calculations of Bŏhm and Hollik.[57] At $\sqrt{s} = 29$ GeV these corrections decrease the average polarization by $\sim 2\%$ when the maximum allowed radiated photon energy is less than 20% of the beam energy. The largest corrections occur for $\cos\theta \sim -1$, where the polarization is nearly zero. Figure 44 shows the polarization as a function of polar angle for the expected values of the coupling constants. Since these effects were far smaller than the sensitivity of this experiment, they were ignored.

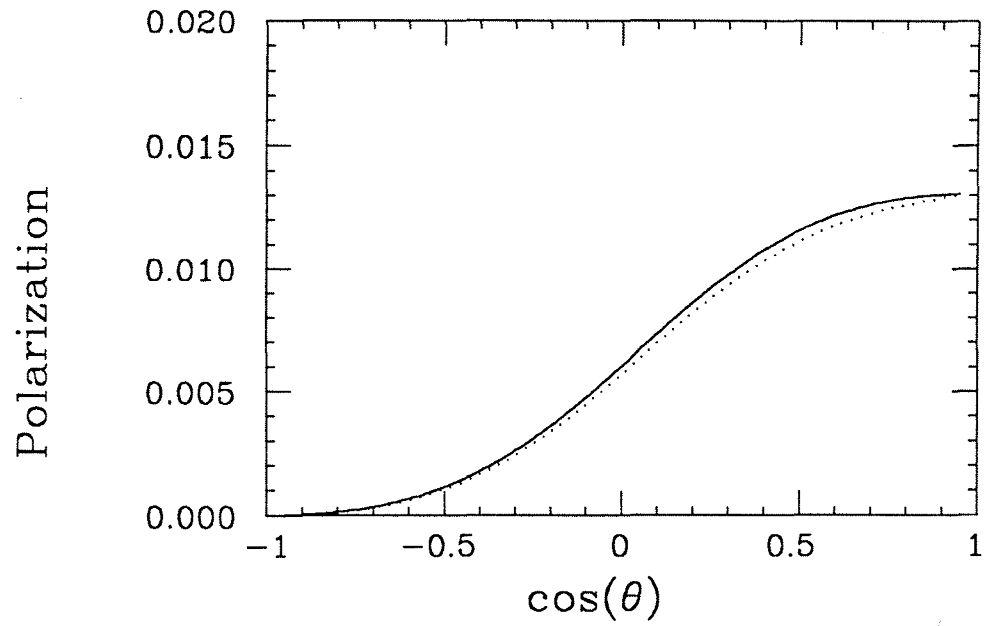

FIGURE 44. Polarization as function of polar angle for the expected values of the coupling constants. The dotted curve shows the effects of radiative corrections.

Although it has been shown that radiative corrections have little effect on the polarization, radiation reduces the average center of mass energy and therefore also the average energy of the tau decay products. Radiative corrections also produce a small energy asymmetry of the taus themselves. It is therefore necessary to correct the data for radiative corrections before attempting to interpret the observed average energy and energy asymmetry. The event generator of Berends, Kleiss, and Jadach (BKJ), which incorporates their calculations of radiative corrections to order α^3, was used to generate tau-pair events.[58] The tau decay distributions were evaluated in the center of mass and then transformed to the laboratory. This procedure is valid since it has been shown that radiative corrections don't modify the tau polarization appreciably. Figure 45 shows the average energy and energy asymmetry of the taus as functions of the maximum allowed acollinearity angle (this is equivalent to the requirement of a maximum allowable photon energy). Because of the two to four neutrinos which are present in each event and the effects of detector resolution, the data sample for this experiment did not have a well defined maximum photon energy. However, since the tau average energy and energy asymmetry are not strongly dependent on the maximum photon energy, the radiative corrections effects are well understood. The corrections were made by absorbing them in the energy measurement parameters listed in Table 19. It was verified by running the BKJ event generator for various values of g_v^τ that there was a negligible effect on the tau average energy and energy asymmetry when it was varied within reasonable limits (± 1). Varying g_v^e within its experimental error ($g_v^e = -0.05 \pm 0.09$) also had little effect on the tau average energy and energy asymmetry.

The ability of the BKJ event generator to model the data has been checked in the reaction $e^+e^- \to \mu^+\mu^-(\gamma)$.[59] Further evidence of the validity of these calculations has been found by studying this process for photon energies above 1 GeV.[60] The agreement of the tau data with the Monte Carlo in the acollinearity distribution, shown in Figure 15, although a less sensitive test than the mu-pairs, also indicates that the calculations are

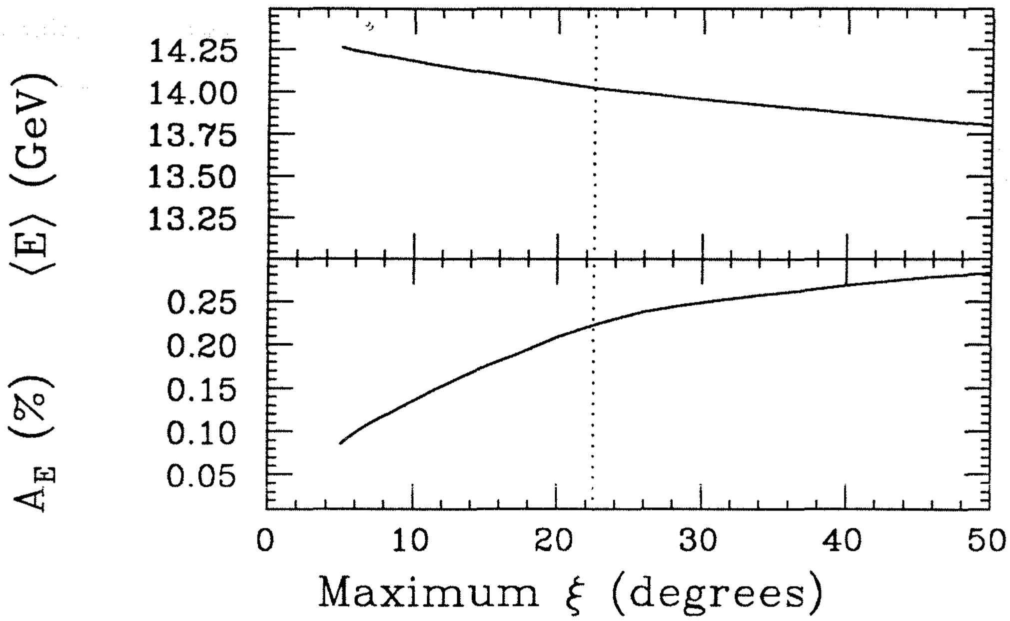

FIGURE 45. Average τ energy and energy asymmetry as functions of the maximum allowed acollinearity angle (ξ). The vertical dotted line indicates the effective maximum allowed ξ for the data sample.

correct. Finally, the charge asymmetry in radiative events from the process $e^+e^- \rightarrow \tau^+\tau^-\gamma$ has been measured and found to be in agreement with the BKJ Monte Carlo prediction.[21]

Since there is no evidence that the BKJ calculations and event generator fail to reproduce the data, it was assumed that at worst the systematic errors could be 10% of the size of the radiative effects. This is about the level at which radiative corrections to the tau and mu-pair total cross sections have been checked. Since $\langle E \rangle$ scales directly with the tau energy and the average tau energy was 96.6% of the beam energy, a systematic error of $(1 - 0.966) \times 10\% = 0.34\%$ was assigned for $\langle E \rangle$ in all four channels. Since this effect cancels out to a first approximation in the energy asymmetry, no systematic error was assigned for A_E. With analysis acceptance included, the calculated tau energy asymmetry was 0.11% and since A_E scales directly with this asymmetry, this would result in a systematic error of 0.01% which is completely negligible.

4.7.2 Radiative Corrections to Tau Decay

Radiative corrections to the differential decay rate for the weak decay $\mu \rightarrow \nu_\mu e \bar{\nu}_e$ have been calculated and can be applied directly to leptonic tau decays.[61] The calculation, which included virtual and bremsstrahlung diagrams, was carried out to first order in α. The calculation was used here to estimate the effect of radiative corrections on measured $\langle E \rangle$ and the sensitivity to the polarization. With the assumption of $V - A$ interactions and massless decay leptons (except in the radiative correction functions where the mass m_l is important), the differential decay rate in the tau center of mass is

$$\begin{aligned} \frac{d^2\Gamma(x,\theta)}{dx\, d\cos\theta} =& \frac{G^2 m_\tau^5}{384\,\pi^3} x^2 \left\{ [3 - 2\,x + f_c(x)] \right. \\ & \left. + P \cos\theta \,[1 - 2\,x + f_\theta(x)] \right\}, \end{aligned} \tag{4.18}$$

where x is the energy of the decay electron or muon relative to its maximum possible energy and θ is the decay polar angle (in the tau center of mass). The functions f_c and f_θ are

$$\begin{aligned} f_c(x) =& \frac{\alpha}{2\,\pi} \left\{ 2\,(3 - 2\,x)\, R(x) - 3\, \log x \right. \\ & \left. + \frac{1-x}{3\,x^2} \left[(5 + 17\,x - 34\,x^2) \log \frac{x\, m_\tau}{m_l} - 22\,x + 34\,x^2 \right] \right\} \\ f_\theta(x) =& \frac{\alpha}{2\,\pi} \left\{ 2\,(1 - x)\, R(x) - \log x - \frac{1-x}{3\,x^2} \left[(1 + x + 34\,x^2) \log \frac{x\, m_\tau}{m_l} \right. \right. \\ & \left. \left. + 3 - 7\,x - 32\,x^2 + \frac{4\,(1-x)^2}{x} \log(1-x) \right] \right\} \end{aligned} \tag{4.19}$$

where $R(x)$ is defined by

$$\begin{aligned} R(x) =& \left(\log \frac{x\, m_\tau}{m_l} - 1 \right) \left(\log \frac{1-x}{x} + \frac{3}{2} \right) + \log(1-x) \left[\log x + 1 - \frac{1}{x} \right] \\ & - \log x + 2\, L_2(x) - \frac{\pi^2}{3} - \frac{1}{2} \end{aligned} \tag{4.20}$$

and L_2 is Euler's dilogarithm, $L_2(x) = - \int_0^x (\log(1-t)/t) dt$. When integrated over the energy spectrum and solid angle, these radiative corrections change the average electron and muon energy in the laboratory by the amounts shown in Table 20. Also shown in Table 20 are the amounts by which the energy asymmetries are decreased. To account better for the corrections to the data samples, the analysis acceptance was included in the energy and solid angle integrations, i.e., only laboratory energies greater than 1 (2) GeV for the electronic (muonic) decay modes were included. The results of these calculations are also summarized in Table 20. The corrections to the average energy were not negligible for the electronic decay mode. Since these corrections were not implemented in the Monte Carlo event generator, it was decided to correct the data. The procedure adopted was to correct measured $\langle E \rangle$ and A_E directly according to the amounts listed in the second row of Table 20.

TABLE 20. Effect of radiative corrections to leptonic τ decay on $\langle E \rangle$ and A_E. These corrections were calculated without the detector simulation. The analysis momentum acceptance of 1 (2) GeV/c for electrons (muons) is a rough approximation of the actual momentum acceptance.

	$\tau \to \nu_\tau e \bar{\nu}_e$		$\tau \to \nu_\tau \mu \bar{\nu}_\mu$	
	$\delta\langle E \rangle$	δA_E	$\delta\langle E \rangle$	δA_E
Rad. corr. to entire spectrum	−2.0%	−2.2%	−0.3%	−0.6%
Rad. corr. to accepted spectrum	−1.4%	−1.5%	−0.2%	−0.6%

Calculations of radiative corrections to the decay $\tau \to \nu_\tau \pi$ exist but only for the total decay rate and not the differential decay rate.[62] Nevertheless, since the pion mass, and those of all other tau decay products, are larger than the muon mass, the corrections to all but the electronic decay mode are expected to be negligible.

Since the radiative corrections to the leptonic tau decays were done without the detector simulation and event selection, a conservative systematic error was assigned as half the difference between the corrections with and without the approximate energy cut of 1 (2) GeV for electrons (muons). This implies a systematic error in $\langle E \rangle$ of 0.3% for the electronic decay mode and 0.05% for the muonic decay mode. Similarly, a systematic error of 0.35% was assigned due to uncertainty in the radiative corrections to the energy asymmetry of the electronic decay mode. No systematic error was assigned to A_E for the muon decay mode since applying the analysis momentum acceptance had no effect on A_E. Since the radiative corrections to the hadronic decays were assumed to be negligible, no systematic errors were assigned to $\langle E \rangle$ or A_E for them.

4.7.3 Effects of a Massive Tau Neutrino

The current upper limit on the τ neutrino mass is $70\,\mathrm{MeV}/c^2$ [63] so for the purposes of this experiment it was assumed that $m_{\nu_\tau} = 0$. Differential decay rates for the case of $m_{\nu_\tau} \neq 0$ have been calculated for most of the decay modes and in particular for the decay modes used in this analysis. While it is possible to calculate the energy spectrum in the laboratory frame for arbitrary neutrino mass (see appendix B), it is sufficient and much simpler to calculate the average energy in the laboratory as a function of neutrino mass. After integrating the differential decay rates over all center of mass phase space, we find the average energies in the laboratory, to lowest order in $v = m_{\nu_\tau}^2/m_\tau^2$ and $y_i = m_i^2/m_\tau^2$ $(i = e, \mu, \pi, \rho)$,

$$\begin{aligned}
\langle E\rangle(\theta)^{e,\mu} \simeq & E_{beam}\left(\frac{7-19\,v+31\,y}{20}-P(\theta)\,\frac{1-7\,v+3\,y}{20}\right),\\
\langle E\rangle(\theta)^{\pi} \simeq & E_{beam}\left(\frac{1-v+y}{2}+P(\theta)\frac{1-v-y}{6}\right), \text{ and}\\
\langle E\rangle(\theta)^{\rho} \simeq & E_{beam}\left(\frac{1-v+y}{2}+P(\theta)\frac{1-v-y}{6}\frac{1-2y}{1+2y}\right.\\
& \left.\times\frac{(1-\frac{v}{1-2y})\sqrt{1-\frac{2v(1+y)}{(1-y)^2}}}{1-\frac{v(2-y)}{(1-y)(1+2y)}}\right).
\end{aligned} \tag{4.21}$$

The narrow width approximation was made for the ρ, and β of the tau was approximated by 1. These approximations were compared with the results of calculations including neutrino mass terms of all order described briefly in appendix B and found to differ by less than 1% for neutrino masses up to several hundred MeV$/c^2$.

With these approximations it is easy to estimate the effects of a 70 MeV$/c^2$ neutrino on the average energies and demonstrate that the effects are small. The deviations from the case of zero mass are shown in Table 21. There is no reason not to assume that the tau neutrino is massless and therefore no systematic error due to the uncertainty in m_{ν_τ} was assigned.

TABLE 21. Effects of $m_{\nu_\tau} = 70$ MeV$/c^2$ on $\langle E\rangle$ and A_E. The results are given in terms of the approximate percentage deviations of the energy measurement constants a and b in equation (4.13).

Decay mode	δ_a/a (%)	δ_b/b (%)
$\tau \rightarrow \nu_\tau e\bar{\nu}_e$	−0.4	−1.1
$\tau \rightarrow \nu_\tau \mu\bar{\nu}_\mu$	−0.4	−1.1
$\tau \rightarrow \nu_\tau \pi$	−0.2	−0.3
$\tau \rightarrow \nu_\tau \rho$	−0.1	−0.4

4.7.4 Background Levels and Detection Efficiencies

Since both the average energy and the sensitivity to the tau polarization are dependent upon the decay channel, it is important to know the amount of misidentification background as well as non-tau background in each channel. Misidentification of leptons as hadrons and visa versa is especially troublesome since their polarization dependences have opposite signs. Signal to background ratios are affected by branching ratios, detection efficiency, and background rejection inefficiency. Incorrect modeling of the momentum dependence of detection efficiencies is another potential source of bias to the average energy. Systematic errors in $\langle E \rangle$ due to uncertainties in the branching ratios were calculated from the estimated background, the difference between $\langle E \rangle$ of the signal and background, and the experimental uncertainty in the branching ratio of the background. The Monte Carlo was used to estimate the average momentum of the backgrounds. The systematic errors in the polarization asymmetry due to uncertainties in the branching ratios were estimated by variation of them within their experimental limits and observation of the change in b'', the constant of proportionality between the energy asymmetry and $g_a^e\, g_v^\tau$. Systematic errors in both $\langle E \rangle$ and A_E due to uncertainties in detection efficiencies were estimated by variation of the particle identification requirements.

Table 22 summarizes the estimates for the systematic errors in b', b'', $\langle E \rangle$, and A_E due to uncertainty in the branching ratios. Note that the errors for the hadronic modes are larger than for the leptonic modes. The large contribution to $\delta\langle E \rangle_\rho$ is due to the large uncertainty in the fraction of events with two or more π°'s and the inability of the detector to resolve the multiple π°'s. Only the largest single background was included in the table since the others were found to have relatively small effects.

TABLE 22. Systematic errors for polarization measurement due to uncertainties in tau branching ratios.

	$\tau \to \nu_\tau e \bar{\nu}_e$	$\tau \to \nu_\tau \mu \bar{\nu}_\mu$	$\tau \to \nu_\tau \pi$	$\tau \to \nu_\tau \rho$
dominant background	$\tau \to \nu_\tau \rho$	$\tau \to \nu_\tau \pi$	$\tau \to \nu_\tau \rho$	$\tau \to \nu_\tau A_1$
f_{BG} (%)	10	3	10	25
$\delta(B/B_{BG})/(B/B_{BG})$ (%)	6	11	12	20
$\lvert\langle E\rangle - \langle E\rangle_{BG}\rvert$ (GeV)	0.3	1.8	2.3	0.8
$\delta\langle E\rangle/\langle E\rangle$ (%)	0.1	0.1	0.4	0.6
$\delta b'/b'$ (%)	0.8	1.0	0.5	5.0
$\delta b''/b''$ (%)	0.7	1.0	0.4	4.0

Estimates of the systematic errors in $\langle E\rangle$ and A_E due to incorrectly modeled energy dependence of the detection efficiencies or the estimation of background levels are listed in Table 23. The systematic error assigned for $\langle E\rangle_\rho$ is particularly large for several reasons. The average charged and neutral energies in the Monte Carlo and data differed by 0.3 GeV and 0.9 GeV respectively and these differences were strongly dependent on the requirements used to define a neutral shower in the SC. The problem was suspected to be due to poor modeling of overlapping charged and neutral showers. The character of the disagreement (average charged momentum was high in the data and the average neutral energy was low) indicated that perhaps there were more $\tau \to \nu_\tau \pi$ decays accompanied by false neutral showers in the data than predicted by the Monte Carlo but this conjecture was not consistent with the observation that the measurement of B_π was quite stable with respect to variation of the same neutral shower requirements (used as a veto in that case). The symptoms were also not consistent with the hypothesis that the background from $\tau \to \nu_\tau \pi \pi^\circ \pi^\circ$ was larger than indicated by the Monte Carlo since in this case one would expect the average neutral energy to be larger in the data than in the Monte Carlo.

TABLE 23. Systematic errors in $\langle E\rangle$ and A_E due to incorrect modeling of detection efficiency or background levels.

Decay mode	$\delta\langle E\rangle/\langle E\rangle$ or $\delta A_E/A_E$ (%)
$\tau \rightarrow \nu_\tau e \bar{\nu}_e$	0.5
$\tau \rightarrow \nu_\tau \mu \bar{\nu}_\mu$	0.5
$\tau \rightarrow \nu_\tau \pi$	1.2
$\tau \rightarrow \nu_\tau \rho$	8.0

For the decay mode $\tau \rightarrow \nu_\tau \rho$, which was the only channel for which a device other than the CD was used to measure $\langle E\rangle$, another source of systematic error was uncertainty in the absolute energy calibration of the SC. The agreement between $\langle E\rangle_e$ measured with the CD and SC indicates that this was a negligible effect. A realistic estimate of how well the SC could be calibrated is 1%. Sophisticated online and offline corrections to the energy response of the SC were made for events from the process $e^+e^- \rightarrow e^+e^-$ that were reliable within 1%[64] but at low momentum a significant fraction of a shower's energy could be deposited in the solenoid coil and other material before the SC, spoiling the energy calibration performed at beam energy. Therefore a conservative systematic error of 2% was assigned to the average neutral energy in $\tau \rightarrow \nu_\tau \rho$ decays and since the average neutral energy was about half of the average total energy, the systematic error assigned to $\langle E\rangle_\rho$ was 1%.

4.7.5 Effects of Energy Resolution

The momentum resolution of the CD at 2 GeV/c was about 10%. Since there are no efficiencies which vary significantly over such a small momentum range, the systematic error associated with modeling the momentum thresholds for the particle identification was assumed to be negligible.

Because the momentum resolution is Gaussian in inverse momentum rather than momentum, the momentum resolution smearing is not symmetric about the true momentum and causes a bias in $\langle p \rangle$ (which depends on the momentum spectrum and how the high momentum tail is treated). The mean momentum of an event sample with a $1 + \cos^2\theta$ angular distribution and a flat momentum distribution smeared by the resolution given in Table 7 is shown in Figure 46 as a function of the point at which the momentum spectrum is saturated. All momenta above the saturation point are assigned the momentum at the saturation point. To estimate the possible systematic bias introduced by the saturation procedure and any differences between the data and Monte Carlo the saturation point was varied by $\pm$ 5 GeV/c. Table 24 lists the systematic errors assigned to $\langle E \rangle$ and A_E due to uncertainties in the effects of the saturation procedure.

4.7.6 Detector Energy Asymmetries

There are two types of energy asymmetries possibly present in the detector. The first occurs in the case where the energy response in the $z > 0$ half of the detector is different from the response in the $z < 0$ half. This type of asymmetry was expected to have negligible effects on both the average energy and the energy asymmetry even when the charge asymmetry is large since oppositely charged particles populate the other half of the detector

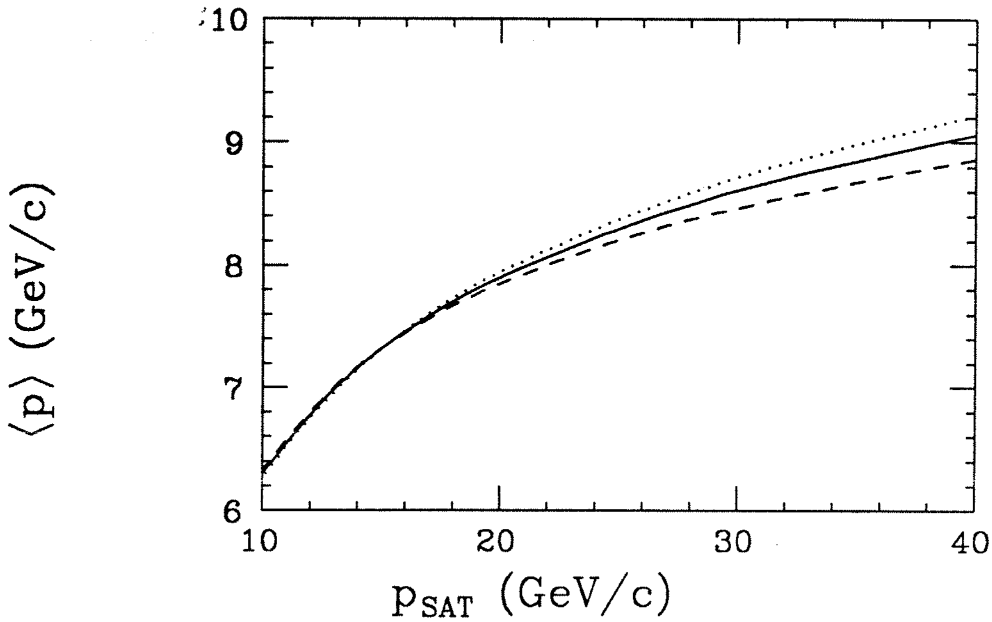

FIGURE 46. Mean momentum of a resolution smeared flat distribution (with mean momentum of 7.25 GeV/c) as a function of the momentum saturation point. The dotted (dashed) curve shows the same function for a 10% increase (decrease) of the resolution.

TABLE 24. Systematic errors assigned to $\langle E \rangle$ and A_E due to uncertainties in the momentum resolution and the momentum saturation procedure.

Decay mode	$\delta\langle E\rangle/\langle E\rangle$ or $\delta A_E/A_E$ (%)
$\tau \to \nu_\tau e \bar{\nu}_e$	1.0
$\tau \to \nu_\tau \mu \bar{\nu}_\mu$	0.6
$\tau \to \nu_\tau \pi$	0.4
$\tau \to \nu_\tau \rho$	0.4

equally to make up for any net effect incurred by the particles of one charge. The cancellation would not be complete, however, if the detection efficiency also had a $z > 0, z < 0$ asymmetry. The physical energy asymmetry is defined by $(E_f - E_b)/2$ where E_f and E_b are the average energies in the $z > 0$ and

$z < 0$ halves of the detector. For the measurement of the physical energy asymmetry, the tau decay products were assigned to the $z > 0$ or $z < 0$ hemispheres depending on which half of the detector the tau decay product was in. For the measurement of the energy asymmetry used to extract a polarization asymmetry, however, the tau decay products were assigned to the $z > 0$ or $z < 0$ hemispheres depending on the sign of the product of the charge of the tau decay product and which half of the detector the decay product was in. For example, a $tau^- \rightarrow \bar{\nu}_\tau \pi^-$ candidate in the $z > 0$ half of the detector was added to the $z > 0$ hemisphere for the physical energy asymmetry measurement and to the $z < 0$ hemisphere for the polarization asymmetry measurement. The measured physical energy asymmetries listed in Table 25 are consistent with zero and it was concluded that this type of effect was negligible.

The second type of possible energy asymmetry is unique to the central drift chamber. The CD measured the curvature, or inverse radius, of a charged track. The inverse momentum is proportional to the curvature and the sign of the curvature (defined by the direction of the cross product of the vector from the origin to the mid-point of the track and the vector from the mid-point to the center of curvature) determined the charge of the track. Therefore, the inverse momentum was assigned a sign such that $1/p = Q/|p|$, where Q was the charge. Due to causes which were not well understood, the inverse momentum spectrum was shifted such that each inverse momentum changed by $1/p \rightarrow 1/p + \Delta$. A fit to the inverse momentum spectrum of tracks from the process $e^+e^- \rightarrow \mu^+\mu^-$ (shown in figure 47) was used to determine the size of this effect; the fit to this spectrum yielded $\Delta = -0.0075 \pm 0.0011$ $(\mathrm{GeV}/c)^{-1}$. Large momentum tracks are more sensitive to such a shift (since $\delta p = p^2 \delta(1/p) = p^2\,\Delta$) so the flat pion momentum is most susceptible to this kind of effect. The effect of Δ on a flat momentum spectrum between 0 and

E is

$$\begin{aligned}\langle p\rangle &= \frac{\int \frac{p}{1+\Delta p}\,dp}{\int dp} \\ &\simeq \frac{\int p\,(1-\Delta p+\Delta^2 p^2)\,dp}{\int dp} \\ &= \frac{E}{2} - \Delta\frac{E^2}{3} + \Delta^2\frac{E^3}{4}.\end{aligned} \tag{4.22}$$

When the momentum distributions of both charges are added, the net effect on the mean momentum is

$$\langle p\rangle = \frac{E}{2} + \Delta^2\frac{E^3}{4}. \tag{4.23}$$

For $\Delta = -0.0075$ and $E = 14.5$ GeV the change in $\langle p\rangle$ is 0.043 GeV/c, not completely negligible. This effect was corrected for by the addition of 0.0075 GeV/c to the inverse momentum of each CD track in the data. A systematic error of half the size of the effect caused by introducing this correction was assigned for $\langle E\rangle$ (0.1% for e and μ, 0.3% for π, and 0.1% for ρ). Since the effect on A_E was negligible due to the fact that this effect is essentially multiplicative, no systematic error was assigned for A_E here.

TABLE 25. Physical energy asymmetries of the four decay modes.

decay mode	physical A_E (GeV)
$\tau \to \nu_\tau e \bar{\nu}_e$	-0.075 ± 0.097
$\tau \to \nu_\tau \mu \bar{\nu}_\mu$	0.001 ± 0.088
$\tau \to \nu_\tau \pi$	-0.170 ± 0.191
$\tau \to \nu_\tau \rho$	0.009 ± 0.063

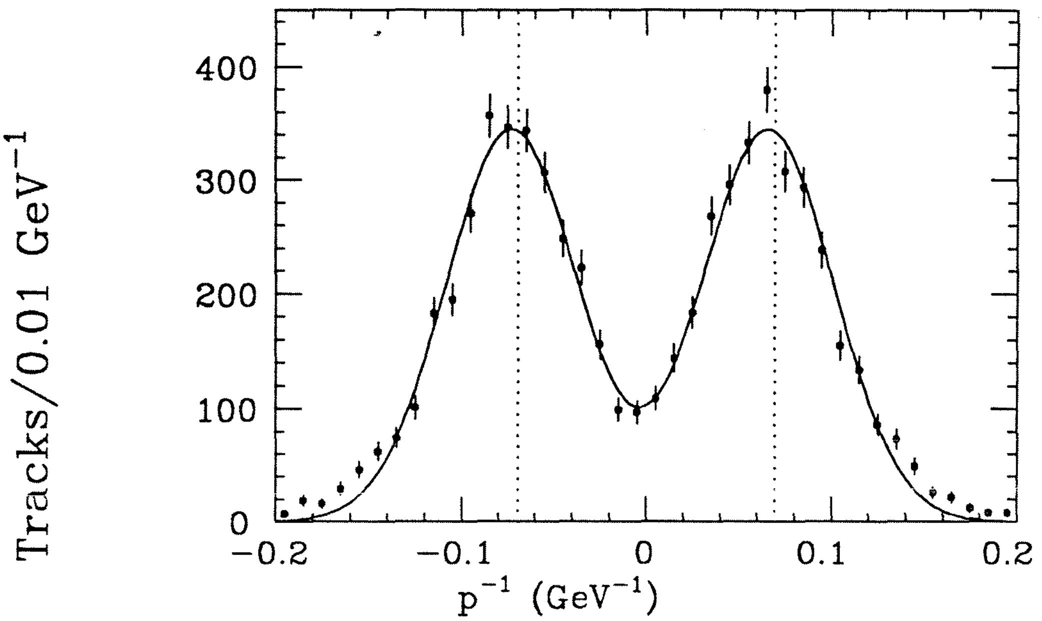

FIGURE 47. Inverse momentum spectrum of CD tracks in events from $e^+e^- \to \mu^+\mu^-$. The curve is the result of a fit of two independent Gaussians which yielded a shift of the whole spectrum of $\Delta = -0.0075 \pm 0.0011$. The vertical dotted lines indicate where the means of the two Gaussians should be.

Charge misidentification also introduces a sort of physical asymmetry which dilutes the energy asymmetry when tracks are assigned to the wrong hemisphere. If the charge misidentification were large and not modeled correctly it could introduce a bias to the data. Due to the soft momentum spectrum of tau decays, the fraction of events in the 2-prong tau data with two tracks of the same charge was about 3% and the estimated fraction of events with two charge misidentifications was about 1%. A systematic error of 1% was assigned to the energy asymmetry of all four decay modes to account for uncertainties in the charge misidentification since the Monte Carlo did not model it well.

4.7.7 Summary of Systematic Errors and Results

Table 26 is a summary of the contributions to the systematic errors in $\langle E \rangle$ and A_E. After combination of the systematic errors in quadrature, the final results are

$$g_v^e g_a^\tau(\tau \to \nu_\tau e \bar{\nu}_e) = 0.97 \pm 0.63 \pm \cancel{0.63} \quad 0.53$$

$$g_v^e g_a^\tau(\tau \to \nu_\tau \mu \bar{\nu}_\mu) = -0.53 \pm 0.50 \pm 0.35$$

$$g_v^e g_a^\tau(\tau \to \nu_\tau \pi) = -0.13 \pm 0.39 \pm 0.29$$

$$g_v^e g_a^\tau(\tau \to \nu_\tau \rho) = 3.54 \pm 0.34 \pm 3.34$$

$$g_a^e g_v^\tau(\tau \to \nu_\tau e \bar{\nu}_e) = (0.68 \pm 1.39) \times (1 \pm 0.018)$$

$$g_a^e g_v^\tau(\tau \to \nu_\tau \mu \bar{\nu}_\mu) = (0.43 \pm 0.67) \times (1 \pm 0.017)$$

$$g_a^e g_v^\tau(\tau \to \nu_\tau \pi) = (-0.20 \pm 0.54) \times (1 \pm 0.018)$$

$$g_a^e g_v^\tau(\tau \to \nu_\tau \rho) = (0.50 \pm 0.50) \times (1 \pm 0.091),$$

where the first errors are statistical and the second are systematic and the multiplicative systematic errors are indicated as product errors. The product errors on $g_a^e g_v^\tau$ are quite small and were included to draw attention to this fact and the fact that the systematic errors on $g_v^e g_a^\tau$ are not small. The pion decay mode has the smallest overall errors for both $g_v^e g_a^\tau$ and $g_a^e g_v^\tau$, despite being the smallest sample, because of its factor of about three larger sensitivity of the energy spectrum to the tau polarization, and because of the large systematic errors associated with measuring the ρ energy spectrum. The statistical errors on $g_a^e g_v^\tau$ are about 30% larger than those on $g_v^e g_a^\tau$ due to the factor of $3x^2/(3x + x^3)$, where x is the maximum detected $|\cos\theta|$, in the polarization asymmetry (see equation 1.18). The statistical error on $g_a^e g_v^\tau(\tau \to \nu_\tau e \bar{\nu}_e)$ is particularly large due to the requirement $|\cos\theta_e| < 0.75$ and the removal of events with high energy, low angle electrons from the

TABLE 26. Summary of systematic uncertainties for polarization measurement. All entries apart from those for δ_A are percentage errors. The errors quoted for δ_A are the errors in GeV.

source	quantity	$\tau \to e$	$\tau \to \mu$	$\tau \to \pi$	$\tau \to \rho$
E_{beam}	$\langle E \rangle$	0.1	0.1	0.1	0.1
Solenoid B	$\langle E \rangle$	0.4	0.4	0.4	0.2
SC calibration	$\langle E \rangle$	-	-	-	1.0
$\sigma_{1/p}$	$\langle E \rangle$	1.0	0.6	0.4	0.4
Δ shift in $1/p$	$\langle E \rangle$	< 0.1	0.1	0.3	0.1
Particle ID	$\langle E \rangle$	0.5	0.5	1.2	8.0
$\sigma_{\tau\tau}$ Rad. Corr.	$\langle E \rangle$	0.3	0.3	0.3	0.3
τ decay Rad. Cor.	$\langle E \rangle$	0.3	0.1	-	-
B.R.'s	$\langle E \rangle$	0.1	0.1	0.4	0.6
Charge Misid.	b''	1.0	1.0	1.0	1.0
τ decay Rad. Cor.	b''	0.35	< 0.1	-	-
B.R.'s	b''	0.7	1.0	0.4	4.0
B.R.'s	b'	0.8	1.0	0.5	5.0
M.C. stats.	a'	0.8	0.6	0.5	0.3
M.C. stats.	δ_A	0.047	0.035	0.077	0.031

sample as discussed in item 7 of section 3.3.

The above results were combined, allowing for effects due to the systematic errors which were common to all decay channels, to yield

$$g_v^e\, g_a^\tau = -0.05 \pm 0.21 \pm 0.34$$

$$g_a^e\, g_v^\tau = (0.26 \pm 0.31) \times (1 \pm 0.012).$$

The values of the axial-vector couplings of the electron and tau to the weak neutral current in the Standard Model are both $-1/2$. With this assumption, the coupling constant products measured in this thesis yield

$$g_v^e = 0.10 \pm 0.42 \pm 0.68$$
$$g_v^\tau = (-0.52 \pm 0.62) \times (1 \pm 0.012).$$

This result for g_v^τ is considerably more precise than the value reported by CELLO,[39] $2g_v^\tau = -0.1 \pm 2.8$, also determined with the polarization asymmetry technique. Both the present result and that reported by CELLO are consistent with the values expected in the Standard Model but the errors are too large to make any serious tests of lepton universality. It should be noted that the only other measurements of g_v^τ have been made by comparison of the total cross section for the process $e^+e^- \to \tau^+\tau^-$ with the QED cross section. This is an even more difficult experiment since the effect is proportional to $g_v^e g_v^\tau$ (see Section 1.3) and g_v^e is known to be small (-0.05 ± 0.09).[51] Typical errors for g_v^τ in these experiments are ± 2.5 or more. The present result for g_v^e is consistent with other measurements but its error is so large that it does not add significantly to the world's knowledge of g_v^e.

The above results can also be expressed in terms of the average polarization and the polarization asymmetry extrapolated to full acceptance (where the only assumption required is that the polarization must be of the form $c_1 + c_2 \times 2\cos\theta/[1+\cos^2\theta]$):

$$\langle P \rangle = -0.02 \pm 0.07 \pm 0.11$$
$$A_P = 0.06 \pm 0.08.$$

These results are consistent with the predictions of the Standard Model, $\langle P \rangle = 0.0101$ and $A_P = 0.0076$.

4.7.8 Coupling of $\tau\,\nu_\tau$ to Weak Charged Current

Since there is abundant evidence from μ decay and other weak processes that $e\,\nu_e$ and $\mu\,\nu_\mu$ have purely $V-A$ coupling to the weak charged current, the only uncertainty in the Lorentz structure of tau decay is the coupling at the $\tau\,\nu_\tau - W$ vertex. If the coupling at this vertex is written as

$$\alpha\,(V-A)+\beta\,(V+A) \tag{4.24}$$

the well known Michel parameter can be written as[65]

$$\rho=\frac{3}{4}(1-\frac{\beta^2}{\alpha^2+\beta^2}). \tag{4.25}$$

Interactions which are pure $V-A$, V or A, $V+A$ give $\rho=\frac{3}{4},\frac{3}{8}$, and 0 respectively.

In terms of the Michel parameter, the differential decay rates for the four decay modes considered here, neglecting all masses apart from the ρ mass (where the narrow width approximation has been made) are

$$\begin{aligned}
\frac{d\Gamma_{e,\mu}}{dx\,d\cos\theta} &= \frac{G_F^2 m_\tau^5}{192\pi^3}\frac{2}{3}\Big\{9\,x^2\,(1-x)+2\,\rho\,x\,(4\,x^2-3\,x)\\
&\quad +P\,\cos\theta\,(3-\frac{8}{3}\rho)\,x\\
&\quad \times\,\Big[3\,x\,(1-x)+\frac{3}{2}(1-\frac{3-4\,\rho}{3-\frac{8}{3}\rho})\,x\,(4\,x-3)\Big]\Big\},\\
\frac{d\Gamma_\pi}{d\cos\theta} &= \frac{G_F^2\,f_\pi^2\,\cos^2\theta_c}{32\,\pi}m_\tau^3\,(1-\frac{m_\pi^2}{m_\tau^2})^2\\
&\quad \times\,[1+P\,\cos\theta\,(\frac{8}{3}\rho-1)],\ \text{and}\\
\frac{d\Gamma_\rho}{d\cos\theta} &= \frac{G_F^2\,f_\rho^2\,\cos^2\theta_c}{32\,\pi}\frac{m_\tau^3}{m_\rho^2}(1-y)^2(1+2\,y)\\
&\quad \times\,\Big[1+P\,\cos\theta\,\frac{1-2\,y}{1+2\,y}(\frac{8}{3}\rho-1)\Big]
\end{aligned} \tag{4.26}$$

where $y=m_\rho^2/m_\tau^2$. It is then a simple matter to show that the average energies in the laboratory are

$$
\begin{aligned}
\langle E \rangle_{e,\mu} &\simeq E_{beam} \left(\frac{2\rho + 9}{30} + P\, \frac{1 - \frac{2}{3}\rho}{10} \right), \\
\langle E \rangle_{\pi} &\simeq E_{beam} \left(\frac{1}{2} + P\, \frac{\frac{8}{3}\rho - 1}{6} \right), \text{ and} \\
\langle E \rangle_{\rho} &\simeq E_{beam}\, (1 + y) \left(\frac{1}{2} + \frac{P\,(\frac{8}{3}\rho - 1)}{6} \frac{1 - 2y}{1 + 2y} \right).
\end{aligned}
\tag{4.27}
$$

Note that for hadronic τ decays only the polarization dependent terms of $\langle E \rangle$ depend on ρ. This is in contrast to the leptonic decays for which there is ρ dependence in both the constant and polarization dependent terms of $\langle E \rangle$.

Table 27 shows the deviations $\langle E \rangle$ and A_E for the current world average measured value of ρ (0.71 ± 0.08)[6,66] and for a one standard deviation downward fluctuation of ρ from the measured value. It is clear that large effects on the measured values of $\langle E \rangle$ and A_E due to $\rho \neq \frac{3}{4}$ cannot be ruled out at the present time but since the polarization experiment is actually a measurement of the tau couplings to the Z^0 and not the W, it was assumed that $\rho = \frac{3}{4}$.

The polarization experiment consisted in part of measuring the average laboratory energy. Since the average laboratory energy depends on ρ, it can be used to measure ρ also. For this measurement it was assumed that the the tau polarization is small (as expected in the GWS model). It has already been noted that the average energy in hadronic tau decays is not sensitive to ρ. Therefore the only ways to measure ρ for these modes are to measure precisely the average polarization or to measure momentum or angle correlations in events with identified hadronic tau decays.[67] The Monte Carlo was used to calculate the ρ dependence of the average laboratory

TABLE 27. Effects of a non-standard Michel parameter on the energy spectra. Deviations of the average energy and energy asymmetry due to uncertainty in the amount of $V + A$ present in the $\tau\nu_\tau$ current are shown as percentage changes. The two columns at the left are for the current world average of the Michel parameter ρ and the two at the right are for a one standard deviation downward fluctuation of ρ.

	ρ=0.71		ρ=0.63	
Decay mode	$\delta\langle E\rangle/\langle E\rangle$ (%)	$\delta A_E/A_E$ (%)	$\delta\langle E\rangle/\langle E\rangle$ (%)	$\delta A_E/A_E$ (%)
$\tau \to \nu_\tau e \bar{\nu}_e$	−0.8	+5.1	−2.5	+14.8
$\tau \to \nu_\tau \mu \bar{\nu}_\mu$	−0.8	+5.1	−2.5	+14.8
$\tau \to \nu_\tau \pi$	0.0	−10.7	0.0	−34.7
$\tau \to \nu_\tau \rho$	0.0	−10.7	0.0	−34.7

energy for the leptonic decay modes:

$$\langle E\rangle_{e,\mu} = a_{e,\mu} + b_{e,\mu}\,(\rho - \frac{3}{4}). \tag{4.28}$$

Table 28 lists the calculated values of $a_{e,\mu}$ and $b_{e,\mu}$ and the measured values of $\langle E\rangle_{e,\mu}$. The effects of particle misidentification on $a_{e,\mu}$ (a bias) and $b_{e,\mu}$ (decreased sensitivity) have been included. Figures 48 and 49 show the momentum spectra compared with the Monte Carlo for extreme values of ρ. The description of the contributions to the systematic errors in $\langle F\rangle$ were described in the previous sections and can be applied directly here. The final results are

0.165 ± 0.139

$$\rho_e = 0.623 \pm 0.\cancel{182 \pm 0.115}$$

$$\rho_\mu = 0.892 \pm \cancel{0.144 \pm 0.0}81,$$

0.135 ± 0.095

where the first errors are statistical and the second are systematic. These results can be combined (since the couplings of $e\,\nu_e$ and $\mu\,\nu_\mu$ to the W have been shown to be the same) to yield

$$\rho = 0.792 \pm 0.113 \pm 0.092.$$

$0.791 \pm 0.104 \pm 0.123$

TABLE 28. Results of ρ parameter measurement. The constants a_l and b_l (equation (4.28)) were calculated with the Monte Carlo and include the effects of background.

	electron	muon
a_l (GeV)	5.656 ± 0.047	6.650 ± 0.039
b_l (GeV)	0.613	0.779
$\langle E \rangle_l$ (GeV)	5.578 ± 0.101	6.761 ± 0.105

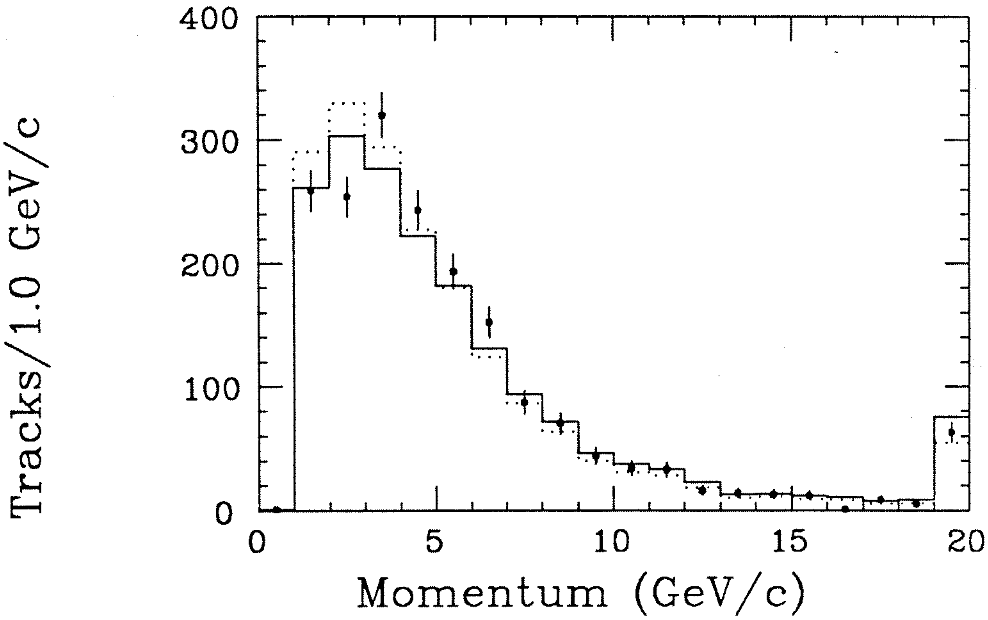

FIGURE 48. Momentum spectrum for $\tau \to \nu_\tau e \bar{\nu}_e$ with $\rho = 3/4, 0$. The solid (dotted) curve is the Monte Carlo prediction for the momentum spectrum when $\rho = 3/4(0)$.

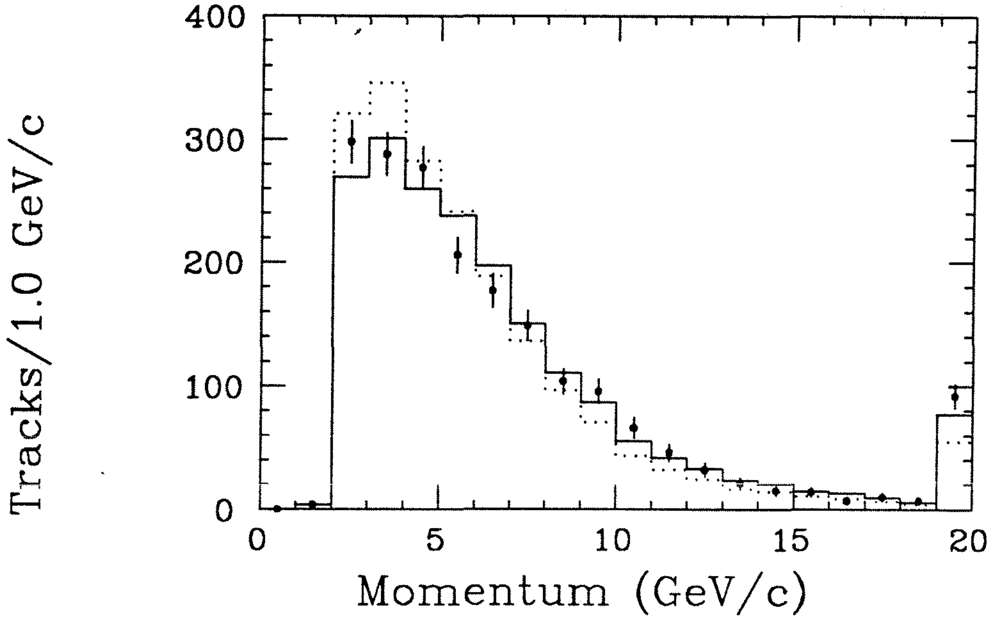

FIGURE 49. Momentum spectrum for $\tau \to \nu_\tau \mu \bar{\nu}_\mu$ with $\rho = 3/4, 0$. The solid (dotted) curve is the Monte Carlo prediction for the momentum spectrum when $\rho = 3/4(0)$.

The results presented here and previous measurements of the Michel ρ parameter are listed in Table 29. The final result is in agreement with the previous world average. When combined with previous results, the new world average becomes $\rho = 0.73 \pm 0.07$. A $V+A$, V, or A interaction at the $\tau\nu_\tau - W$ vertex is ruled out by this result but an admixture of about 27% $V+A$ with the expected $V-A$ interaction is not excluded.

TABLE 29. Measured values of the ρ parameter.

Experiment	ρ_e	ρ_μ	Average
DELCO [6]	0.72 ± 0.15	-	0.72 ± 0.15
CLEO [66]	0.59 ± 0.14	0.81 ± 0.14	$0.70 \pm 0.10 \pm 0.03$
This experiment	$0.62 \pm 0.18 \pm 0.12$	$0.89 \pm 0.14 \pm 0.08$	$0.79 \pm 0.11 \pm 0.09$
Average	0.65 ± 0.09	0.84 ± 0.11	0.73 ± 0.07

CHAPTER 5

SUMMARY AND CONCLUSION

5.1 Leptonic Branching Ratios

The three leptonic branching ratio results were

$$B_e B_\mu = 0.0288 \pm 0.0017 \pm 0.0019$$

$$B_e = 0.180 \pm 0.009 \pm 0.006$$

$$B_\mu = 0.183 \pm 0.009 \pm 0.005.$$

The result $B_\mu/B_e = 1.02 \pm 0.07 \pm 0.04$ from the $e-3$ and $\mu-3$ results is consistent with 0.973, the value expected from $e-\mu$ universality, the previous world average of 0.94 ± 0.05, and previous universality tests.[68] The result for $B_e B_\mu$ can be used as a constraint to reduce the errors for B_e and B_μ. This combined fit yields

$$B_e = 0.174 \pm 0.008 \pm 0.005$$

$$B_\mu = 0.177 \pm 0.008 \pm 0.005.$$

These results are consistent with the previous world averages of $B_e = 0.179 \pm 0.006$ and $B_\mu = 0.169 \pm 0.007$. The three results can also be combined with the assumption of $e-\mu$ universality ($B_\mu = 0.973\, B_e$) to yield

$$B_e = 0.178 \pm 0.005.$$

The systematic errors common to the three results were accounted for in the combined results.

The combination of this result with the previous world average yields $B_e = 0.179 \pm 0.004$, which implies a tau lifetime of $(2.86 \pm 0.06) \times 10^{-13}$ sec, consistent with the world average tau lifetime of $(2.84 \pm 0.19) \times 10^{-13}$ sec. In section 1.6.3 it was shown that it was not possible to account for the observed 1-prong branching ratio with the sum of the exclusive branching ratios that contribute to B_1 (about 6% of B_1 is not accounted for). One suggestion which solves this problem assumes that the measurements of the leptonic branching ratios have been incorrect and that the true value of B_e is $\sim$ 19.3%. This suggestion implies that the measured electron branching ratio is about 3.5 standard deviations low. Thus other solutions to this problem appear to be necessary.

5.2 Pion Branching Ratio

The final pion branching ratio result,

$$B_\pi = 0.106 \pm 0.004 \pm 0.008,$$

is in agreement with the previous world average of 0.105 ± 0.011. It is also consistent with the value predicted by the measured values of the pion and tau lifetimes of 0.109 ± 0.007. The ratio of the pion branching ratio measured here to the world average value of the electron branching ratio (the result in section 4.4.2 was combined with the value of B_e listed in Table 5),

$$B_\pi / B_e = 0.60 \pm 0.05,$$

is consistent with the theoretical prediction of 0.607.

5.3 Five Charged Prong Branching Ratio

Two experiments at PEP observed about a dozen 5-prong tau decays with little background after a previous version of this analysis was published[26] . The average of their measurements[31,32] is $B_5 = 0.0014 \pm 0.0004$ (systematic and statistical error were combined in quadrature). The successful observation of this rare topology with essentially no background by these other experiments was made possible by the large size and fine granularity of their central drift chambers and the small amount of material in front of them. The present result for the branching ratio for tau to five charged hadrons, $B_5 < 0.0027$ at the 95% confidence level, is consistent with all previous limits (see Table 3) and the measurements quoted above.

5.4 Tau Polarization

The value of the axial-vector coupling of the electron to the weak neutral current in the Standard Model is $-1/2$. With this assumption, the coupling constant product measured in this thesis of

$$g_a^e\, g_v^\tau = (0.26 \pm 0.31) \times (1 \pm 0.012)$$

yields

$$g_v^\tau = (-0.52 \pm 0.62) \times (1 \pm 0.012).$$

This result is considerably more precise than the value reported by CELLO[39] ($2\, g_v^\tau \;=\; -0.1 \pm 2.8$), also determined with the polarization asymmetry technique. Both of these results are consistent with the values expected in the Standard Model but the errors are too large to make any serious tests of lepton universality.

5.5 $V + A$ Limits

The value of the Michel ρ parameter measured in this experiment,

$$\rho = 0.79 \pm 0.113 \pm 0.092,$$

is consistent with the previous world average of 0.71 ± 0.08 and with the expected value of $3/4$ ($\rho = 3/4$ for a pure $V - A$ interaction). When the result of this experiment is combined with the previous results, the new world average becomes $\rho = 0.73 \pm 0.07$. A $V + A$, V, or A interaction at the $\tau\nu_\tau - W$ vertex is ruled out by this value of ρ but an admixture of about 27% $V + A$ with the expected $V - A$ interaction is not excluded.

5.6 Conclusions

No inconsistencies with the standard picture of the tau (a lepton with weak couplings identical to those of e and μ) were found. The measured branching ratios support previous measurements and add weight to the assertion that about 6% of tau decays cannot be accounted for by known decay modes.

REFERENCES

1. (SLAC-LBL Collaboration) M. L. Perl *et al.*, Phys. Rev. Lett. **35**, 1489 (1975).

2. (DASP Collaboration) R. Brandelik *et al.*, Phys. Lett. **73B**, 109 (1978).

3. (DELCO Collaboration) W. Bacino *et al.*, Phys. Rev. Lett. **41**, 13 (1978).

4. (DESY-HEIDELBERG Collaboration) W. Bartel *et al.*, Phys. Lett. **77B**, 331 (1978).

5. (PLUTO Collaboration) J. Burmester *et al.*, Phys. Lett. **68B**, 297 (1977); (SLAC-LBL Collaboration) M. L. Perl *et al.*, Phys. Lett. **70B**, 487 (1977).

6. (DELCO Collaboration) W. Bacino *et al.*, Phys. Rev. Lett. **42**, 749 (1979).

7. (SLAC-LBL Collaboration) J. A. Jaros *et al.*, Phys. Rev. Lett **40**, 1120 (1978).

8. (SLAC-LBL Collaboration) G. S. Abrams *et al.*, Phys. Rev. Lett **43**, 1555 (1979).

9. (SLAC-LBL Collaboration) C. A. Blocker *et al.*, **109B**, 119 (1982).

10. (DELCO Collaboration) W. Ruckstuhl *et al.*, Phys. Rev. Lett. **56**, 2132 (1986).

11. (Mark II Collaboration) G. J. Feldman *et al.*, Phys. Rev. Lett. **48**, 66 (1982); W. T. Ford *et al.*, Phys. Rev. Lett. **49**, 106 (1982).

12. S. Weinberg, Phys. Rev. Lett. **19**, 1264 (1967); A. Salam, *Elementary Particle Theory*, edited by N. Svartholm (Almquist and Forlag, Stockholm, 1968), p. 367; G. t'Hooft, Nucl. Phys. B **35**, 167 (1971); B. W. Lee, Phys. Rev. D **5**, 823 (1972); S. Weinberg, Phys. Rev. Lett. **27**, 1688 (1971).

13. H. D. Dahmen, L. Schülke, and G. Zech, Z. Physik C **5**, 71 (1980).

14. (Particle Data Group) M. Aguilar-Benitz *et al.*, Phys. Lett. **170B** (1986).

15. (UA-1 Collaboration) G. Arnison *et al.*, Phys. Lett. **122B**, 103 (1983); (UA-2 Collaboration) M. Banner *et al.*, Phys. Lett. **122B**, 476 (1983).

16. (MAC Collaboration) E. Fernandez *et al.*, Phys. Rev. Lett. **54**, 1620 (1985).

17. (Mark II Collaboration) M. E. Levt *et al.*, Phys. Rev. Lett. **51**, 1941 (1983).

18. (JADE Collaboration) W. Bartel *et al.*, Phys. Lett. B **161**, 188 (1985).

19. (HRS Collaboration) K. K. Gan *et al.*, Phys. Lett. B **153**, 116 (1985).

20. (PLUTO Collaboration) Ch. Berger *et al.*, Z. Physik C **28**, 1 (1985).

21. (TASSO Collaboration) M. Althoff *et al.*, Z. Physik C **26**, 521 (1985).

22. P. Limon, M. L. Stevenson, W. A. Wenzel, in *Proceedings of the 1974 PEP Summer Study*, Berkeley, pp. 349-355 (1975).

23. Y. S. Tsai, Phys. Rev. D **4**, 2821 (1971).

24. F. J. Gilman and S. H. Rhie, Phys. Rev. D **31**, 1066 (1985).

25. (HRS Collaboration) M. Derrick *et al.*, Phys. Rev. Lett. **55**, 570 (1985).

26. (MAC Collaboration) E. Fernandez *et al.*, Phys. Rev. Lett. **54**, 1624 (1985).

27. (Mark II Collaboration) C. A. Blocker *et al.*, Phys. Rev. Lett. **49**, 1369 (1982).

28. (TPC Collaboration) H. Aihara *et al.*, Phys. Rev. D **30**, 2436 (1984).

29. (TASSO Collaboration) R. Brandelik *et al.*, Phys. Lett. **92B**, 199 (1980).

30. (CELLO Collaboration) H. J. Behrend *et al.*, Phys. Lett. **114B**, 282 (19822).

31. (HRS Collaboration) M. Derrick *et al.*, Phys. Rev. Lett. **55**, 1775 (1985).

32. (Mark II Collaboration) P. R. Burchat *et al.*, **54**, 2489 (1985).

33. (CELLO Collaboration) H. J. Behrend *et al.*, Z. Physik C **23**, 103 (1984).

34. (Mark II Collaboration) J. Jaros, SLAC-PUB-3569, *Proceedings of the 12th SLAC Summer Institute on Particle Physics*, ed. by P. McDonough, p. 427 (1984).

35. (MAC Collaboration) in *Proceedings of the 1985 International Symposium on Lepton and Photon Interactions at High Energies*, Kyoto, Japan (1985).

36. (HRS Collaboration) in *Proceedings of the International Symposium on Lepton and Photon Interactions at High Energies*, Kyoto, Japan (1985).

37. (TASSO Collaboration) M. Althof *et al.*, Phys. Lett. B **141**, 264 (1984).

38. P. R. Burchat, Stanford University Ph.D. Thesis, SLAC-Report-292 (1986).

39. (CELLO Collaboration) H. J. Behrend *et al.*, Phys. Lett. **127B**, 270 (1983).

40. (Mark II Collaboration) J. M. Yelton *et al.*, Phys. Rev. Lett. **56**, 812 (1986).

41. (MAC Collaboration) W. W. Ash *et al.*, Phys. Rev. Lett. **55**, 2118 (1985).

42. (MAC Collaboration) E. Fernandez *et al.*, Phys. Rev. D **31**, 1537 (1985), and references therein.

43. G. E. Fisher, SLAC technical note PEP-PTM-210, 1979 (unpublished); R. H. Helm, P. B. Wilson, and H. Wiedemann, SLAC technical note PEP-PTM-103-R1, 1975 (unpublished); J. Martin, Private communication.

44. R.Weinstein, MAC Note 230 (unpublished).

45. F. A. Berends, R. Kleiss, and S. Jadach, Nucl. Phys. B **202**, 63 (182).

46. R. L. Ford and W. R. Nelson, SLAC Report No. SLAC-PUB-210, unpublished (1978).

47. T. W. Armstrong, in *Computer Techniques in Radiation Transport and Dosimetry*, edited by W. R. Nelson and T. M. Jenkins (Plenum, New York, 1980).

48. T. Sjöstrand, Comput. Phys. Commun. **27**, 243 (1983).

49. R. Bhattacharya, J. Smith, and G. Grammer, Jr., Phys. Rev. D **15**, 3267 (1977); J. Smith, J. A. M. Vermaseren, and G. Grammer, Phys. Rev. D **15**, 3280 (1977).

50. (MAC Collaboration) E. Fernandez *et al.*, SLAC-PUB-4004, submitted to Phys. Rev. D (1986).

51. (MAC Collaboration) E. Fernandez *et al.*, SLAC-PUB-4005, submitted to Phys. Rev. D (1986).

52. D. A. Bryman *et al.*, Phys. Rev. Lett. **50**, 7 (1983).

53. (Mark III Collaboration) R. M. Baltrusaitis *et al.*, Phys. Rev. Lett. **55**, 1842 (1985).

54. (DELCO Collaboration) W. Bacino *et al.*, Phys. Rev. lett. **42**, 6 (1979).

55. F. Reines, H. S. Gurr, and H. W. Sobel, Phys. Rev. Lett. **37**, 315 (1976); F. T. Avignone *et al.*, Phys. Rev. D **16**, 2383 (1977); W. Krenz, Physikalisches Institut, Technische Hochschule Aachen, Germany preprint PITHA 82/26 (1982, unpublished).

56. *Quarks and Leptons: An Introductory Course in Modern Particle Physics* by F. Halzen and A. D. Martin, pp. 126-127, N.Y., Wiley, (1984).

57. M. Böhm and W. Hollik, Nucl. Phys. B **204**, 45 (1982); W. Hollik, University of Würzburg Print-83-0312 (unpublished).

58. F. A. Berends, R. Kleiss, and S. Jadach, Nucl. Phys. B **202**, 63 (182).

59. (MAC Collaboration) E. Fernandez *et al.*, Phys. Rev. Lett. **50**, 1238 (1983).

60. (MAC Collaboration) W. T. Ford *et al.*, Phys. Rev.Lett. **51**, 257 (1983).

61. T. Kinoshita and A. Sirlin, Phys. Rev. **113**, 1652 (1958); F. Scheck, Phys. Reports **44**, 187 (1978); A. Ali and Z. Z. Aydin, Nuovo Cim. **43A**, 270 (1978).

62. J. H. Kim and L. Resnick, Phys. Rev. D **21**, 1330 (1980); A. Garcia and J. M. Rivera Rebolledo, Nucl. Phys. B **189**, 500 (1981).

63. (ARGUS Collaboration) H. Albrecht *et al.*, Phys. Lett. **163B**, 404 (1985); (HRS Collaboration) S. Abachi *et al.*, Phys. Rev. Lett. **56**, 1039 (1986).

64. M. C. Delfino, Univ. of Wisconsin-Madison Ph.D. Thesis, Report WISC-EX-85/263.

65. K. Mursula and F. Scheck, Nucl. Phys. B **253**, 189 (1985).

66. (CLEO Collaboration) S. Behrends *et al.*, Phys. Rev. D **32**, 2468 (1985).

67. J. Babson and E. Ma, Phys. Rev. D **26**, 2497 (1982); J. Babson and E. Ma, Z. Physik C **20**, 5 (1983).

68. D. A. Bryman *et al.*, Phys. Rev. Lett. **50**, 7 (1983).

69. For example, *Data Analysis for Scientists and Engineers*, Stuart L. Meyer, N.Y., Wiley, 1975.

70. REDUCE 3.2, The Rand Corporation, Santa Monica, California.

APPENDIX A

MUON MISIDENTIFICATION MEASUREMENT

The distinguishing characteristic of a muon in the MAC detector was a track in the outer drift chambers which, when extrapolated back through the detector to the origin, agreed in momentum and polar angle with a track in the central drift chamber. Possible causes of misidentification of tracks as muons include false OD tracks due to noise hits, cosmic rays in accidental coincidence with an annihilation event, pion and kaon decays in flight, and hadronic showers which completely penetrate the hadron calorimeter.

The noise and cosmic ray backgrounds were largely eliminated by the CD-OD matching criteria discussed in section 2.5 and were determined to be negligible by measurement of the fraction of tracks with a CD-OD match in events from the process $e^+e^- \rightarrow e^+e^-$ which were selected without regard to activity in the OD. In a sample of 17546 tracks there were 6 CD-OD matches and therefore the muon misidentification from cosmic ray and noise backgrounds was less than 0.04% per track.

The detector simulation modeled hadron decay and shower penetration ("punchthrough") processes but the latter is a complicated process which is difficult to model accurately. A comparison of muon misidentification in the detector simulation with that in the data was made with the rather clean source of pions available in the tau data sample. Charged tracks in 3-charged prong tau decays are known to be mostly hadrons: The 1.4% background was composed of electrons from photon conversion pairs or π^0 Dalitz decay pairs. The prompt muon contamination from tau-pair events was negligible. Backgrounds (estimated with Monte Carlo calculations) from the processes $e^+e^- \rightarrow e^+e^-\tau^+\tau^-$ and $e^+e^- \rightarrow q\bar{q}$ amounting to 4.5% of the input tracks and 5.5% of the misidentified muon tracks were subtracted. All other backgrounds were negligible.

The muon misidentification probability was calculated by dividing the number of tracks with a CD-OD match by the total number of tracks. The misidentification probability for the data and Monte Carlo is shown in Figure 50. When integrated over polar angles, the average misidentification probability is 0.0192±0.0008 (20% π/K decays, 80% punchthrough) for the Monte Carlo and 0.0189±0.0018 for the data. The average momentum of the tracks in the input sample of hadrons was 3.3 GeV/c for both the data and Monte Carlo and the standard deviations of the momentum spectra were both 2.6 GeV/c. Since the Monte Carlo was able to reproduce the data quite well, it was not necessary to correct the amount of background in studies of muonic tau decays.

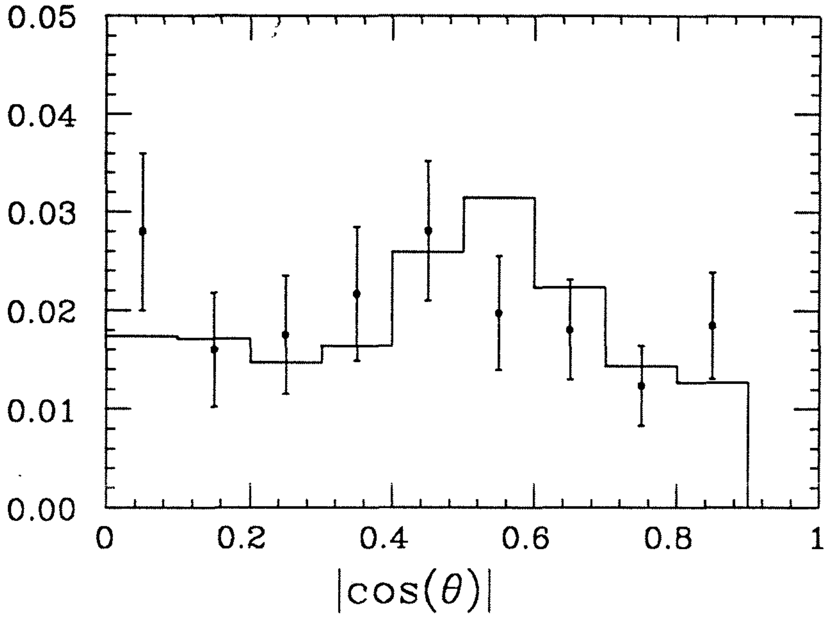

FIGURE 50. Muon misidentification probability per hadron measured with hadrons in 3-prong tau decays. The solid line is for the Monte Carlo. The average momentum of the hadrons was 3.3 GeV/c and the standard deviation of the momentum spectrum was 2.6 GeV/c.

APPENDIX B

LABORATORY ENERGY SPECTRA

Since the differential decay rates of the tau have been calculated in the tau center of mass, in order to calculate a laboratory momentum spectrum it is necessary to do a Monte Carlo calculation or transform the spectrum to the laboratory frame. In some instances it is convenient to have an analytic form of the laboratory momentum spectrum at hand.

The procedure for transforming a probability distribution which is a function of several variables to one which is a function of one variable, that variable being a function of the original variables, can be found in standard textbooks on statistical analysis.[69] The transformation of a differential decay rate which depends on x, the energy of the tau decay product divided by $m_\tau/2$, and $\cos\theta$, the polar angle between the decay product and the polarization axis, to the differential decay rate which is a function of x', the laboratory energy divided by the maximum possible laboratory energy, is outlined here. The problem is simplified greatly when the decay product is massless and β of the tau is $\sim$ 1 so that the Lorentz boost becomes $x' = \frac{x}{2}(1+\cos\theta)$. Let the differential decay rate be of the form

$$\frac{dN}{dx\,d\cos\theta} = ax^n + bx^m \cos\theta. \tag{B.1}$$

The differential decay rate in the laboratory is given by

$$\frac{dN}{dx'} = \frac{d}{dx'} N(x_{lab} < x') \tag{B.2}$$

where $N(x_{lab} < x')$ is the total number of events with a laboratory energy less than x' and is simply the integral of the center of mass differential decay rate over the area A in the $x, \cos\theta$ plane for which $x_{lab} < x'$ (see Figure 51):

$$N(x < x') = \iint\limits_A \frac{dN}{dx\, d\cos\theta} dx\, d\cos\theta. \tag{B.3}$$

The area of integration consists of two pieces. The first is a rectangle which covers the region $-1 < \cos\theta < 1$ and $0 < x < x'$, x' being the value of x in the center of mass for which $\cos\theta = 1$ and $x_{lab} = x'$. The second piece of the area of integration is given by $x' < x < 1$ and $-1 < \cos\theta < \frac{2x'}{x} - 1$. With the help of the identity $\frac{d}{dx}\int_a^x f(u)\, du = f(x)$ it is straightforward to show that

$$\frac{dN}{dx'} = \alpha + \beta \tag{B.4}$$

where

$$\alpha = \begin{cases} 2a\frac{1-(x')^n}{n} & (n \neq 0) \\ -2a \ln x' & (n = 0) \end{cases} \tag{B.5}$$

$$\beta = \begin{cases} 2b\left[\frac{2x'}{m-1} - \frac{1}{m} + (x')^m (m+1)\left(\frac{1}{m} - \frac{1}{m-1}\right)\right] & (m > 1, m < 0) \\ 2b\,(x' - 1 - 2x' \ln x') & (m = 1) \\ 2b\,(2 + \ln x' - 2x') & (m = 0). \end{cases} \tag{B.6}$$

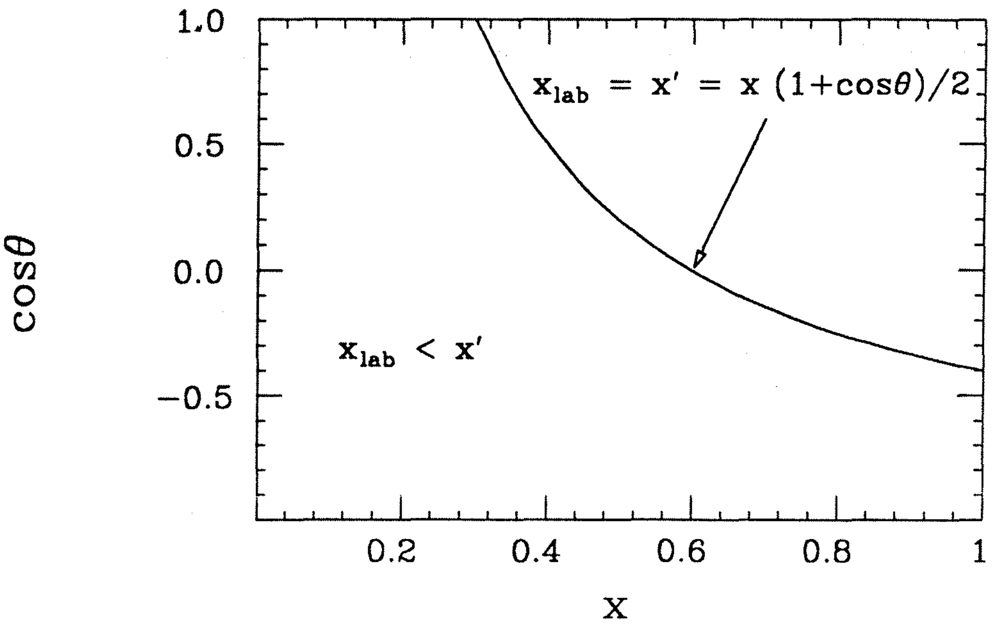

FIGURE 51. Area of integration for transformation of a center of mass differential decay rate to the laboratory. The curve represents a constant laboratory energy fraction x'. The area underneath and to the left of the curve is the area of integration A in equation (B.3).

With these results it is straightforward to show, for instance, that the center of mass differential decay rate for the decay $\tau \rightarrow \nu_\tau e \bar{\nu}_e$

$$\frac{dN}{dx\,d\cos\theta} = 3\,x^2 - 2\,x^3 - P\,\cos\theta\,x^2\,(2\,x - 1), \tag{B.7}$$

where P is the polarization, yields a laboratory energy spectrum of

$$\frac{dN}{dx'} = \frac{5 - 9\,(x')^2 + 4\,(x')^3}{3} + P\,\frac{1 - 9\,(x')^2 + 8\,(x')^3}{3}. \tag{B.8}$$

This procedure is even simpler when the differential decay rate has a delta function in energy such as for the decay $\tau \rightarrow \nu_\tau \pi$. If the decay rate is written in the form

$$\frac{dN}{dx\,d\cos\theta} = (a + b\cos\theta)\,\delta(x - x_0) \tag{B.9}$$

where x_0 is the energy fraction of the decay product then it is straightforward to show that the energy spectrum in the laboratory is given by

$$\frac{dN}{dx'} = \frac{2}{x_0}[a + b(1 - 2x')]. \tag{B.10}$$

Inclusion of effects such as a massive tau neutrino and the mass of the decay product greatly complicates the calculation of the laboratory energy spectrum. In addition to the increased complexity and number of integrals to perform, the area of integration A must be carefully calculated as it loses its simple shape. The laboratory energy spectrum for the decay $\tau \to \nu_\tau \mu \bar{\nu}_\mu$ was calculated using the algebraic programming package REDUCE[70] and used to check the validity of the approximations of the mean laboratory energies as functions of the decay product mass and the tau neutrino mass found in Section 4.7.3.